Università di Pisa

Facoltà di Scienze Matematiche, Fisiche e Naturali

School of Graduate Studies "Galileo Galilei"

Applied Physics

Ph.D. Thesis

Numerical Studies of the Structure and Dynamics of Polymers

Candidate:

Luca Larini

Tutor:

Prof. Dino Leporini

Director of the School:

Prof. Francesco Pegoraro

2007

This work is a more extensive exposition of the following papers appeared (or which are to appear):

1. P.A. Rolla, D. Prevosto, M. Lucchesi, S. Capaccioli, L. Larini; "Structural dynamics in polymers interpreted in terms of the Adam-Gibbs theory." *Current Trends in Polymer Science* **9**, 69 (2004).

2. L. Larini, A. Barbieri, D. Prevosto, P.A. Rolla, D. Leporini; "Transient and equilibrated single-molecule crystals of polyethylene: Molecular dynamics studies of the lamellar fold length." *Journal of Physics: Condensed Matter* **17**, L199 (2005).

3. L. Larini, D. Leporini; "A manifestation of the Ostwald step rule: Molecular-dynamics simulations and free-energy landscape of the primary nucleation and melting of single-molecule polyethylene in dilute solution." *Journal of Chemical Physics* **123**, 144907 (2005).

4. L. Larini, A. Barbieri, D. Leporini; "Equilibrated polyethylene single molecule crystals: molecular-dynamics simulations and analytic model of the global minimum of the free-energy landscape." *Physica A: Statistical Mechanics and its Applications* **364**, 183 (2006).

5. L. Larini, D. Leporini; "Free-energy effects in single-molecule polymer crystals." *Journal of Non-Crystalline Solids* **352**, 5021 (2006).

6. L. Larini, D. Leporini; "The free-energy landscape of single-molecule polymer crystals." *Philosophical Magazine* **87**, 411 (2007).

7. L. Larini, R. Mannella, D. Leporini; "Langevin stabilization of molecular-dynamics simulations of polymers by means of quasisymplectic algorithms." *Journal of Chemical Physics* **126**, 104101 (2007).
   Also selected for pubblication on the Virtual journal of Biological Physics Research, 15 March 2007 issue (http://www.vjbio.org)

Preface

Polymers respresent one of the most wonderful and fascinating class of materials: they are the constituent of the biological matter, and the basis of the modern technologies. They are ubiquitous: clothes(for example: nylon,wool), lubrificant, food, proteins, ...

Since the very beginning of polymer history, with the formulation of theory of chain molecules due to Staudinger in 1920s, the knowledge of this type of matter has been growing faster and faster, both from the chemical and from the physical point of view. These results make polymers an increasingly attractive topic for investigation.

Nevertheless, several open issues in polymer physics remain. In this thesis, we consider three of them: the problem of polymer crystallization, the questions arising from the glass transition and the improvement of the actual models for simulating polymers. To each of these themes is devoted one of the three sections of this thesis.

In part I we tackle the process of polymer crystallization. It is curious to observe that one of the arguments presented against the ideas of Staudinger came from the field of polymer crystallization: how can a gigantic molecule fit into a minuscule crystal unit cell? In fact, this is not possible. The answer is that the single molecule itself is part of different unit cells, and the repeting unit is not a molecules or a collection of molecules, but a section, a very tiny section, of the whole molecule. In principle, just one, extremely long, molecule is sufficient to build up a crystal. This fascinating perspective was so attractive

that we simulated one single molecule of polyethylene in order to produce a (very) small crystal; this tiny structure demonstrated to possess enough details to be valuable of several studies: after a general introduction of the polymer crystalization (chapter 1) and an explanation of the model employed (chapter 2), will be presented the original results (chapter 3), with a particular focus on the free energy landscape features(chapters 4 and 5).

Simulating materials which are so complex, and whose properties are the result of effects which work on several time and length scales is very challenging. To this aspect of the problem is devoted the Part II. There, is proposed a series of new algorithms, in the framework of symplectic integration schemes, which have been put forward in order to reach longer time steps; in this way is possible to span a wider dynamic of the system, and, so, more ample spectra of properties.

Part III introduces the problem of glass transition. Glass transition is a wider field than just polymer dynamics, and we moved in this perspective of generality. Starting from molecular dynamics simulations of a polymer melt, we linked our results with experimental data avilable in literature collected from the most different materials. From this comparison we extract an universal scaling law which connects the fast local motion of the particles with the global reorganization which take place at longer and slower time scales.

Contents

Introduction

In this chapter we will define polymers, and the ideas that underlie them, in order to understand the basic notions that will be investigated in the following chapters. Talking about polymers is not a trivial task, as they are of great interest to many research fields: technologically they have a wide assortment of practically useful properties, as we can argue from everyday life, where polymers can be met everywhere; for a chemist is not trivial the way to synthetize new polymer; and the conformational and structural aspects of polymer are of great importance also in biological system at the molecular level (proteins or DNA, for example).

The history of polymer physics began in 1920s, when Staudinger (Nobel Prize 1953) introduced the word *macromolecule*, in 1922, to define substances which present a chain structure. Staudinger proposed his viewpoint on the basis of his experimetal research into the structure of rubber; this picture contrasted with the generally accepted theory that rubber consisted of colloidal aggregates of small ring molecules. What shocked the scientists of that period, was the fact that for the first time they met molecules which can reach macroscopic dimension: a molecule of DNA can be measured in metres, for example. This contrasted sharply with their vision of tiny, microscopic particles which work together in order to shape the macroscopic matter; simply, in their vision, there was a mixture of time and length scale which was unbelivable. Without any doubt, the hypothesis of Staudinger fashioned more open minded scientists, who collected more and more evidence on the existence of chain molecules; worth mentioning are the results presented by Staudinger himself in a meeting in Düsseldorf in 1926, and

the important work done by Mark and Meyer [1] (incidentally, ref. [1] is the first monograph on polymeric compounds).

During 1930s the idea of macrmolecules was accepted, and from now on polymer science spread both into physics and chemistry. At that time, chemists had already discovered several polymers, but their microscopic structure had not been understood. The first synthetic polymers appeared during the 19th century, but usually they came in use much later. An example is PVC, discovered by Regnault in 1835 and considered unuseful because of its mechanical properties; afterward, in 1936, the addition of plasticiser made it suitable for numerous applications; nowadays, is one of the most commonly used polymeric materials.

The development of the chemistry of polymer is a monumental challenge between chemists and their ability in tuning the molecular structure to achieve the desidered purpose; a clear example is PET, where a deliberate design of a polymer for a specific purpose (the production of fibres) was achieved with real understanding of what was required. The history of the chemistry of polymer is very stimulating, and a quick overview is given in ref. [2]. But from now on we are going to leave the field of chemistry and to dive into the physics of polymers.

Whilst chemists moved toward the microscopic level to shape macromolecular structure, physicists, following the outstanding intuitions of Flory (Nobel Prize 1974) [3, 4], understood that the key features of polymers could be extracted from more general considerations, discarding their specific molecular composition. This is well described by the the Nobel lecture of Flory, where it is stated: "the chemical basis for the special properties of polymers that make them suitable for so many applications and functions, both in nature and in the artifacts of man, is not therefore to be sought in peculiarities of chemical bonding, but rather in their macromolecular constitution, specifically, in the attributes of long molecular chains. " [5] The basic idea is that the essential physics of macromolecules can be grasped by discarding the chemical details and considering only the statistical properties of the chains, which is related to the flexibility of the molecules,

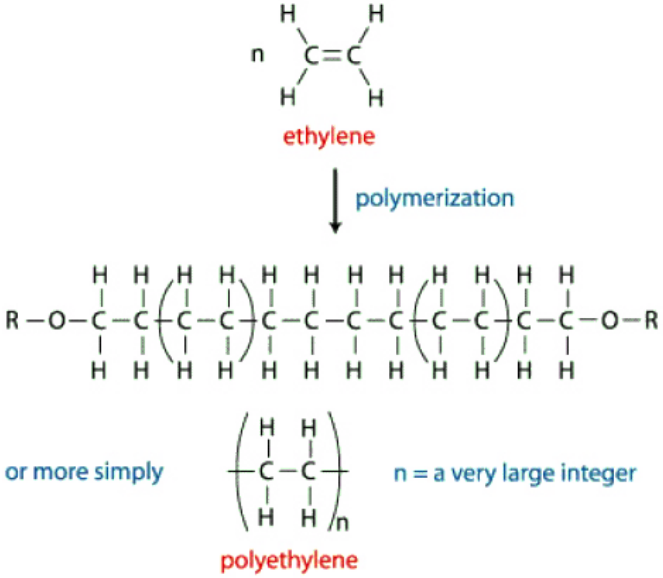

Figure 1: Merging together a large number of equal molecular units of ethylene (via a process called polymerization) we obtain polyethylene [10].

i.e. bond rotations, angle disposition, ...; substantially, the dynamics of polymer chains is reduced to an analysis of their conformations.

This area of research remained rather detached and isolated until 1960s, when some leading theoretic physicists, like Lifshitz[6, 7], Edwards[8], de Gennes [9] introduced the methods of the modern theoretic physics into the field of polymer physics. In particular, Lifshitz developed an approach based on Scrödinger equation with imaginary time; Edwards based its results on path integration, whilst de Gennes introduced the language of renormalization group. Substantially, these three scientists dealt with the problem of many-body and long range interactions, beyond the mean field theories which had characterized the physics since Flory's studies.

This ended in the formation of a harmonious system of simple models and qualitative concepts about the physical properties of polymers on the molecular level, which can be successfully applied in the fields of physical chemistry and molecular biophysics.

0.1 Polymers: giant, multilinked molecules

Polymers, also known as macromolecules, are built up of a large number of molecular units (said monomers) which are linked together by covalent bonds. Usually they are organic compounds. The word comes from the greek *polumeros*, which means *having many parts*: each part is called monomer. A very simple example is the polyethylene: linking together a huge number of equal building blocks, in this case ethylene, we obtain the polymer (figura 1).

The word *plastics*, often associated with polymers, comes also from the Greek, where it means *to form*: this say a lot of thing about the properties of this type of matter, often called *soft matter*.

0.2 The importance of chain connectivity

At first, one might think that any treatment of the properties of a polymer has to emanate from its microscopic chemical structure. So we have to consider in detail the effects of bond lengths, bond angle stretchings, rotational potentials, ecc. Obviously this kind of analysis is specific for every compound and fails in generality.

The idea comes from the fact that as polymer are very long chains, we can watch the chain from a long distance: discussing properties for a lowered resolution, corresponding to length scales in the orders of nanometers, the dependence on the chemical constitution vanished. In such a *coarse grained* picture, polymer chains become equivalent to each other and then exhibit a common behaviour.

For a lowered resolution, polymer chains become thread, characterized only by their stiffness [7, 11].

So the key point in polymer physics consists in considering the chain connectivity.

0.3 Elasticity: entropy

The connectivity, which we revealed in the previous section, bring intriguing consequences. Suppose we have a thread on the desk: we can arrange it in a huge number of different conformations. The differences in energy between the different conformations depend on its stiffness: bending a stiff thread cost much more in energy than bending a flexible one. But we have to consider another aspects of the problem: a full stretched configuration can be realized only in one way; on the other hand, once the energy has been fixed, we can realize a huge number of coiled structure. The number of configurations means entropy.

Experimental measurements agree that the entropy contribution is huge (at least for moderate to large deformations). So, if we stretch a polymer chain, the thread prefers to come back to its coiled structure: an elastic force of entropic origin has raised.

Here another key feature of the macromolecules has been introduced: the large contribution of entropy.

0.4 Phase transitions

One aspect that will be studied in the following pages is the phase transitions of macromolecules. In this work we will consider only linear polymer, usually olefin, i.e. organic macromolecules built only with carbon and hydrogen atoms.

This type of polymers, at high temperature, is in a melt state where the molecules are entangled each other. When the temperature decreases, the motion of the single molecules slows down. Below the melting temperature the motion of the molecules is not sufficient to permit long range rearrangements; in particular, below the *glass transition temperature* the chain appears blocked, and starts a slow rearrangement, which works on time scales of the order of day, week, etc. As the temperature is lowered again, also more local motions start to be blocked.

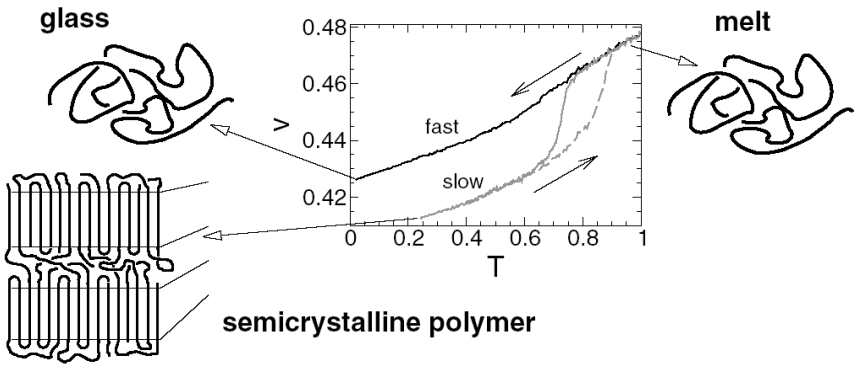

Figure 2: Problematic phase transitions in polymer. Polymer chains are entangled each other, so they need long time for reorganization. Starting from a melt configuration, where polymer chains have a random coil configuration, after a rapid cooling we can freeze the melt configuration, which can survive for geological time scale. To obtain a crystal we need to cool the system very slow. In every case chains are not able to obtain to disentangle completely, so we obtain a semicrystalline solid. In figure is also reported the specific volume against temperature: as we can see, in the glassy state it preserved a melt-like behaviour [12]. For details see [13, 14].

This metastable disordered state is called *glass* (figura 2).

An ordered state, i.e. a crystalline structure, is very difficult to achieve, if not impossible. In fact we have to remember again that macromolecules are build up by a large number of linked units, and the chains need to arrange in an ordered way these units. So two problems arise; first, every chain needs to disentangle from the other: this can be achieved in solutions of polymers, where the chains are far from each other. But a second condition has to be fulfilled: the chain itself *has* to posses an ordered disposition of its building blocks: if this is not true (for example in the case of atactic polymers, where monomers have large lateral groups of atoms disposed irregularly), simply the chain cannot find an ordered disposition of itself, so a crystalline structure is not possible. Again connectivity is the key feature.

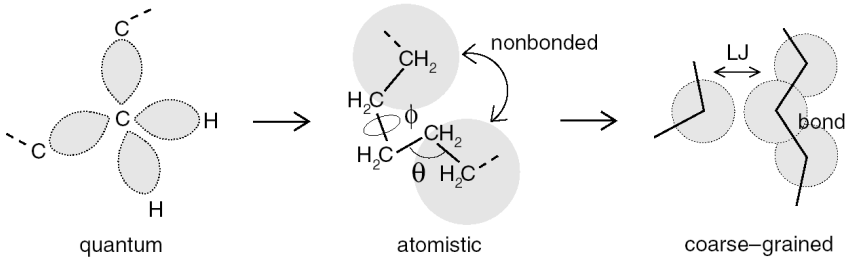

Figure 3: Various degree of simplification needed to obtain simulation which investigate more longer time and space scales [12].

0.5 Simulating polymers

In this work we present extensive simulations in order to study polymer properties. This section will introduce the basic ideas which lay below the simulation of polymer. Here is given only a fast view of the problems linked to the simulation of large molecules, interacting in several, and, sometimes, very complex ways. Nice reviews can be found in literature which address the matter in deeper details, for example [12, 15–22]. One idea could be to start from an *ab initio* quantum mechanical description of the polymer [23]: this approach can be interesting for single and not too long molecules, but as the number of molecules increases, also the computational effort grows. Practically, for the type of studies we are interested in, this approach is not realistic: system has to be tiny and the time scales covered are about 1 ns (figure 3, quantum panel).

For longer time scales and greater systems we need simplifications. A first simplification consists in replacing electronic degrees of freedom by empirical potential shaping bond lengths, bond angles, etc. [24]. Following this approach we can consider each atom separately (*fully atomistic simulations*), or we can perform *united atoms simulations* where groups of atoms will be mimicked. For example: if I am interested in a molecule of polyethylene composed by 100 CH_2 groups (plus 2 CH_3 groups at the chain ends), I can consider a system of 102 C atoms plus 206 H atoms (*fully atomistic*) or a system composed by 100 beads,

where each bead represents a CH_2 group. Following this approach it is possible to cover until 100 ns (figure 3, atomistic panel).

Until now we have described how to simulate polymers, considering their chemical structure. As we said in section 0.2, in polymer we can find properties not related to a particular chemical structure; this suggests that we can perform other simplifications, which go beyond the chemical nature of the constituents. This approach, defined *coarse-graining* [25], leads to the substitution of the faster degrees of freedom (bond lengths, bond angles,etc) by a more general potential which retains only the most basics features of polymers chain [12, 19, 26, 27]: connectivity, excluded volume, stiffness of the chain. This approach permits time scale of ps (figure 3, coarse-grained panel).

Part I

Polymer crystallization

Chapter 1

Polymer Crystals

In what follows we give a rapid review of the problems and the questions around polymer crystallization. Firstly, we describe what a polymer crystal is: how it can be prepared and the major problems arising during the crystallization process. Finally, a glimpse to the theories developed about the argument. The literature on all these aspects is huge; a nice and more detailed description can be found in [28, 29], and references therein.

Before entering into the technical aspects of polymer crystallization, we start with a brief historical background, which highlights controversies and open questions around the ordered state of polymers and, more generally, macromolecules.

1.1 Introduction

The first postulate that polymer crystals have folded chain habits (stacks of layer-like crystallites with thickness in the nanometer-range) was made in 1938 by Storks [30] and confirmed by Keller [31] in 1957.

In the 1960s and 1970s polymer crystals became a major field of research and a focus of interest. Lauritzen and Hoffman [32] pioneered the kinetic approach with secondary nucleation from dilute solution; this model was soon extended to crystallization from the melt [33]. Instead of a kinetic approach, were also

proposed equilibrium theories for chain folding, due to Peterlin and Fischer [34], who considered the effect of thermally activated chain vibrations on the crystal free energy, and Peterson and Lindenmeyer [35], who focused their attention on dangling chain ends that create an entropic energy penalty.

Other models were presented, some of them different from these now sketched, other ones which underline inconsistencies or which improve the models [28]. A famous conference, organized by the Faraday Society in 1979 at Cambridge, became famous as a climatic event [36]. An agreement among the scientists could not be reached, neither at this conference nor afterwards.

In any case, in the years that followed, the model put forward by Lauritzen and Hoffman gained the ascendancy. This model was always confronted by criticism, and some points were taken up and led to modifications, but the foundation remained unchanged. By the late 1980s was broadly applied.

With the onset of 1990s a reconsideration began, triggered by new experimental observation [29]. Nowadays the kinetic approach prevails, but a new version has been proposed by Sadler [37–40]. A completely different picture was engaged in the field by Strobl, whose theory requires no nucleation process, in contrast with the other two, commonly accepted, views. [29, 41].

For most of the theories listed above, a quick introduction will be given in section 1.5.2.

1.2 Factors affecting crystallinity

A crystal consists of a regular disposition, along the three directions of the space, of its constituents. In order to obtain a crystalline phase from a polymer, we need a high degree of order inside the molecule itself. In particular ([42], chapter 11):

Symmetry The symmetry of the chain shape influences both the melting temperature and the ability to form crystallites. Polyethylene and poly(tetrafluoro-

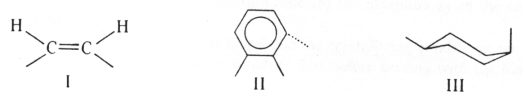

Figure 1.1: Irregular units which detract the chain from linear geometry: I) *cis*-double bond, II) *o*-, *m*-phenylene. III) *cis*-oriented puckered rings [42].

ethylene) are both sufficiently symmetrical to be considered as smooth stiff cylindrical rods.

In the crystal these rods tend to roll over each other and change position when thermally agitated [43–46]. This motion within the crystal lattice, called *premelting*, increases entropy of the crystal and effectively stabilizes it. Consequently, more thermal energy is required before the crystal becomes unstable, and the melting temperature is raised.

Flat or irregularly shaped polymers, with bends and bumps in the chain, cannot move in this way without disrupting the crystal lattice, and so have lower melting temperature values. This is only one aspect. For crystals formation in a polymer, easy close-packing of the chains in a regular three-dimensional fashion is required. Chains containing irregular units, which detract from the linear geometry, reduce the ability of a polymer to crystallize (figure 1.1).

Intermolecular bonding Any interaction among chains in the crystal lattice will help to hold the structure together more firmly and raise the melting temperature. In polyethylene crystals this interaction come from the Van der Waals dispersion forces. Polar groups and hydrogen bonds can provide additional stability. An interesting example come from polyamides. As it can be seen in figure 1.2, nylon-6,6 is suited to have an extended zig-zag conformation which allows regular hydrogen bindings [47]. Instead, the extended zig-zag structure of nylon-7,7 misses one possible hydrogen bonding; but the energy gain is such that the molecule prefers to bend itself in order to allow the hydrogen bond.

Tacticity If a chain possesses large pendant groups, these increase the difficulty of

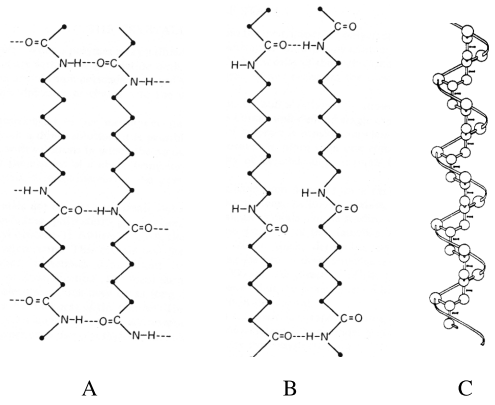

Figure 1.2: Examples of chain dispositions inside the crystal. A) nylon-6,6 completes all hydrogen bonds with a planar configuration; B) the same is not possible for nylon-7,7. C) Isotactic polypropylene has large pendant groups disposed to form a helix (the strip has been added for clearness)[42, 48].

the chains to match each other. This latter problem can be overcome if the groups are arranged in a regular fashion along the chain. An example is polypropylene (figure 1.2), where a helix is formed [49].

Branching If the chain is branched (i.e. it has long, straight pendant groups comparable in length with the dimension of the chain itself), the possibility to obtain crystals is low, due to the difficulty of arranging the long molecular thread departing from the chain.

Molar mass Reducing molar mass, the importance of terminal groups increases. These groups are characterized by high mobility, so the energy required to stimulate chain motion and melting decreases. This makes the crystal less stable.

1.3 Molecular packing

The formation of stable crystalline regions in a polymer requires an economical close packed arrangement of the chains; chains need to approach each other to distances comparable with the distances of low molar mass compounds. If the chain has a cylindrical shape, a good disposition can be seen in figure 1.3, where a coordination number of six unit has been found. Chains with an helical conformation could prefer a disposition with a coordination number of five(figure 1.3).

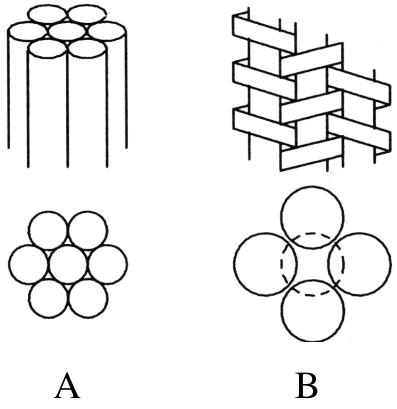

Figure 1.3: Possible packings of the polymer chains inside the crystal: A) molecules with a cylindrical shape prefer an hexagonal packing; instead B) molecules with pendant groups chose a five coordination number; in the latter case the central helix is disposed in a different manner [48–50].

The disposition chosen by the chains depends also on the condition in which the crystallization process has been performed [29].

1.4 Morphology and structure

Polymer crystals are characterized by different morphologies, some of them very complicated. The conditions in which crystallization occurs are critical. We can obtain crystals from melt, heating a glass, from solution, and also during the polymerization process. Typical structures are spherulites and lamellar-like crystals [11, 42, 51]. In this work is not possible to consider the wide variety of morphologies that can be found in nature; for a more detailed review see ref. [48, 52, 53].

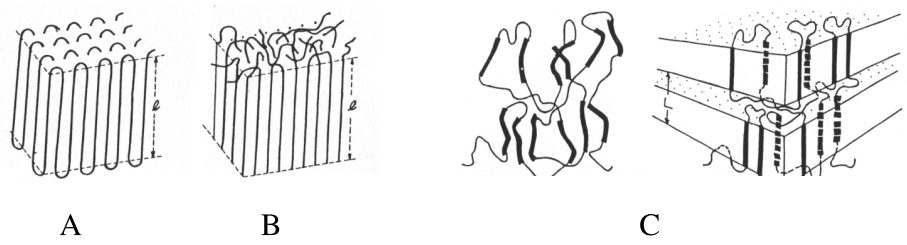

Figure 1.4: Typical lamellar morphologies: A) Adjacent re-entry, B) switchboard model; C) semicrystalline material[42].

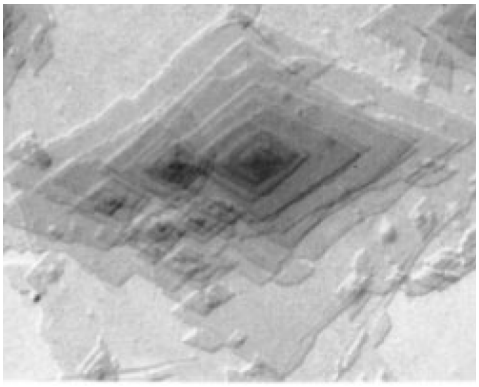

Figure 1.5: A lamellar-like crystal [48].

1.4.1 Crystallization from the solution

The modern era of polymer crystallization began with the discovery [31, 54, 55] that solution grown single crystals are thin platelets, or lamellae, with the molecular backbone oriented along the thin dimension of the crystal(figure 1.5). The morphology of this type of crystals has been extensively investigated in the case of polyethylene, so we will refer to these findings. Lamellae have a thickness of a few hundreds Å, but a single molecule can be several thousands Å long: so the chain is folded inside the lamella, in such a way to have straight sections perpendicular to the basal surfaces [56](see figure 1.4). The models proposed to describe the fine structure of these lamellae and their surface characteristics are two:

1. adjacent re-entry of the chains [36, 57, 58]

2. switchboard model, where the chain re-entry is random [59]

The exact nature of the structure has been the subject of considerably controversy [36]; for this reason different techniques have been employed in order to test the two model, such as Monte Carlo simulation [60], neutron scattering [61, 62], infrared spectroscopy [63]. While the morphology of the single crystal grown from dilute solution may be more regular and resembles the first model, for polymers

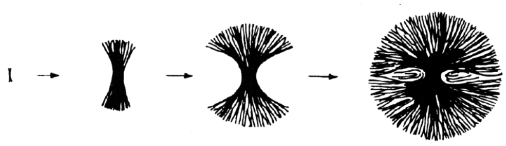

Figure 1.6: Spherulites growing. The threads are rotating lamellae [50].

that are crystallized from less dilute solution the second model seems more appropriate. If the solution is not dilute, the system can be semicrystalline, with sections of the chains inside different crystalline region (figure 1.4).

1.4.2 Crystallization from the melt

Typical of the crystallization from the melt are spherulites. Their name comes from their substantially spherical shape. Spherulites are composed by rotating lamellae which spring out from a common central region (figure 1.6 and 1.7). As lamellae are anisotropic material, spherulites present a typical birefringence, a characteristic Maltese cross optical extinction [11, 50]. Lamellae are linked by sections of chains which belong to different lamellae.

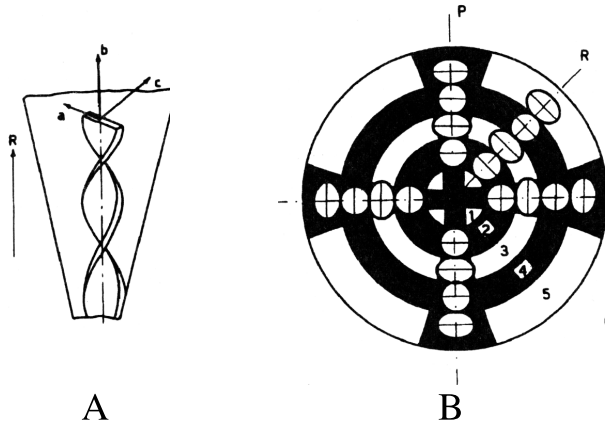

Figure 1.7: Maltese cross in spherulites. The lamellae spring from the center of the spherulite screwing(A); as they are birefringent, a typical pattern rise (B) [50].

1.5 The crystallization process

For complex materials like polymers, crystallization requires a very difficult reorganization of the material on different length scales: monomers have to be in the right position, and so the whole chain; then the chains themselves need to approach each other in the right manner. Obtaining a perfect crystal is difficult in this situation, sometimes impossible, and usually semicrystalline materials result. There is now wide agreement that the morphology of polymer crystals is determined by kinetic rather than equilibrium factors. Although in principle a crystal would equilibrate given enough time, the free energy barriers are so great that the time required is effectively infinite. The kinetic theories assume that the observed growth faces would have a range of possible thickness, each having a growth rate which depends on thickness. The preferred thickness for the crystal is that which maximises the growth rate: hence the kinetic origin of the model. The way the chains follow to form or enter inside a crystal can be divided in [50]:

1. primary nucleation.
2. growth.
3. secondary crystallization.

The first two processes are often referred together as *primary crystallization*. In what follows, a more detailed description will be given.

Equilibrium theory, despite its merits, is usually ignored these days and no further discussion of this approach is given below. The interested reader can refer to the original papers of Peterlin [34, 64–66], Huggins [67, 68], Peterson [35], Zachmann [69]; a brief summary can be found in ref. [28], section 2.4.1.

1.5.1 Primary nucleation

The first step in crystallite formation is the creation of a stable nucleus brought about by the ordering of chains in a parallel array, stimulated by intramolecular

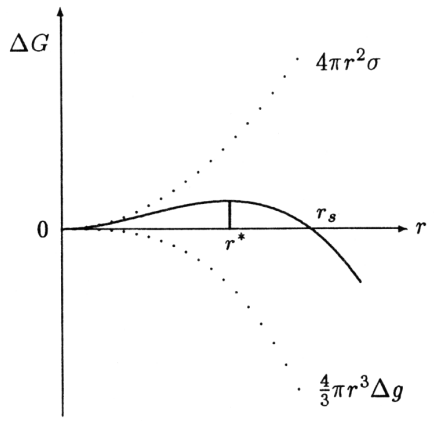

Figure 1.8: Total free energy (straight line). The surface and bulk free energy have been reported for a spherical nucleus (dotted lines); σ is the surface free energy per units of area and Δg is the bulk free energy per units of volume [50].

forces (*homogeneous nucleation*) or brought about by an impurity present, or added, inside the sample (*heterogeneous nucleation*). When a "cluster" of polymer chain has born, two contributions determine his fate. The first contribution is related to the gain in bulk free energy: this contribution is always favourable to crystallization. The second aspect to be remembered is related to the increase in free energy associated with the surface formation. In order to be stable, the nucleus has to be greater than a certain dimension r^* (see figure 1.8): in this situation the nucleus can decrease his total free energy by growing until it has a dimension larger than r_s. Beyond r_s the nucleus is stable: a new crystal starts to grow. The picture represented in fig. 1.8, strictly speaking, make sense only if we consider a spherical aggregation of particles. For a more detailed review on primary nucleation in polymer see Chapter 5.

1.5.2 Growth

The growth of the crystal is one of the most active field of research in polymer crystallization where different theories and hypothesis have been proposed.

The first explanation comes from Lauritzen and Hoffman [32, 70] in 1960s (from now LH theory). Once the crystal is sufficiently large, we can think to the growth surface as a big (usually considered infinite), plain surface. If a chain poses on it, this fact generates a step (figure 1.9, left), so the same problem as presented in the previous section rises: the new surfaces created increase free energy; instead the bulk free energy decrease. The idea was that something like a nucleation happens: this process is called *secondary nucleation*. When a free polymer molecule decides to became part of a crystal, it needs to attach a section of his chain larger than a minimum length, otherwise it detaches. After this condition has been fulfilled, the chain arranges itself on the surface and then other chains can attach close to the nucleus without penalties(Fig. 1.9, right). So the first nucleus starts to spread over the entire surface until he covered it completely: a new molecular layer has been added.

Inside this picture is possible to image three regimes:

1. **Regime I**. The nucleation process is slower than the growth process, so usually only one nucleation event happens before the layer is completely covered [71, 72].

2. **Regime II**. The nucleation process is as fast as the growth process [73–78]. More nucleation event are present before a layer is covered. Moreover, on each spreading layer can start other nucleation event. So this regime

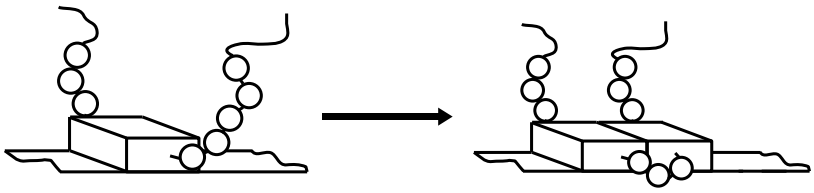

Figure 1.9: Lauritzen-Hoffman theory. When a stem (i.e. a straight section of the chain) attaches onto the surface, a step has been generated (left); this is a nucleation event. After that, other sections of the chain can collapse, so the step grows until all the substrate has been covered.

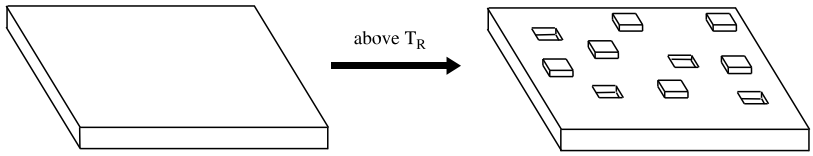

Figure 1.10: Sadler-Gilmer theory. Above the roughening temperature T_R, a plain surface (left) starts to present steps and vacancies (right).

shows several patches in the same layer, which may in turn support further nucleation events.

3. **Regime III** In this regime the niches get so close that patches have little or no time to spread before colliding with another niche [58, 79, 80].

The theory presented until now is the most broadly accepted in the field of polymer crystallization. This means that many observations, corrections, questions about polymer crystallization are phrased in terms of this influential theory. While it is not possible to cite every aspect of this work, we mention some highlights germane to the present study:

1. **Concentration**. In order to grow the crystal need to be fed by always new polymer chains adding to the spreading layer[81–86]. Different concentration can improve some particular aspects which characterize the growth rate [74, 87, 88]: for example, if more than one layer starts to grow on the same substrate, they can collide, generating dangling chain ends. Fractionation effects have also been revealed [89, 90].

2. **Defects**. The description drawn is related to wide planar surfaces, which contain no defects. This can not be considered realistic, and sometimes effects related to defects and the dimension of the crystal arise [91–93].

3. **Theoretical basis**. More technical problems arise if we consider the detailed prediction of LH theory. Critics of the theory have noted the arbitrary

choice of some basic parameters [70, 94] that have been made in comparison to experiments, and the path chosen to describe the process of chain attachment[95–97]. As the theory was considered successful, modifications and extensions were proposed in order to account for multicomponent chains [98, 99], cilia [74, 100], fractionation effects [101], the amount of adjacent reentry [102, 103], the reptation dynamics [104], crystal with curved edges [94, 105, 106].

The LH theory arguments on the expectation that on a wide crystal surface a secondary nucleation event on wide crystal surface decreases the free energy, so that a new polymeric layer starts to spread. Another possibility to decreases the free energy barrier has been proposed by Sadler and Gilmer [37–40] who proposed a superficial roughening where the smooth surface just considered starts to present steps and vacancies above a specific temperature. In this process no nucleation is required.

In the first two approaches (LH theory and Sadler-Gilmer) a section of the chain comes close to the surface, and than the whole chain collapses on the substrate. Wunderlich and Metha [90] supposed that (especially for low mass polymers) the leading process is the molecular nucleation: *firstly* the single molecule forms a stable nucleus, *then* it approaches to the surface. This means that chains too short, which can not form a stable nucleus, will not enter inside the crystal: this can be observed also experimentally.

Another interesting observation comes from Hikosaka [107, 108]. The growth front of a polymer can be sketched as a strip with a definite thickness, but an infinite width. In such a surface the chain has a penalty if it approaches to upper and bottom edges, so firstly it enters onto the surface, then it rearranges itself until it reaches the two edges. This reorganization works only within few layers below the growth surface.

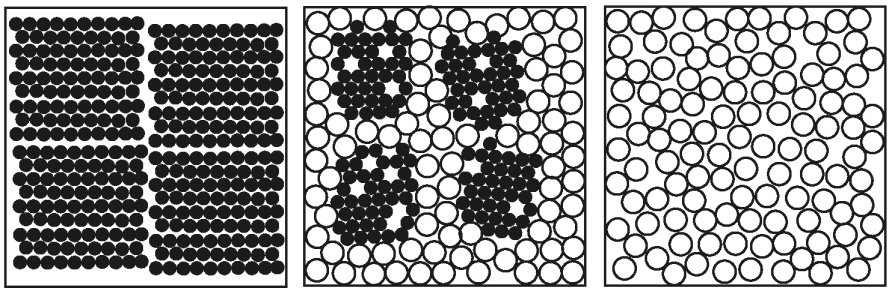

Figure 1.11: Sketch of the changes in the internal layer structure: liquid-like packing in the mesomorphic state (right), pattern of crystal blocks after the transition in the granular state (center), lamellar crystals with mosaic block structure (left). [41].

1.5.3 Secondary crystallization

Usually, the polymer crystallization stops resulting in a semicrystalline material, where ordered regions are bounded by disordered ones. In this situation, a slow process occurs which tends to give rise to more perfect crystals and increasing crystallization over time. The secondary crystallization involves a slow structural reorganization of the material.

1.5.4 Some final remarks

An alternative picture of polymer crystallization has been furnished by Strobl [41] and can be seen in fig. 1.11. The leading idea is that a mesomorphic phase is present when the sample is cooled below the melting temperature, before it achieves an ordered disposition of the chains typical of the crystal. In this picture the chains are disposed along a preferential direction; this preferential direction is not retained for long distances, so the sample has a granular appearance with clusters of oriented chains close to each other, moving indipendently inside a matrix of chains which do not belong to any cluster (middle picture in Fig.1.11) ; these clusters are internally very mobile both in reorganization and in thickening. Lowering the temperature again, make the cluster grow adsorbing other free

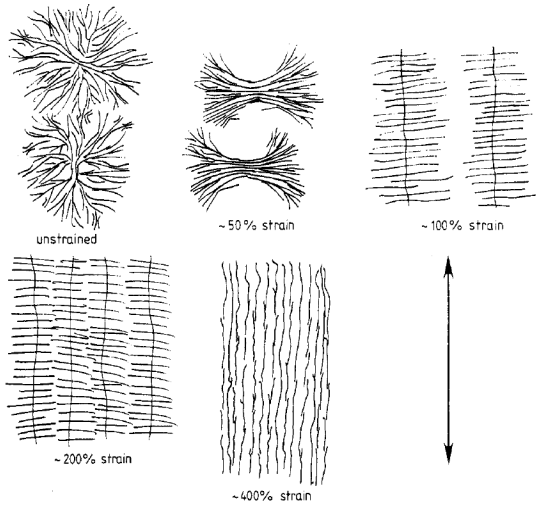

Figure 1.12: Effect of strain on crystal morphology. For strain equal zero a spherulitic pattern would be found. As the strain increases fibrillar structures appear [52].

chains. When the matrix of free chains is substantially disappeared, the clusters start colliding with each other. Their motion is now very difficult, and they start merging together forming a crystal. The crystallization, in this picture, is a collective process, and no nucleation is present. Evidence of the existence of these initial clusters of molecule, would be provided by a microscopic blocky structure of the lamella, which has been actually observed[145, 146].

Spinodal decomposition is often discussed in connection with polymer crystallization [11, 147]. The term "spinodal decomposition" is borrowed from the field of polymer mixture [148–151], and happens when two *chemically* different polymers start phase separating leading to interpenetrating continuous domains when the concentration is near a critical value.A similar situation seems to occur when polymers crystallize where the crystallized and amorphous forms of the polymer play the roles of the phase separating species in phase separation. Notably, we are dealing with a one-component sample; the key issue is the different mobility and density of the polymer segments in the crystalline and non-crystalline domains [152].

Although the idea of spinodal mode of crystallization is attractive, but the evidence supporting this phenomenon is rather limited (for a detailed list of samples,

refer to references cited in [122] and [152]).

Another form of crystallization is the crystallization under strain [48, 52, 109–115]. Applying a strain lead to a different forms of molecular organization: for an isotropic melt usually a spherulitic pattern is found; as the strain increase a fibrillar structure starts to appear. It is interesting to see that nucleation and growth rates, in materials subjected to a strain can be several orders of magnitude larger than those of unstrained materials.

Astonishingly, because of the weak effect it has on polymer melts, orientation effects can be also obtained by means of magnetic fields [116–119].

Chapter 2

Simulation Model

In this chapter we will explain the details related to the model used during the simulations. Details on how simulations have been performed, will be given at the beginning of each of the following chapters.

2.1 System under examination

The system under investigation consists in a single polymer chain in solution. The aim of the simulations is to investigate the early stages of the crystallization process. Both structural and dynamic properties of the chain will be analysed.

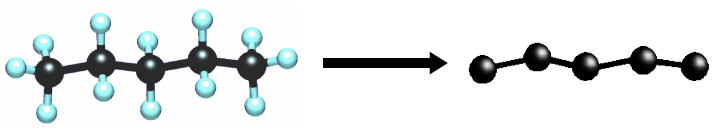

Figure 2.1: The chain is described as a sequence of beads, where each bead represents a single methylene CH_2 group. No distinction is made between internal methylene CH_2 groups and terminal methyl CH_3 groups [120].

Table 2.1: Parameters of the force field.

Parameter	**Value**	
	reduced units	SI units
ϵ	1	0.112 kcal/mol
σ	1	4.04 Å
m	1	14.03 g/mol
Γ	1	0.455 Hz/mol
k_r	51005	350 kcal/mol Å^2
r_0	0.38	1.53 Å
k_θ	535.71	60 kcal/mol
θ_0	109°	109°
k_1	26.96	3.02 kcal/mol
k_2	-5	-0.56 kcal/mol
k_3	23.04	2.58 kcal/mol

2.2 Chain representation

The chain is described as a sequence of beads, where each bead represents a single methylene CH_2 group. No distinction is made between internal methylene CH_2 groups and terminal methyl CH_3 groups in order to obtain a slight improvement in efficiency [121]. For long chains this approximation is fair. The local interactions shaping the chain are defined by the potentials

$$U_{\text{bond}}(r) = k_r(r - r_0)^2 \tag{2.1}$$

$$U_{\text{angle}}(\theta) = k_\theta(\cos\theta - \cos\theta_0)^2 \tag{2.2}$$

$$\begin{aligned} U_{\text{torsion}}(\phi) = {} & k_1(1 - \cos\phi) + k_2(1 - \cos 2\phi) \\ & + k_3(1 - \cos 3\phi) \end{aligned} \tag{2.3}$$

$U_{\text{bond}}(r)$ is a harmonic spring potential defined for every couple of adjacent beads, r being their distance and r_0 the equilibrium bond length. $U_{\text{angle}}(\theta)$ is defined for every triplet of adjacent beads, θ being the angle between the corresponding bonds and θ_0 its equilibrium value. Finally, $U_{\text{torsion}}(\phi)$ is defined for every quadruplet of adjacent beads and ϕ is the dihedral angle between the planes defined by the corresponding three adjacent bonds. Pairs of beads not interacting by any of the preceding potentials interact by means of a Lennard-Jones potential

$$U_{\text{LJ}}(r) = 4\epsilon \left[\left(\frac{\sigma}{r}\right)^{12} - \left(\frac{\sigma}{r}\right)^{6} \right] \tag{2.4}$$

with a cutoff radius $r_{\text{cut}} = 2.5\sigma$. The set of parameters of the above force field are taken from ref. [122] (see table 2.1). The corresponding time and temperature units are given by $t^* = 2.21$ ps and $T^* = 56.3$ K. All the results will be presented in terms of reduced units. For that set the single-molecule crystal melts at $T_m = 11 \pm 0.2$ in the limit of vanishing heating rate [122, 123]. This value is exceedingly high and calls for refinements of the force field. However, since we are interested in studies carried out by the same force field [121–124], these adjustments are beyond the present purposes. By the way, similar problems were also noted in other studies on PE single-chain crystals which exhibited global orientational order already at 550 K by using the Dreiding potential [125].

2.3 Solvent

The solvent is mimicked by suitable friction and random forces acting on the monomers. The dynamics is described by the Langevin equation

$$\ddot{\mathbf{r}}_i = -\nabla_i U - \Gamma \dot{\mathbf{r}}_i - \mathbf{W}_i \tag{2.5}$$

where $\mathbf{r}_i$ denotes the position vector of the i-th bead, $\nabla_i U$ is the sum the internal forces acting on it, $\Gamma \dot{\mathbf{r}}_i$ is the frictional force and $\mathbf{W}_i$ is a gaussian noise:

$$\langle \mathbf{W}_i(t) \cdot \mathbf{W}_j(t') \rangle = 6\Gamma k_b T \delta_{ij} \delta(t - t') \tag{2.6}$$

The friction and the random forces account for the solvent and set the temperature via the proper fluctuation-dissipation theorem.

2.4 Integration scheme

Eq. 2.5 is integrated by means of the velocity Verlet algorithm [126–128]:

1. Firstly compute the new position r at time $t+\delta t$, knowing position, velocity v and acceleration a at time t:

$$r(t+\delta t) = r(t) + v(t)\delta t + \frac{1}{2}a(t)\delta t^2 \tag{2.7}$$

2. Then compute velocity at mid-step:

$$v(t+\frac{1}{2}\delta t) = v(t) + \frac{1}{2}\delta t a(t) \tag{2.8}$$

3. Compute acceleration knowing the new positions $r(t+\delta t)$

4. Finally, complete the velocity step:

$$v(t+\delta t) = v(t+\frac{1}{2}\delta t) + \frac{1}{2}\delta t a(t+\delta t) \tag{2.9}$$

The time step used is $\delta t = 0.001$.

Chapter 3

Primary Nucleation and Melting

After the general description given in chapter 1 regarding polymer crystallization, here we focus our attention on the early stages of the formation of an ordered crystalline structure. Before entering into the results gained with our simulations [129, 130], a brief introduction to this field is furnished. After that, we go on to describe the behaviour of a single polymer chain, composed by 500 monomers, in solution via MD simulations. For details on the model, readers can refer to chapter 2. Here we are interested in the crystalline structure obtained, and in the processes followed in order to come to the final state. A description of the whole process in terms of Free Energy Landscapes will be given in chapter 4. At the end of this chapter a concise study of the melting process is presented. The results here showed, appeared in ref. [129, 130].

3.1 A glimpse at the birth of a crystal

In this section an account of the experimental observations involving the early stages of crystallization is reviewed. Most of them appeared recently, because of the development of techniques that make possible to extract local information from the sample, instead of global ones (such as growth rate). Incidentally, it is worth noticing that the Lauritzen-Hoffman theory (the most accepted theoretical

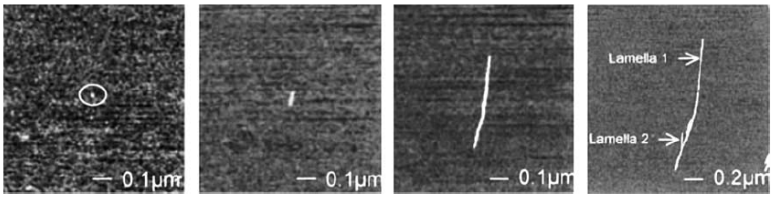

Figure 3.1: The birth of a homogeneous nucleus which develops into a lamella.[131].

description) relies its predictions on the growth rate measurements almost exclusively; thus, the new developed techniques are able to open a completely new perspective on the microscopical picture of crystallization.

3.1.1 Early stages

The nucleation can start when a density fluctuation in the sample is sufficient to provide a nucleus which is wide enough to begin to spread out (see chapter 5). This starting event, due to density fluctuation, is called *homogeneous nucleation*. Fig. 3.1 presents one example of homogeneous nucleation: the dot in the left hand picture is a nucleus which subsequently develops into a single lamella [131]. As it is shown in the picture on the right hand side, in the case of a melt-grown crystal, the first branches develop when the lamella reaches a size of the order of 1 μm. The branching is repeated also at later stages and the final structure is a spherulite with a pair of "eyes" (the two black holes) at its center (fig. 3.2). Another way to start nucleation is the presence of an heterogeneity in-

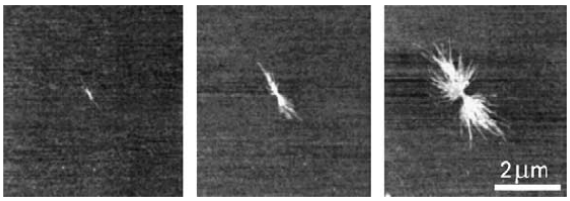

Figure 3.2: Homogeneously nucleated growing spherulite [132].

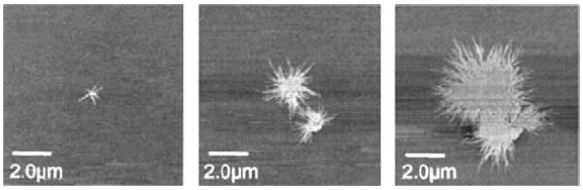

Figure 3.3: Heterogeneously nucleated growing spherulite [132].

side the sample. This case is called *heterogeneous nucleation*. Now, more nuclei start spreading at the same time; as it can be seen in fig. 3.3, several lamellae develop simultaneously, emanating from the surface of the heterogeneity; the nucleus shows a quasispherical symmetry and this symmetry is retained up to the end. An interesting feature of the growing spherulites, see figure 3.4, is the existence of dominant and subsidiary lamellae: in the first image a bounce of rapidly advancing lamellae is shown. Afterward, an in-filling process starts, by means of subsidiary lamellae. The concept of dominant and subsidiary lamella was introduced by Bassett and co-workers in order to explain TEM experiments [133]. Nowadays, the same process can be seen by AFM [134, 135], micro-beam X-ray scattering [136], SAXS [137], the linear attenuation coefficient of light [138, 139].

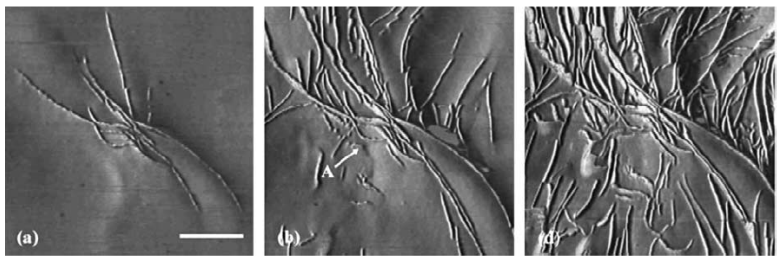

Figure 3.4: AFM images related to the in-filling process which happens during the growth of spherulites. [134].

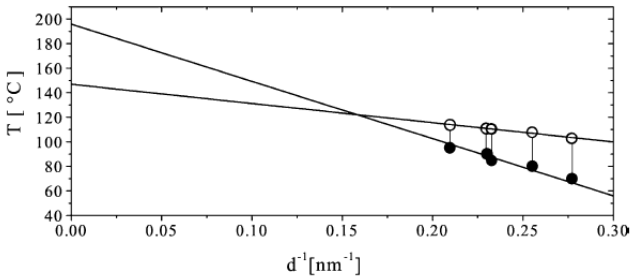

Figure 3.5: sPPc015: crystallization (filled symbols) and melting (open symbols) line versus d_c^{-1} [155].

3.1.2 Crystal structure

The crystals produced during the crystallization process, can be characterized by means of their thickness. Several investigations describe a very interesting picture of the thickness evolution in time. Usually a time invariant crystal thickness is observed [29, 140–142], but if a polymer has longitudinal chain mobility [143] in the crystalline state, it shows spontaneous crystal thickening at the crystallization temperature. This is true for polyethylene, whose crystal thickness increases with time [144].

Another well-known feature of lamellae is their blocky substructure [145, 146, 153, 154]: this means that looking at a lamellae very closely, a granular structure is visible. This is the reason for the theory proposed by Strobl (section 1.5.4).

Despite of the uniform lamellar thickness obtained at a certain temperature, this does not imply an analogous uniform stability of the crystallites [155]. Actually, conventional views often associated melting point variations with a corresponding distribution of lamellar thickness only, but recent experiments now point to further causes. For example, subsidiary lamellae melt before dominant lamellae [156]; in general crystals formed later melt much earlier [157–161]. Other important aspects are the interactions with neighbors [162], and stability within a single lamella [163, 164].

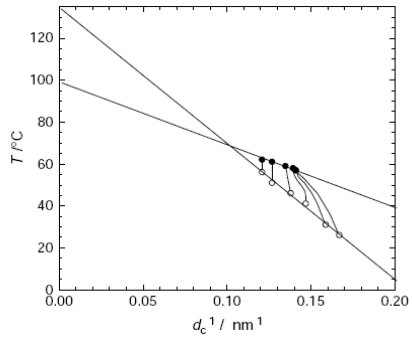

Figure 3.6: PEc014: crystallization (filled symbols) and melting (open symbols) line versus d_c^{-1}. the connecting lines show the temperature dependence of d_c^{-1} [169].

3.2 Melting: the presence of metastable phases?

The melting of a polymer is usually described by means of the Gibbs-Thompsom equation:

$$T(d_c) = T^{\infty} - \frac{2\sigma_{ac}T^{\infty}}{\Delta h_f d_c} \tag{3.1}$$

where Δh_f is the heat of fusion and σ_{ac} the surface free energy, d_c the crystal thickness and T is the melting temperature. This equation suggests plotting the melting points as a function of d_c^{-1}. It also suggests using the same representation for the relation between the crystallization temperature and the thickness of the resulting crystal. In figures 3.5 and 3.6 are given two examples of the plot: the experimental points are reported together with their crystallization and melting lines. In addition, thin lines which connect respective points on this two lines are drawn: the lines are vertical when the thickness remains constant and are curved when the crystal thickness increases during heating.

As the two lines come to an intersection, it is interesting to understand what happens around the intersection points. In figure 3.7 is possible to see that: the points deviate from the crystallization line before reaching the intersection point.

This representation with the crystallization and melting line is also useful to study the behaviour of polymers with the presence in the chain of co-units

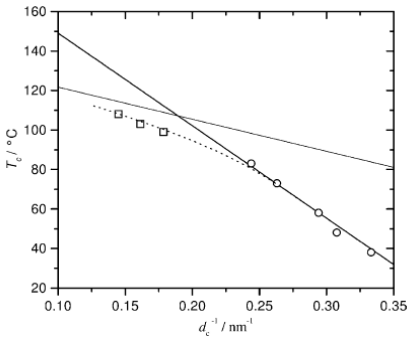

Figure 3.7: sPPc020: relation between crystallization temperature and crystal thickness near the point of intersection between the melting and the crystallization line. [41].

[144, 155, 165, 166], or stereo defects that cannot be included in the crystal. Polymer mixed with low molar mass diluent [140] or a second non-crystallizable polymer [167] have also been studied with this technique. In the same way the effect of the molar mass of the polymer has been considered [168]. In many of this experiments an attractive feature is found: the remarkable constancy of the crystal layer thickness which depends only on the crystallization temperature. Another interesting aspect of melting is the the recrystallization process: heating an isothermally crystallized polymer is not always accompanied just by melting of the crystallites, but in many cases, the melting is immediately followed by formation of a new crystal. In this case two different scenarios are found:

- if the crystal is formed at high temperature, which means near the intersection between crystallization and melting line, the melting is followed by a new crystallization process [170], before the final melting. If the sample is heated fast enough, on the order of $10Km^{-1}$, the sample melts without recrystallization.

- For low temperature crystals, the situation is quite different. Now is not possible to identify a melt-crystallization-melt process, but after the "first" melt the system starts a continuous crystal thickening, which stops only

when the final melting arise [171–173]. In this case, in order to avoid the recrystallization, the heating rate has to be very high [174], such as $10^5 Km^{-1}$.

The experimental description of the melting-crystallization by means of the crystallization and melting lines addresses Stobl's idea of the presence of a mesomorphic phase which turns up between the crystal and the point of melting [29, 41, 172].

Is there any evidence of this (or these) mesomorphic phase(s) in literature?

Early in the 1990s, Keller and his co-workers [175] carried out crystallization experiments on polyethylene at elevated pressure using a polarizing optical microscope. Crystals nucleate into a hexagonal phase, and then grow to sizes in the micrometer range before they transform into the orthorhombic phase after a statistically initiated, second nucleation step. The authors interpreted their observation as an example of Ostwald's rule of stages [176]. The presence of an hexagonal metastable phase has also been revealed in other experiments on PE [177–179], sometimes in connection with the "rotator phase", which is found in n-alkanes [180, 181]; this mesophase is also present in other polymers, such as sPP [182–187].

3.3 Introduction

In order to understand the events that take place in the early stage of the crystallization process, we perform large scale molecular dynamic simulations. Our target is a deep analysis of the crystallization from very dilute solutions, where is expected that each crystal is obtained initially from the folding of one single molecules. Afterward, other chains can depose themselves on the one molecule nucleus in order to develop, at long time, the typical lamellar crystal [124].

For oligomers, once-folded or extended conformations of the chain are observed in the crystallized melts of relatively long monodisperse n- alkanes (C_nH_{2n+2}, $150 \leq n \lesssim 390$) while up to four foldings per chain were observed in dilute

solutions [188–191]. The number of foldings increases with supercooling. It is believed that for *multi-chain* crystallites the extended conformation of the single chain corresponds to the global minimum of the free-energy, which may be reached from the original kinetically-selected minimum via a series of transitions through less and less folded conformations (each corresponding to different local minima) if the involved free-energy barriers can be overcome [189].

Transitions are evidenced by heating solution-grown crystals ($n = 168, 240$ [189, 192]) or melts ($n = 198, 246$ [190]) . Furthermore, aging behavior yielding transitions from folded to extended states were observed in the melt of n- alkanes by prolonged isothermal crystallization at small supercoolings ($198 \leq n \leq 390$ [188, 190]).

The primary nucleation of polymers and oligomers has been investigated in the melt both by experiments [190, 193] and simulations [194]. Nonetheless, very few groups have challenged the rather problematic and related issue of the preparation of single-molecule single crystals [195, 196]. Understanding if the primary nucleation is kinetically or thermodynamically controlled is nontrivial.

The difficult characterization of the primary nucleation regime in dilute solutions motivated several simulations [121, 123–125, 129, 197–205]. For relatively short chains, the primary nucleation of single-molecule n-alkanes with a number of monomers $N = n \leq 300$ were found to end up in the global minimum of the free-energy , i.e. in thermodynamic equilibrium, at a quench depth $\Delta T \equiv T_m - T \sim 0.2\ T_m$, where T_m is the melting temperature [123, 124]. However, the eventual kinetic arrest of the nucleation in one state during the primary nucleation of longer single-molecules cannot be excluded due to the increasing number of entanglements and, consequently, larger energy barriers.

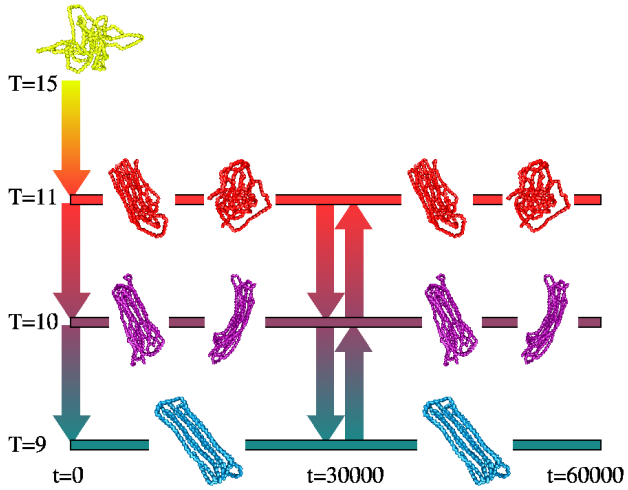

Figure 3.8: Thermal histories leading to the final temperature T_f

3.4 Simulation details

The model has been already presented in chapter 2. The runs are performed according to the following protocol: seventeen random chain conformations are initially equilibrated at $T_{eq} = 15$ for at least ten times the time needed for the self correlation function of the end-to-end vector to vanish. The equilibrated chain does not exhibit any local orientational order (see Sec. 3.5 for details).

The final temperature T_f is reached via different thermal histories (see fig. 3.8):

- instantaneous direct quenches $T_{eq} \rightarrow T_f$.
- instantaneous quenches with intermediate annealing at T_{ann}, $T_{eq} \rightarrow T_{ann} \rightarrow T_f$. Annealing times were 3×10^4 at $T_{ann} = 9$, 10 and 6×10^4 at $T_{ann} = 11$.

The overall scheme of the thermal paths is summarized in Fig. 3.8. The total number of direct quenches (17) and quenches with intermediate annealing leading to one specific T_f was 28.

Memory effects were also investigated by preparing a sample in the “all-trans”

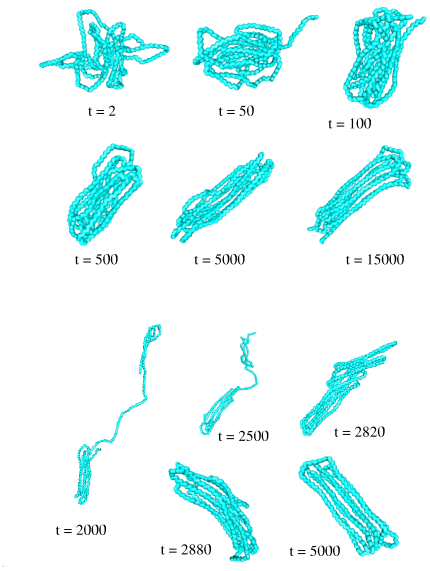

Figure 3.9: Wire-frame snapshots of the crystallization of a single polyethylene chain with $N = 500$ monomers for two different initial states: chain equilibrated at $T_{eq} = 15$ and quenched at $T_f = 9$ (top); chain initially in the fully-stretched configuration (all-trans) and isothermally annealed at $T = 9$ (bottom). For the latter case note the presence of initial distinct nucleation sites merging at later times.

fully-extended conformation and isothermally annealing it at $T = 9$. Having reached T_f, data were collected during evolution times of 3×10^4 at $T = 9$, 10 and 6×10^4 at $T = 11$. The all-trans conformation was monitored after the initial preparation for 3×10^4 time units.

The force field enforces the local stiffness of the chain yielding a Kuhn segment length $\ell_{\rm k} \cong 1.2$ [11, 51], corresponding to segments with about four beads. Therefore, the polymer is sketched as a succession of about $N_{\rm k} = 125$ rigid segments.

3.5 The crystallization process

The kinetics of the crystallization process is nontrivial and depends on the chain conformation. Fig. 3.9 shows some representative snapshots evidencing that the chain gathers relatively long straight sections (the so-called stems) to form the overall ordered structure.

The nucleation may involve either the whole chain or separate portions merging at later times by reeling in their connector. The latter process has been already noted for much longer chains ($N = 2000$)[122, 123]. Fig. 3.9 shows that

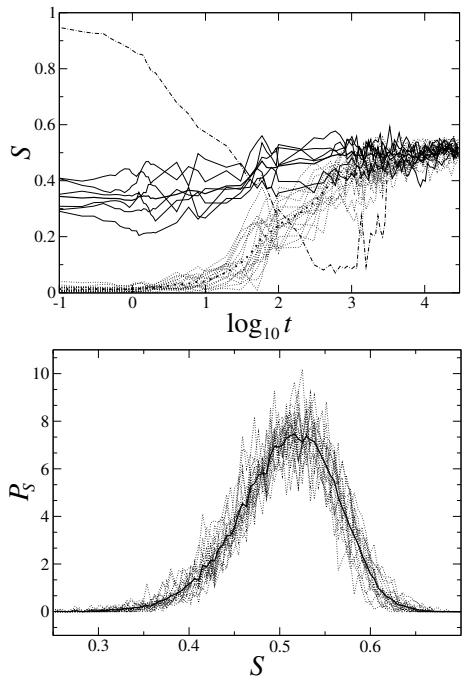

Figure 3.10: Top: time evolution of the order parameter S (eq.3.3) for all the investigated thermal histories leading to $T_f = 9$ (top): direct quenches from $T_{eq} = 15$ (dotted lines) and quenches after annealing at $T_{ann} = 10$ (solid lines). The thicker lines are the average order parameter for each set of curves. The dot-dashed line refers to the chain initially in the fully-stretched configuration and then annealed at $T = 9$. Bottom: order-parameter distributions P_S (dotted lines) gathered for times $t > 2 \times 10^4$ for all the thermal histories. The solid line is the average distribution.

it also occurs in shorter chains. In principle, owing to the different scenarios of the nucleation, the kinetic arrest in different states cannot be ruled out .

Tracking the amount of alignment between different sections of the chain by means of suitable order parameters is of help in order to assess that hypothesis. To this aim, one defines

$$\mathbf{b}_i = \frac{\mathbf{r}_{i+1} - \mathbf{r}_{i-1}}{|\mathbf{r}_{i+1} - \mathbf{r}_{i-1}|} \tag{3.2}$$

$\mathbf{b}_i$ is thus a unit vector locally aligned with the chain backbone. The order parameter is defined as [121]

$$S = \langle P_2(\mathbf{b}_i \cdot \mathbf{b}_j) \rangle_{i>j} \tag{3.3}$$

where $P_2(x)$ denotes the second Legendre polynomial in the variable x and the average is computed for all the pairs of inner monomers. Fully disordered and ordered states yield $S = 0$ and $S = 1$, respectively.

Fig. 3.10 (top) shows the time evolution of the order parameter S of the chain for all the investigated thermal histories leading to $T_f = 9$. Direct quenches

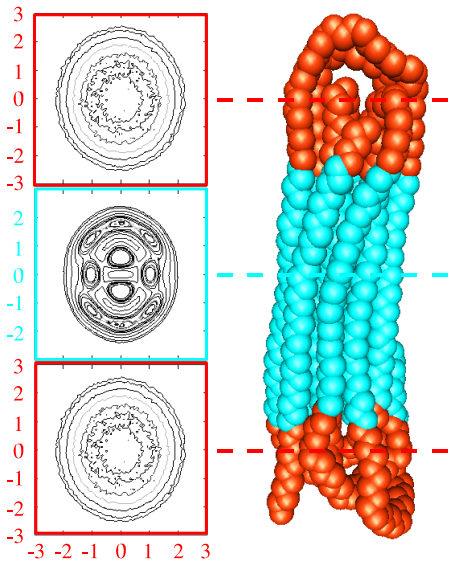

Figure 3.11: Tomography of the crystal state with a number of stems $\mu = 10$. The azure zone is the stem region. The red zones are the two caps. The left-side column plots the averaged density profiles in the cross sections marked by the dashed lines. Note the absence of ordered structures on the crystal surface and the two caps.

from $T_{eq} = 15$ and quenches after the annealing at $T_{ann} = 10$ exhibit at short times ($t \lesssim 5$) the pre-quench order parameters $\langle S \rangle_{T_{eq}} = (1.31 \pm 0.03) \times 10^{-2}$, $\langle S \rangle_{T_{ann}} = (3.4 \pm 0.18) \times 10^{-1}$, respectively. For the all-trans initial conformation S drops from the unit value.

Note that the spread of the curves is much larger at intermediate times than immediately after the quench evidencing that the crystallization paths may be somewhat different from each other. Nonetheless, at long times the paths become closer and , after a transient period of about 2×10^4 time units, independently of the thermal history, the chain exhibits the order parameter $\langle S \rangle_{T=9} = (5.10 \pm 0.18) \times 10^{-1}$, i.e. at long times the time average of a single history coincides within the errors with the ensemble average over all the different histories. Henceforth, the chain conformations at $T_f = 9$ after the transient period will be referred to as belonging to the crystalline *final state*.

Fig. 3.11 shows one conformation of the final state. It is a well-defined lamella with two small-sized caps where the loops connecting the stems are localized. The stems have approximately equal length. In Sec. 3.6 it will be seen that they are

arranged into a regular, hexagonal pattern and their number μ is well defined ($\mu = 10$), i.e. the general features of the final state are largely independent of the thermal history.

In fact, Fig. 3.10 shows that the order-parameter distributions P_S for the final states of all the thermal histories are quite similar within the statistical errors. P_S peaks at $S \sim 0.52$ evidencing considerable chain order. The distribution is skewed to the low S-values. This is ascribed to the disorder localized in the two crystal caps as well as in the crystal surface (see Sec. 3.6 and fig. 3.11).

To characterize the different kinetic pathways leading to the final crystal state the inertia tensor of the conformations was considered. The principal axes $\{\mathbf{1}, \mathbf{2}, \mathbf{3}\}$ are ordered according to the magnitude of the corresponding eigenvalue which are labelled as I_1, I_2 and I_3, I_1 being the largest one. Fig.3.12 (top panel) plots the time -dependence of I_1 of both selected quenches at $T = 9$ and the isothermal annealing of the initially fully-extended conformation at the same temperature.

The plot gives insight into the typical structural changes leading to the final crystal state. It is seen that the changes occur as fast transitions in about few hundreds of time units between states with different, discrete I_1 values. Such states are identified by visual inspection as ordered conformations with different number of stems. At long times all the pathways converge to a single state with $I_1 \cong 10^4$, i.e. the final state with a number of stems $\mu = 10$. The time -dependence of I_1 evidences transitions with changes of the number of stems $\Delta\mu = \pm 1, -2$ and even a quasi-transition with $\Delta\mu = -4$, i.e. two transitions with $\Delta\mu = -2$ being very close to each other. Transitions with $\Delta\mu = \pm 1$ involve stems terminated by one of the two chain ends. Transitions with $\Delta\mu = -2$ involve stems built by inner portions of the chain. Transitions with $\Delta\mu = +2$ were not observed. Notice that the approach to the final state ($\mu = 10$) is not monotonous, e.g. in Fig.3.12 a transition is seen from one state with $\mu = 11$ to one with $\mu = 9$. Fig.3.12 (middle panel) shows selected snapshots of one transition with $\Delta\mu = -1$ involving

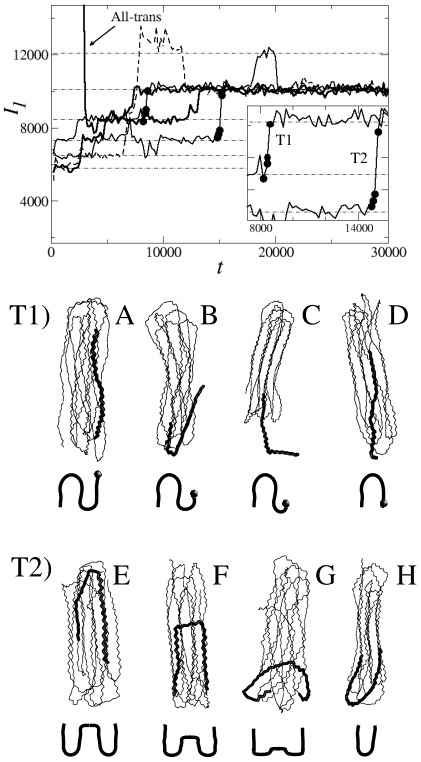

Figure 3.12: Kinetic pathways of the crystal formation. Top: Pathways of selected thermal histories leading to the final crystal state as characterized by the time dependence of the largest eigenvalue of the inertia tensor I_1. The time starts 10^2 time units after either the quench at $T = 9$ or, for the "all-trans" curve, the beginning of the isothermal annealing of the fully-extended conformation at $T = 9$. The horizontal dashed lines mark the I_1 values corresponding to crystal structures with a number of stems equal to (from the top to the bottom) $9, 10, 11, 12, 13, 14$. The inset is a magnification of two transitions involving the disappearance of either one (T_1) or two stems (T_2). Middle: Snapshots of the molecular conformations during the T1 transition occurring at times 8200 (A), 8420 (B),8450 (C),8600 (D) being marked by dots in the top panel. The cartoons below the wire-frame view sketch the rearrangements of the thick portion of the chain end involved in the transition. Bottom: Snapshots of the molecular conformations during the T2 transition occurring at times 14800 (E), 14900 (F),15000 (G),15200 (H). The cartoons below the wire-frame view sketch the rearrangements of the thick portion of the chain involved in the transition. Notice that the stems disappearing in both the T1 and T2 transitions are located on the crystal surface.

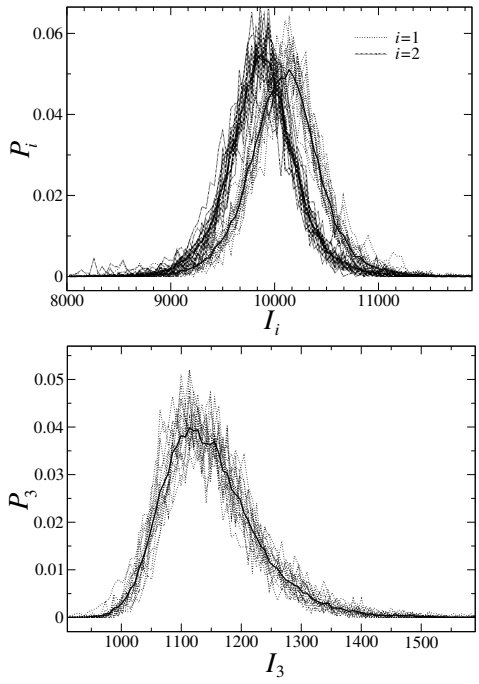

Figure 3.13: The distributions of the moments of inertia along the transverse x^1, x^2 (top) and the longitudinal x^3 (bottom) axes in the final state at $T = 9$(see Fig. 3.11) . The dotted lines refer to the different thermal histories . The solid lines are the averages.

a chain end (transitions with $\Delta\mu = +1$ are quite analogous to the same sequence in reverse time order). Fig.3.12 (bottom panel) shows selected snapshots of one transition with $\Delta\mu = -2$. It is interesting to note that the stems disappearing (or being created) during the transitions are always seen to be located on the crystal surface.

3.6 The crystalline final state

3.6.1 Moments of inertia.

In order to get a deeper understanding of the structure of the crystallized chains, the inertia tensor of the configurations in the final state at $T = 9$ was analyzed. Fig. 3.13 plots the distributions of the three eigenvalues I_1, I_2 and I_3 for all the thermal histories. The principal axes $\{\mathbf{1}, \mathbf{2}, \mathbf{3}\}$ are ordered according to the magnitude of the corresponding eigenvalue. The average values over all the thermal histories are $\langle I_1 \rangle = 10097 \pm 58$, $\langle I_2 \rangle = 9885 \pm 51$, $\langle I_3 \rangle = 1148 \pm 11$. Since

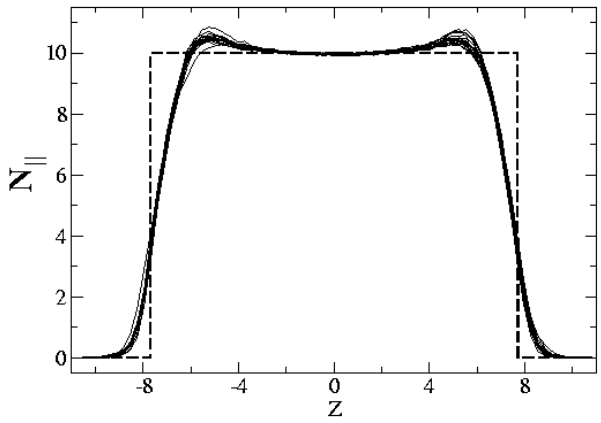

Figure 3.14: The number of intersections of the chain with the plane at $x^3 = z$, $N_{||}(z)$, in the final crystalline state at $T = 9$. The plane is perpendicular to the approximate cylindrical symmetry axis x^3. The different curves refer to all the thermal histories ending at $T = 9$. The dashed line is the distribution corresponding to the ideal case of ten parallel and fully extended stems with fifty monomers each. The number of stems μ is equal to $N_{||}(0) = 10$. Note the steep decrease at the end region evidencing the small size of the loops connecting the stems.

$\langle I_1 \rangle \gtrsim \langle I_2 \rangle \gg \langle I_3 \rangle$, the ellipsoid of inertia of the crystal exhibits approximate cylindrical symmetry around the **3** axis, as it may be seen by visual inspection (see Figs. 3.9, 3.11, 3.15). Fig. 3.13 shows that the shape of the distributions for the largest eigenvalues P_1 and P_2 is nearly symmetric with small width whereas the distribution for the smallest eigenvalue P_3 is rather asymmetric, larger and skewed to higher I_3 values. The skewness must be ascribed to the structural changes occurring on the crystal surface (see below).

3.6.2 Longitudinal monomer distribution: small caps

In order to analyze the crystal structure one defines the monomer distribution function $\rho(\mathbf{r})$ as

$$\rho(\mathbf{r}) = \frac{1}{N} \sum_{i=1}^{N} \left\langle \delta(\mathbf{r} - \mathbf{r}_i^{(\mathrm{cm})}) \right\rangle \tag{3.4}$$

where $\mathbf{r}_i^{(\mathrm{cm})}$ is the position of the i-th bead with respect to the center of mass of the chain and the brackets denote a suitable average. In particular, one defines the quantity

$$N_{||}(x^3) = N\, d \times \int \rho(x^1, x^2, x^3)\, dx^1 dx^2 \tag{3.5}$$

where $d \equiv r_0 \sin\left(\frac{\theta_0}{2}\right) \simeq 0.31$ is the distance along the chain backbone between two adjacent beads of the fully-extended chain and x^k is the projection of $\mathbf{r}$ along the $k-$th principal axis. The quantity $N_{||}(z)$ denotes the number of intersections of the chain with the plane at $x^3 = z$, namely a plan perpendicular to the approximate cylindrical symmetry x^3 axis. Fig. 3.14 plots the quantity $N_{||}(z)$ in the final crystalline state at $T = 9$ for all the thermal histories. It is apparent that the dependence of $N_{||}(z)$ on the thermal history is negligible. A fortiori, this holds true for the number of stems $\mu = N_{||}(0) = 10$, corresponding to the conformation yielding the global minimum of the free-energy (fig. 4.3). Three different regions are seen in Fig. 3.14:

- the central region, $|z| \lesssim L_\mathrm{c}/2$ with $L_\mathrm{c} = 8$, where $N_{||} \simeq 10$;
- the transition region, $L_\mathrm{c}/2 \lesssim |z| \lesssim L_\mathrm{c}/2 + 2$ where the average orientation of the stems departs from the one of the x^3 axis;
- the end region, $|z| \gtrsim L_\mathrm{c}/2 + 2$, where the stems join each other by forming loops.

Fig. 3.14 shows that the shape of $N_{||}(z)$ is very close to the ideal one corresponding to ten parallel, all-trans stems of fifty monomers each. The comparison makes it more apparent both the order in the final state and the small size of the two crystal caps. In fact, the longitudinal size of the loops, $\Delta z \sim 3$, is fairly smaller than the crystal length $2L_\mathrm{c} = 16$. Notice that, since $I_3 \ll I_\perp$ with $I_\perp = (I_1 + I_2)/2 \simeq 9990$, the folded chain may be sketched as a rigid rod with length $2L$, mass N and negligible thickness. The approximation yields $L = \sqrt{3I_\perp/N} \simeq 7.74$, to be compared with $L_\mathrm{c} \sim 8$, as drawn from Fig. 3.14.

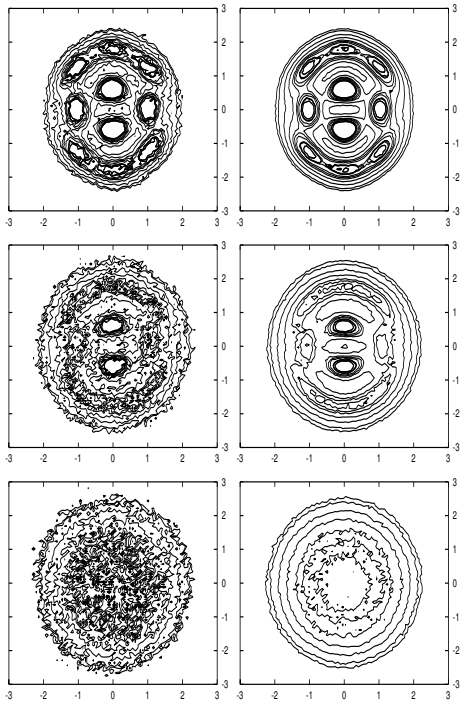

Figure 3.15: Tomography of the crystal final state. The transverse distributions $\rho_{\perp,\mathrm{centr}}$ (top), $\rho_{\perp,\mathrm{trans}}$ (center) and $\rho_{\perp,\mathrm{term}}$ (bottom) (Eqs. 3.6-3.8), for one particular thermal history, i.e. a direct quench from $T = 15$, (left panels) and averaged over all the thermal histories (right panels). Note: i) the independence of the tomography on the thermal history, ii) the absence of ordered structures on the crystal surface and the two caps.

Both previous experimental [188] and numerical [203] works pointed out the sharpness of the loops connecting the different stems and motivated a recent model of the FEL global minimum of the single-molecule polymer crystals [129] (see chapter 4 for a detailed description).

3.6.3 Transverse monomer distribution: surface mobility

In order to study the monomer distribution in planes perpendicular to the x_3 axis one defines

$$\rho_{\perp,\mathrm{centr}}(\mathbf{x}_\perp) = \int_{-L_c/2}^{L_c/2} \rho(\mathbf{x}_\perp, z)\, dz \tag{3.6}$$

$$\rho_{\perp,\mathrm{trans}}(\mathbf{x}_\perp) = \int_{L_c/2}^{L_c/2+2} [\rho(\mathbf{x}_\perp, z) + \rho(\mathbf{x}_\perp, -z)]\, dz \tag{3.7}$$

$$\rho_{\perp,\mathrm{term}}(\mathbf{x}_\perp) = \int_{L_c/2+2}^{\infty} [\rho(\mathbf{x}_\perp, z) + \rho(\mathbf{x}_\perp, -z)]\, dz \tag{3.8}$$

where $\mathbf{x}_\perp = x^1\mathbf{1} + x^2\mathbf{2}$ denotes the position vector in the transverse plane.

$\rho_{\perp,\mathrm{centr}}(\mathbf{x}_\perp)$, $\rho_{\perp,\mathrm{trans}}(\mathbf{x}_\perp)$ and $\rho_{\perp,\mathrm{term}}(\mathbf{x}_\perp)$ are the transverse monomer distributions in the central, transition and end regions, respectively. Fig. 3.15 shows the tomography of the crystal structure.

First, the crystal structure achieved after one particular thermal history (left panels) is compared with the average of all the investigated thermal histories (right panels). Data are collected during a lapse of time of about 5×10^3 time units. The absence of any significant difference is apparent and proves once again the absence of any memory effect, namely that at $T = 9$ the final crystalline state corresponds to the global minimum of the free-energy which is seen in Fig. 4.3 in chapter 4 (in the same chapter a deeper study of the FEL is given).

The tomography evidences several features of the crystal structure. The ten stems of the crystalline nucleus arrange themselves into an hexagonal structure (top plots). Noticeably, there is virtually no order on the crystal surface. Moving to the caps of the crystal structure the amount of order decreases. The transition region (center plots) still retains a partially ordered structure, visible in the two central stems, whereas the remaining eight external stems become more mobile. In the end regions (bottom plots), where the loops connecting the stems are located , any ordered structure is lost. It must be pointed out that the absence of order on the crystal surface and the two caps is due to the mobility of the chain in that regions, as it may be appreciated in the left plots of Fig. 3.15, which monitor the monomer transverse distribution for a single chain over a finite time interval. The presence of a disordered "corona" surrounding the ordered fraction of the nucleus has been noted by MonteCarlo simulations [206]. In the present case the direct inspection of several snapshots shows that the crystal surface is highly mobile and includes the chain ends which are excluded from the crystal interior. The confinement of the end groups on the surface avoids the impairment of lattice perfection and agrees with previous experimental findings [188].

The results discussed in the present section allow one to conclude that in the final crystalline state at $T = 9$ the chain packs into ten stems, of approximately

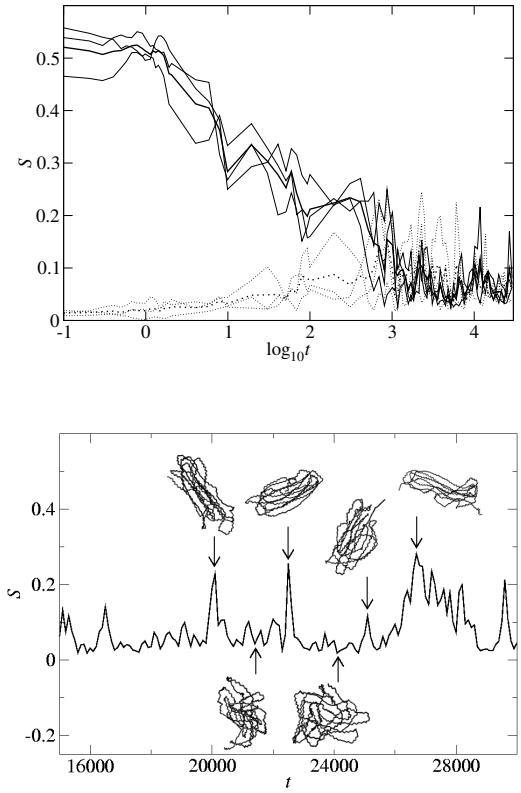

Figure 3.16: Top: time evolution of the order parameter S for different thermal histories ending at $T = 11$ (top); the dotted lines refer to quenches from $T = 15$, the solid lines to reheating from the crystalline final state at $T = 9$. The thick lines represent the average of the corresponding group of curves. Bottom: Fluctuations of the order parameter for one selected thermal history at long times. For some selected S values the corresponding chain conformations are shown.

equal length, arranged into a regular pattern with hexagonal symmetry. The ordered structure cannot include all the beads because of the chain connectivity and of the local potentials, which e.g. generically do not allow a regular packing of chain bendings. The disorder is expelled into the two caps and on the surface, where the structural fluctuations take place. Remarkably, the end regions where the loops connecting the stems are located have small size (see figs. 3.11 and 3.14).

3.7 Melting

The equilibrium melting temperature $T_m^{(eq)}$ is, by definition [205], the temperature where the free-energies of the ordered and the disordered states are equal. An estimate is given by melting the crystal in the limit of vanishing heating rates. By following that method the single-molecule crystal was found to melt at $T_m =$

11 ± 0.2 for the force-field in use [122, 123].

$T = 11$ was reached by:

- instantaneously quenching three equilibrated configurations at $T = 15$
- instantaneously heating three configurations of the crystalline final state at $T = 9$.

Fig. 3.16 shows the subsequent temporal changes of the order parameter S. After the sudden heating, the melting of the crystal is signaled by the large drop in the order parameter S and exhibits large fluctuations at long times. Similar fluctuations are also observed for the quenched configurations. The inspection of several snapshots suggests that the long-time behaviour at $T = 11$ is independent of the thermal history. Fig. 3.16 shows the fluctuations of the order parameter for one selected thermal history at long times and the corresponding chain conformations. It is seen that the large fluctuations are due to infrequent attempts to crystallize of the chain. This behaviour, leading to large energy fluctuations (not shown), is a consequence of the proximity of $T_m^{(eq)}$ to $T = 11$ [204, 205]. The FEL (see chapter 4) at $T = 11$ shows that thermal fluctuations of about $3k_BT$ are needed for ordering the structure, i.e. for increasing I_1 from about $5 \cdot 10^3$ to about 10^4. To characterize the process, the waiting-time distribution $\psi(t)$ between two successive crystallization attempts was evaluated. An attempt is defined as an event with *average* order parameter $\bar{S} > S_{\text{threshold}} = 0.12$ over 50 time units. The waiting-time distribution is found to be roughly exponential (Fig. 3.17), suggesting that the attempts are independent events.

The results discussed in this section provide upper limits for the degree of superheating/supercooling of the present PE model. One defines $\varepsilon = (T_m^* - T_f^*)/T_f^* \geq 0$, T_m^* and T_f^* being the melting temperature on heating and the freezing temperature on cooling, respectively. Being $10 < T_m^*, T_f^* < 11$, it is found $\varepsilon < 0.1$. i.e. small hysteresis.

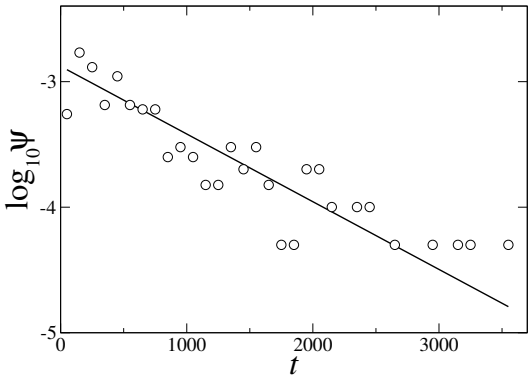

Figure 3.17: Waiting-time distribution of the crystallization attempts at $T = 11$ (see text for details). The solid line is a fit with an exponential decay with time constant $\tau = 805 \pm 5$.

The melting of crystalline polymers has been recently studied by MonteCarlo simulations [204, 205, 207]. In particular, the superheating of the single crystals, as well as the supercooling of the disordered state, have been noted for single chains with a number of monomers $N \gtrsim 100$ resulting in large hysteresis and dependence on the thermal history [204, 205]. To proceed with a comparison with the present results some remarks must be done. The MonteCarlo simulations sketch the polymer as a fully flexible linear chain of N rigid segments [204, 205]. It is natural to identify that segments with the Kuhn segments. As noted in Sec.3.3) the number of Kuhn segment of the present PE model is about $N_{\rm k} = 125$. For $N \cong 125$ the results of refs. [204, 205] yield $\varepsilon \cong 0.1$ in good agreement with the present ones.

Chapter 4

Free Energy Landscape

In this chapter the results presented in the previous chapter will be interpreted by means of the key concept of the Free Energy Landscape. Before entering the description of our findings a brief introduction of the various "energy landscapes" will be briefly given. In literature appeared nice reviews which can introduce the workers in different disciplines to this instruments, such as [208, 209].A very comprehensive book is the one written by Wales [210].

4.1 Energy landscapes

The term "energy landscape" was probably first introduced in the context of free energy surfaces [211–221]. The potential energy landscape (PEL) represents the potential energy of a given system as a function of all the relevant atomic or molecular coordinates. In general the PEL is a high-dimensional function compared to a free energy landscape (FEL), which is obtained from the PEL by averaging over all the other degrees of freedom for fixed values of the order parameters [222]. This averaging is repeated to provide an interpolation over the range for which the order parameters have physically interesting values. The PEL is perhaps a more fundamental object, since there is no requirement for a subjective choice of order parameters. FEL are also temperature dependent, whereas the PEL is not.

A minimum on either a FEL or a PEL is a point from which a small displacement in any direction increases the energy; a displacement corresponds to changes in atomic coordinates for the PEL and in order parameters for the FEL.

Equilibrium thermodynamic properties only depend on the relative potential energies of the local minima in the PEL, and the volumes of configuration space associated with them, whereas the relaxation dynamic is related to the pathways between minima, the so-called *connectivity*. Understanding how some system can relax to particular structures requires a global view of the landscape. Even knowledge of the distribution of barrier heights that separate the local minima is not generally sufficient to understand the global dynamics, unless we also know which minima the barriers actually separate. In term of FEL, local minima represents likely kinetics traps.

Pictorially, the trajectory of the system can be represented as a motion of a representative point $\vec{r}^N$ in the 3N space on the $V(\vec{r}^N)$ surface (see figures 4.1).

It is important to stress that the PEL does not depend on T. It is also important to realize that the exploration of the PEL (i.e. which parts of the surface are explored) is strongly T dependent. As the surface is in 3N-dimensional space, the characterization of the surface can only be performed on a statistical basis, and one of the aims of the PEL studies is indeed to estimate the number of local minima and their distribution in energy, and to estimate the shape of the surface around the local minimum and the hypervolume in configuration space associated with each of these minima. The number and energy depth of the local minima are indeed the basic ingredients of the PEL thermodynamic formalism, put on a firm basis by the work of Stillinger and Weber [223–225]

Stillinger and Weber provided a formally exact partitioning of the configurational space as a sum of distinct basins, associating with each local minimum of the potential energy surface (named an inherent structure, IS) all points in configuration space connected to the minimum by a steepest descent path. This set of points is named a *basin*. The definition of a basin proposed by Stillinger and

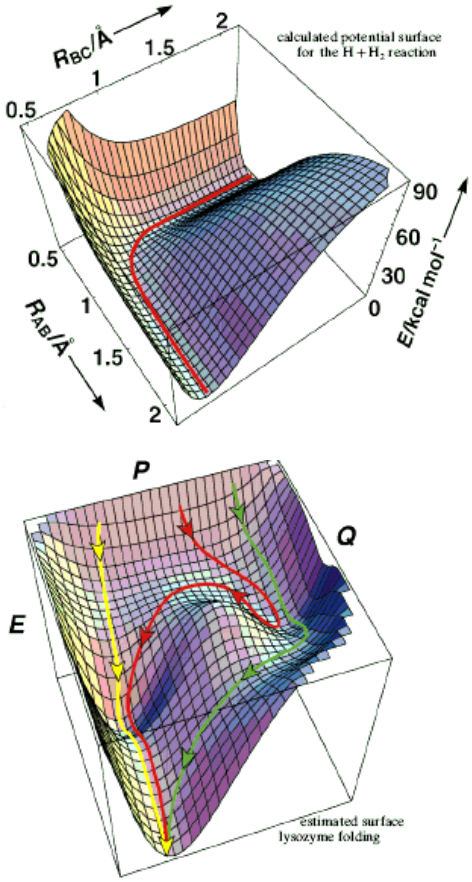

Figure 4.1: Examples of PEL. (top) The collinear hydrogen exchange reaction $H_A + H_B - H_C \rightarrow H_A - H_B + H_C$. In this case the PEL is function only of the two internuclear distances R_{AB} and R_{BC} (in Å). (bottom) A more complex example is the case of lysozyme where the picture has been constructed by averaging over all the solvent and protein coordinated except for the native contacts present (Q) and the compactness (P). For the exact definition of the last two quantities we address the reader attention to the paper where they come from. E is the free-energy, so the surface is a free energy surface. Worth of noticing is the fact that more than one trajectory are available in order to arrive in the global minimum [219].

Weber provides the essential ingredient for developing a thermodynamic formalism since — except for a set of points of zero measure (the saddles and the ridges between different basins) — all points in configuration space are associated with a local minimum. The Stillinger and Weber definition also provides an algorithm suited for numerical studies of the landscape properties.

the FEL has established significance in the field of proteins folding. In 1969 Levinthal first pointed out that the reversible refolding observed for some globular proteins should be viewed as a remarkable achievement, since the observed folding times were entirely incompatible with a random search of all the minima in the PEL (the so-called *Levinthal's paradox* [226]). It is generally recognized that the flaw in Levinthal's original analysis is to regard the search through con-

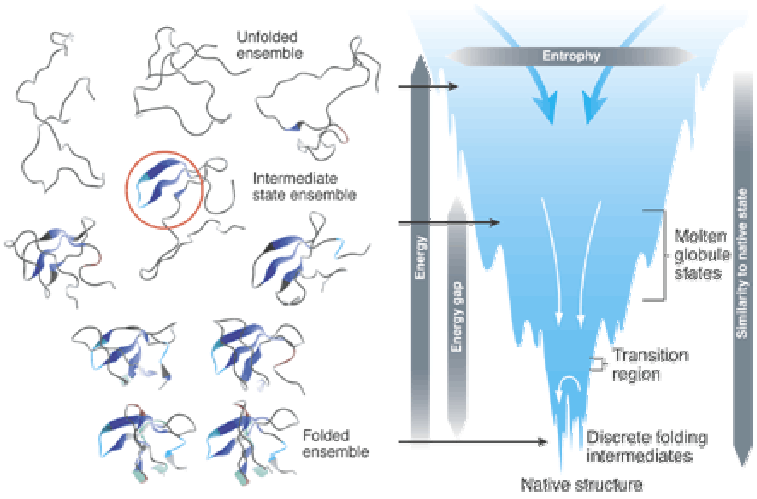

Figure 4.2: An example of a folding funnel. Schematic representation of the changes in internal entropy and potential energy on folding, and the correspondence between these thermodynamic parameters and the ensembles of configurations to which they correspond. [222].

formational space as random, which corresponds to a flat potential or free energy surface. However, the introduction of an energy bias toward the native state has a profound effect on the kinetics, and can reduce the relaxation time scale to a realistic value in simple models [227–229]. It is worth noticing that natural proteins can fold to a well defined native state (which is the minimum energy level [214]), whereas artificial proteins are not expected to do this [211, 230–234].

The presence of a well-defined FEL minimum for the native state is not in itself sufficient for a protein to fold efficiently, since the minimum must also be kinetically accessible [211, 227, 235–238]. It has been proposed that the native state of a natural protein may correspond to the terminus of a collection of convergent kinetic pathways, and envisaged a “folding funnel” (fig. 4.2) where the free energy decreases systematically in the vicinity of the target structure [215]. Efficient folding also requires the absence of local free energy minima that would act as kinetic traps and prevent relaxation to the native state [227]. The funnel concept has been developed in a number of further studies [214, 216, 217, 220, 239–246].

FEL and PEL play an important role also in other field [210, 247], such as glasses and supercooled liquids [248–257], clusters [258], aging phenomena [208, 259], ions transport [260], metals [261], chemical reactions [262].

4.2 Free-energy landscape of a single molecule

In our studies on the polymer crystallization, we try to understand the behaviour of a single molecule crystal from a dilute solution. In order to grasp a deep view of this phase transition we decide to move toward the analysis of the FEL [123, 124, 204, 205, 207, 263].

In order to characterize the reorganization of the chain, both the free energy F and the potential energy U are sampled and their average over all the available configurations correlated to the order parameter I_1 . In order to evaluate the Landau free energy $F(X) = -k_B T \ln Z(T, X)$ of a macroscopic state being characterized by the order parameter X at temperature T leading to a partition function $Z(T, X)$, one relates the latter to the probability $P(X)$ to find the observable with value X via [264]

$$P(T, X) = Z(T, X)/Z(T) \tag{4.1}$$

and $Z(T)$ is the partition function. Then, up to an additive constant $c(T)$ depending on the temperature $F(X)$ is given by [128, 204, 205]

$$F(X) = -k_B T \ln P(T, X) + c(T) \tag{4.2}$$

Since only the shape of $F(X)$ is of interest here, the constant $c(T)$ will be neglected henceforth.

In the present case the choice $X = I_1$ is made in agreement with others [123, 124]. In fact, the crystalline structures are rod-like with foldings having, approximately, equal length [130]. Consequently, the metastable states are well identified by the length of their stems m and then by I_1, the latter being roughly proportional to m^2. Efficient Monte Carlo simulations may be also used to evaluate

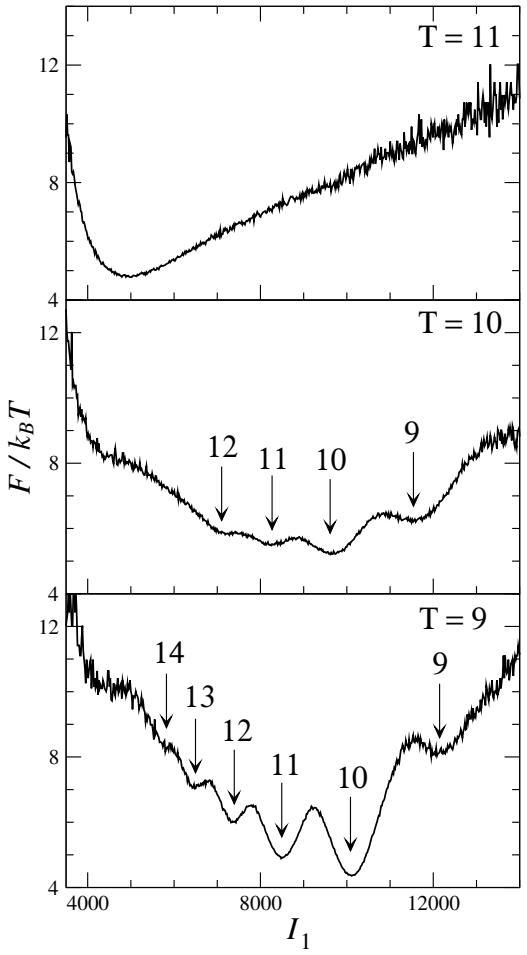

Figure 4.3: The free-energy landscape (FEL) at $T = 9, 10, 11$ as a function of the largest moment of inertia of the chain I_1. The labels indicate the number of stems μ of the ordered structures corresponding to the minima.

the free energy. However, MD techniques, which were already extensively used to investigate the crystallization dynamics of the present system [129, 130, 265, 266], proved to be accurate enough to the present purposes.

4.2.1 Free energy landscape when changing temperature

Fig. 4.3 shows the free-energy landscape (FEL) at $T = 9, 10, 11$ as a function of the largest moment of inertia of the chain I_1. At $T = 11$ a single minimum is observed at $I_1 = I_1^* \sim 4900$. On decreasing the temperature and entering the supercooled regime at $T = 10$ the minimum at I_1^* disappears and a series of shallow minima is observed at higher I_1 values ($I_1 \gtrsim 5500$) . They correspond

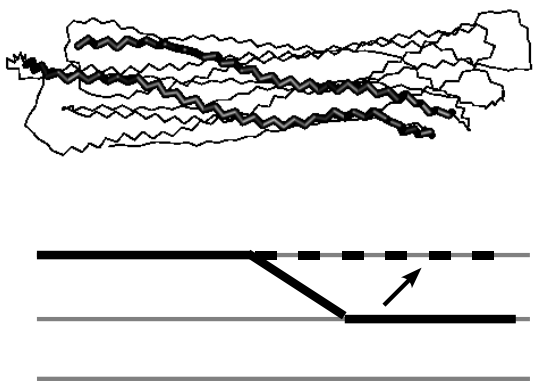

Figure 4.4: Snake-like displacement of two stems (bold) sliding on the crystal surface. The cartoon below the wire-frame view sketches the next move of the two stems to get the optimal alignment with the ordered substrate of the inner stems (grey lines). The black dashed line is the new position of the displaced portion of the stems after the move [266].

to the formation of metastable crystal structures with different number of stems μ (see Sec. 4.2.3). The direct inspection of the dynamical behaviour of the chain at $T = 10$ shows that a continuous interconversion between the metastable structures occurs with no well-defined single final state. At $T = 9$ the FEL exhibits a richer structure with several minima. A well-defined global minimum is apparent corresponding to the final state with $\mu = 10$ (see Sec. 3.6). It is also seen that lowering the temperature allows the appearance of new metastable ordered states which, as at $T = 10$, may be labeled by the number of stems. The comparison with the FEL of shorter chains at $T = 9$ [123, 124] shows that the number of metastable states increases with the chain length. The presence of metastable and long-lived crystalline forms is supported by a number of experimental facts, e.g. the observation of the transient phases that convert to more stable forms during the folding process [180] and the demonstration of stable folded structures for long alkanes, $N \gtrsim 150$, [11, 28, 188, 190].

4.2.2 Crystal structure

The structural changes of the crystalline structures are twofold:

- changes due to the increase or decrease of the number of stems [130](for example, figure 3.12);

- changes which leave the number of stems unaltered [130, 266](see figures 4.4 and 4.5).

The former are effectively characterized by the moment of inertia I_1 and are activated. The latter do not lead to either appreciable changes of I_1 or the internal energy.

Examples of such processes are provided by the reorganizations taking place on the crystal surface, e.g. two stems are seen to slide on the crystal surface while preserving their alignment with the ordered substrate (figure 4.4) . Another kind of restructuring with no change of the number of stems is the position exchange between aligned stems, e.g. the expulsion of a stem terminated by one chain-end from the inside of the crystal (figure 4.5). Notice that the above kinds of rearrangements leave the potential energy largely unaffected, i.e. they are entropic processes, with negligible changes of the moments of inertia.

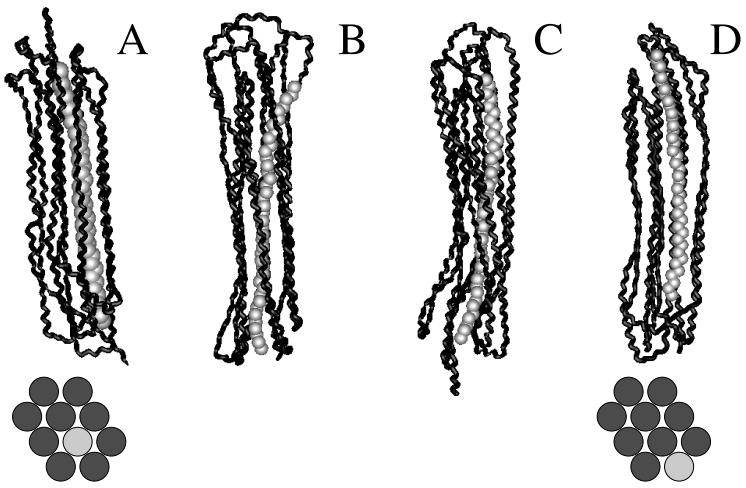

Figure 4.5: The expulsion of one stem terminated by a chain-end (united-atoms) by the inside of the crystal. The snapshots are taken at times (in reduced units): $t_A = 26240, t_B = 26260, t_C = 26270, t_D = 26280$. The two cartoons below the snapshots are schematic cross-sections of the ordered middle portion of the crystal at tA and tD. The circles denote the stems. The light-colored circle is the stem terminated by the chain-end [266].

It is worthwhile to appreciate the role of the mobile fraction of monomers of the crystalline final structure at $T = 9$. In thermodynamic equilibrium, fixed-volume systems minimize the Helmholtz free-energy. Correspondingly, the state point moves between several potential-energy minima (the mechanical equilibrium states) in a region of PEL determined by the temperature. When the temperature decreases, the state point spends more time in the deeper, rarer minima of PEL. If crystallization occurs, the state point becomes localized in the global minimum of PEL. The global minimum is usually not degenerate and the shape of the corresponding minimum of F stems from vibrational dynamics providing suitable contributions to both the internal energy and the entropy. In the present case the region of PEL where the state point localizes at $T = 9$ is highly degenerate due to the different surface configurations of the crystallized chain. Thus, the configurational contributions to F are not negligible even in the crystalline state.

The FEL (fig. 4.3) shows that $10 < T_m^{(eq)} < 11$ since the ordered states ($I_1 \gtrsim 5500$) have higher (lower) F values at $T = 11$ ($T = 10$) than the disordered one ($I_1 \sim 5000$). Noticeably, at $T = 10$ the crystal is not stable but it undergoes frequent interconversions between different ordered structures as signaled by the shallow minima of the FEL and visual inspection of the snapshots (data not shown).

Both the single minimum of F corresponding to the disordered state at $T = 11$ and the small barrier heights at $T = 10$ suggest the negligible superheating of the crystal.

4.2.3 The crystalline metastable states

Fig. 3.9 presents some representative snapshots showing that the chain, after the quench at $T = 9$, undergoes large conformation changes in order to reach the crystalline final state. The FEL structure at $T = 9$, Fig. 4.3, elucidates the

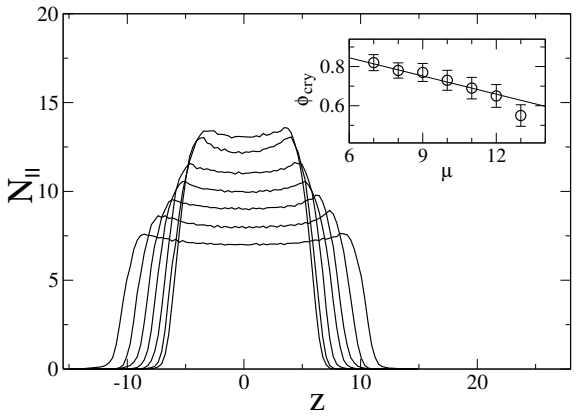

μ	m	m^*
7	14.0	14.43
8	12.2	12.12
9	10.25	10.33
10	8.75	8.9
11	7.5	7.73
12	6.25	6.75
13	5.0	5.92

Figure 4.6: The number of intersections of the chain with the plane at $x^3 = z$, $N_{||}(z)$, for the different metastable crystalline states at $T = 9$ evidenced by the minima of FEL (Fig. 4.3). The number of stems $\mu = N_{||}(0)$ is in the range $7 < \mu < 13$. The crystal with $\mu = 10$ stems corresponds to the final equilibrated state. Inset: The crystalline fraction ϕ_{cry} (eq.4.3) vs. the number of stems μ. The superimposed line is eq.4.4 with $\lambda = 4.0 \pm 0.1$. In the table is presented Eq.4.5 with $\lambda = 4$

state evolution starting at some point characterized by a certain I_1 value, going through a number of transient ordered phases with well-defined number of stems, and ending in the global minimum. n- alkanes are known to have intermediate metastable forms on the path to the final crystalline state [180].

For the different metastable crystalline states at $T = 9$, evidenced by the minima of FEL (Fig. 4.3), Fig. 4.6 shows the number of intersections of the chain $N_{||}(z)$ with the plane at $x^3 = z$, perpendicular to the approximate cylindrical symmetry x^3 axis. The flatness of $N_{||}(z)$ shows that the central sections of the metastable structure are well ordered. It is also apparent that the monomer distribution in the end sections does not depend in a marked way on the number of stems $\mu = N_{||}(0)$. To be more quantitative, we consider the crystalline fraction ϕ_{cry} of a crystal with μ stems. ϕ_{cry} is estimated by the ratio

$$\phi_{cry} = \frac{\int_{z^1_{max}}^{z^2_{max}} N_{||}(z)dz}{\int_{-\infty}^{\infty} N_{||}(z)dz} \tag{4.3}$$

where z^1_{max} and z^2_{max} are the points where $N_{||}(z)$ reaches the maximum values, see Fig. 4.6. Obviously, the amount of crystalline order in a single-molecule crystal may be defined in alternative ways, e.g. in terms of bunches of orientationally ordered trans segments, "trans domains" [125]. However, we found that the definition eq.4.3 is quite fruitful to our purposes. In fact, let us assume that an average number of Kuhn segments λ is located in each of the $\mu - 1$ loops connecting the stems. Then, the crystalline fraction is given by

$$\phi_{cry} = 1 - (\mu - 1)\frac{\lambda}{N_k}. \tag{4.4}$$

The inset of Fig. 4.6 shows the best-fit of ϕ_{cry} from eq.4.3 with eq.4.4 having adjusted λ. It proves that the number of monomers forming the loops do not change appreciably from one transient structure to the other. At the highest number of stems (shortest crystal longitudinal size) eq.4.4 overestimates ϕ_{cry} suggesting that the disorder of the end sections affects the ordered part more effectively (or, alternatively, that λ increases).

As further test of the negligible changes of λ with μ we note that the number of Kuhn segments per stem m is expressed as $m = (z^2_{max} - z^1_{max})/\ell_{\rm k}$. On the other hand, if λ is nearly constant

$$m^* = \frac{N_k - \lambda\,(\mu - 1)}{\mu} \tag{4.5}$$

Table in Fig. 4.6 compares m with m^* as taken from Eq.4.5 with $\lambda = 4$.

4.2.4 Energy contributions to FEL

Figure 4.8 plots the free-energy landscape (FEL) at $T = 9$, the overall potential energy and its torsional and LJ contributions as functions of the largest moment

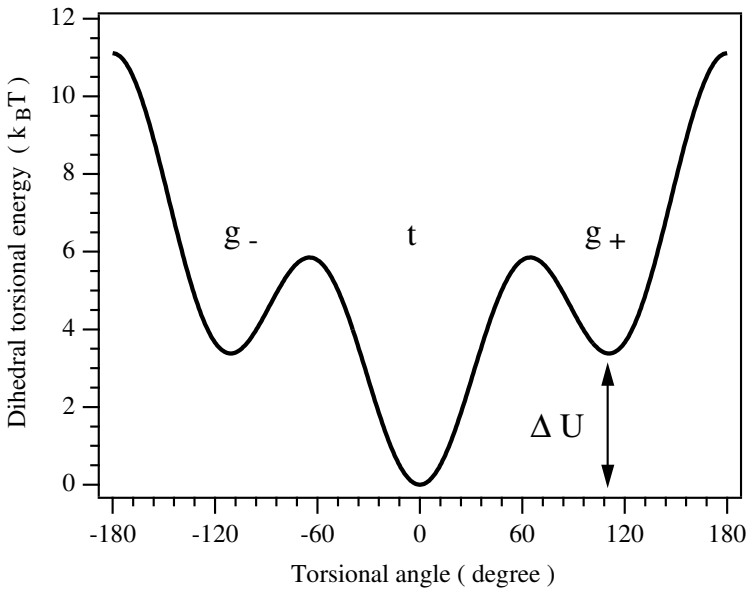

Figure 4.7: The dihedral torsional energy as function of the dihedral torsional angle in units of k_BT with $T = 9$ in reduced units. ΔU is the energy change in a $g_\pm \leftrightarrow t$ transition [267].

of inertia of the chain I_1. For a given I_1 value the above quantities are the averages over all the configurations with equal I_1 assumed by the crystal during the time evolution. Since bond angles and length exhibit negligible changes, the related energies are not considered. The range of I_1 values and the FEL statistics in Fig.4.8 is much improved with respect to previous reports [130, 266], thus allowing for a more detailed view of the metastable structures. Several minima of the free energy, corresponding to well-defined metastable crystals with different number of stems, are seen. The global minimum corresponds to the equilibrated lamella with ten stems. Figure 4.8 shows that the free-energy exhibits minima close to the potential energy ones.

First, we focus on the potential energy with contributions from both the torsional and the LJ potentials. The *decrease* of the torsional energy by increasing I_1, i.e. by decreasing the number of stems, which is seen in Fig. 4.8 is due to the conversion of $g_\pm$ torsional states into t states (see fig.4.7) leading to longer

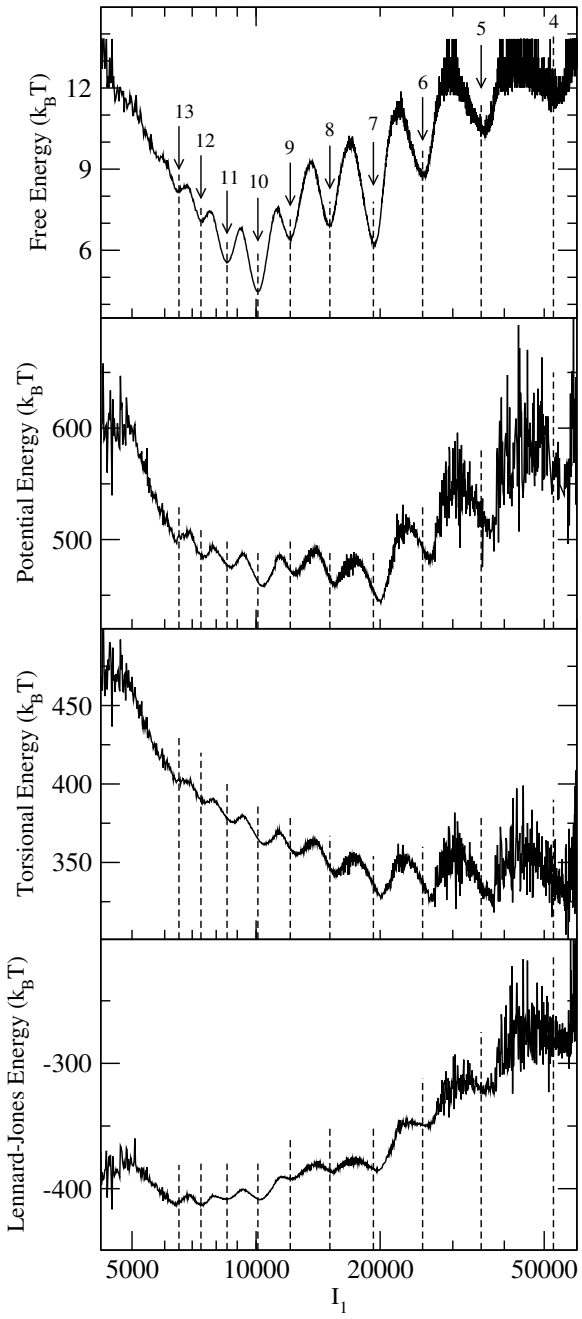

Figure 4.8: From the top to the bottom: the free-energy landscape (FEL) at $T = 9$, the overall potential energy and its torsional and Lennard-Jones contributions as function of the largest moment of inertia of the chain I_1. The labels indicate the number of stems μ of the metastable crystals corresponding to the free-energy minima [267].

stems. On the other hand, increasing I_1 leads to more prolate crystals where the attractive tail of the LJ potential becomes more important. This explains the *increase* of the LJ energy by increasing I_1 which is seen in Fig. 4.8. The different I_1 dependencies of the torsional and LJ potential energies set the overall curvature of the total potential energy. Fig. 4.8 also shows that the latter has the global minimum when the crystal has seven stems. This differs from the FEL global minimum being found for crystals with ten stems. The effect is due to entropic effects shaping the gross features of the FEL. It was shown in chapter 5 that the combinatorics of the stems and of the loops provides a convenient model.

Chapter 5

Nucleation and growth

This chapter is devoted to the study of the primary nucleation, and the immediately following growth, of single crystals in dilute solution. Before starting we report a brief review on the classical theory of nucleation and growth in macromolecular systems; after that we present the new ideas we introduced in order to explain the equilibrium conformation of single molecule polymer crystals [129]; worth of noticing is that the considerations we proposed in that paper, were subsequently reproposed in a number of papers [268, 269].

5.1 Classical nucleation and growth

As said in the previous chapters, the crystalline state of polymers is very different from that of other materials because of the need to arrange in an ordered way a large number of monomers linked to each other sequentially. This results in a wide range of possible hierarchical morphologies where the basic unit is the lamella, which is a few hundred Ångstrom thick [11, 28, 41, 48, 52, 270]. The backbone of a single polymer chain, which is several thousand Ångstrom long, is folded inside the lamella to form the socalled stems; these are perpendicular to the basal surfaces of the lamella where the foldings are localized [28, 48, 52].

The polymer crystal is assumed to have transverse isotropy, its shape repre-

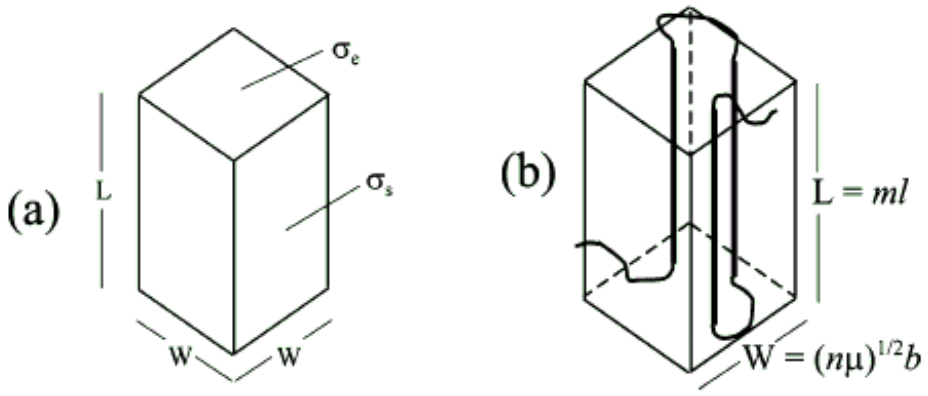

Figure 5.1: Schematic representation of a homogeneous nucleus of a macromolecule: a) dimension and surface energies; b) illustration of a chain inside the crystal [268].

sented by a square tablet or column of width W and thickness L as in Figure 5.1.

The total free energy of this crystal with respect to the disordered melt or solution state is:

$$F = -W^2 L\epsilon + 4WL\sigma_s + 2W^2\sigma_e \tag{5.1}$$

Here ϵ is the bulk free energy of melting (or dissolution) per unit volume, σ_s is the lateral surface free energy and σ_e is the basal surface free energy. See also fig. 5.1. We can see that the total free energy is a combination of an always favourable term, the bulk free energy, and an antagonistic term, the surface free energies. This means, that in order be stable, the nucleus has to achieve a minimum dimension which guarantees the dominant role of the bulk component. In particular, at the beginning, the surface free energy is dominant, and the crystal unstable; if the nucleus is not able to growth enough in order to overcame the free energy barrier, it disappears. For the competition between the surface and bulk free energy, see fig. 1.8, which deals with a spherical distribution of matter.

The maximum of the free energy can be localized by means of partial differentiation of F with respect to L and W:

$$L_c = \frac{4\sigma_e}{\epsilon}; \qquad W_c = \frac{4\sigma_s}{\epsilon} \tag{5.2}$$

where L_c and W_c are the critical dimensions of the nucleus. For a sample of a dimension $V = W^2L$ the values which minimize the free energy are:

$$L^* = \left(\frac{\sigma_e}{\sigma_s}\right)^{2/3} V^{1/3}; \qquad W^* = \left(\frac{\sigma_s}{\sigma_e}\right)^{1/3} V^{1/3} \tag{5.3}$$

The derivation is trivial: for example, to obtain L^* is sufficient to substitute $W = \sqrt{(V/L)}$ in eq. 5.1; putting $(\partial F/\partial L) = 0$ in the same equation, L^* follows.

Crystal volume V and equilibrium dimensions L^* and W^* increase in tandem by accretion of monomers from either the nucleating chain or from other chains. The minimum-energy aspect ratio is independent of crystal size and is the same for both the critical nucleus and a stable crystal of arbitrary volume:

$$\frac{L^*}{W^*} = \frac{L_c}{W_c} = \frac{\sigma_e}{\sigma_s} \tag{5.4}$$

This equation can be recognized as an example of Wulff's law [271, 272] for equilibrium crystal shapes. It should be noted that the same surface energies are used for critical nuclei and for mature crystals, a common simplifying assumption that may not be correct in all cases.

Although the free energy of the supercritical nucleus decreases during growth, it remains higher than that of the melt until the stability dimensions L_{st} and W_{st} are achieved for which $F = 0$ in eq. 5.1:

$$L_{st} = \frac{6\sigma_e}{\epsilon}; \qquad W_{st} = \frac{6\sigma_s}{\epsilon} \tag{5.5}$$

To obtains this rules is sufficient to substituting W or L in eq. 5.1 using eq. 5.4; when $F = 0$ the result follows.

Summarizing: the crystal evolution is driven by the action of both bulk and surface effects (eq. 5.1). In the first stage of his formation, the nucleus is characterized by an increasing $F > 0$, until its dimension reached some critical values L_c and W_c (eq. 5.2). If the nucleus is not able to reach this values, it dissolves. After

overcoming the free-energy barrier, a further increasing in its volume (eq. 5.3), means a decreasing in total free energy (again $F > 0$). The total free-energy is positive until eq. 5.5 is fulfilled. Further increasing means $F < 0$, i.e. the nucleus becomes stable and a new crystal starts to spread.

5.2 Analytic model of FEL global minimum

The equilibrium dynamic presented until now is obtained without any consideration on the polymeric nature of the sample: the only important parameters are the geometrical properties of the macromolecular crystal. In what follows we are interested in desvealing the polymeric nature of the crystal. In particular the attention is addressed to understand the behaviour of a single polymer chain crystal, grown from a dilute solution. Comparison is made with our molecular dynamic simulations (see Chapters 2,3,4 for further details.) The model described below appeared in ref. [129].

The experimental evidence suggests that long alkanes fold in integral reciprocals of the extended chain length. In particular, this implies that large portions of the chain are mostly contributing to the straight stems, i.e. the size of the loops connecting different stems is short [188]. In our simulations, this is apparent from selected configurations (figure 3.11) as well as from the analysis of the longitudinal monomer distribution (figure 3.15). The average length of the loops ℓ_{loop} is relatively small and involves a short sequence of Kuhn segments, $\ell_{loop}/\ell_k \sim 4$ [130, 265]. Based on these remarks, a very simple model which incorporates the above feature and accounts for the existence of equilibrium folded structures has been developed.

A crystallized chain of N_k Kuhn segments is pictured as formed by a nucleus with μ stems, $\mu - 1$ loops and the two cilia. When a segment is included in one stem of the nucleus the energy gain is $\epsilon > 0$ in units of $k_B T$. The lateral surface free-energy contribution per unit area is σ' in units of $k_B T$. If m denotes the

average number of segments per stem, the overall free energy $F_{m,\mu}$ of the nucleus is written as

$$\frac{F_{m,\mu}}{k_B T} = -\mu m\epsilon + \sigma\sqrt{\mu}m - \ln W_{m,\mu} \tag{5.6}$$

with $\sigma = \alpha\sigma' r_0^2$, α being a numerical factor. $W_{m,\mu}$ denotes the number of distinct ways to arrange the N_k segments in μ stems, each of m segments, $\mu - 1$ loops and two tails. To evaluate $W_{m,\mu}$ one assumes that each loop has only one conformation. This roughly accounts for the both the expected stiffness of the short loops and their mutual steric constraints. We factorize $W_{m,\mu}$ as

$$W_{m,\mu} = \binom{N_k - \mu m + \mu}{\mu} \times p^{\mu-1} \tag{5.7}$$

The binomial coefficient enumerates the distinct ways to get a one-dimensional arrangement of $(N_k - \mu m)$ segments separated by μ walls. The second term is a weighting factor accounting for the entropic limitations to bend the linear arrangement and form a crystalline nucleus with $\mu - 1$ loops. One expects that conformations with a large number of loops are inhibited by jams occurring in the compact caps of the nucleus (see figure 3.11). Owing to the roughness of the present model p is left as an adjustable parameter. Equation 5.7 sets the entropic contribution $\ln W_{m,\mu}$ to the free energy. Small variants, e.g. by neglecting the two cilia, do not improve the model appreciably. Muthukumar proved that the entropy role is crucial to enforce the minimum of $F_{m,\mu}$ and estimated $W_{m,\mu}$ by resorting to a Gaussian model of the loops and to a field-theoretic approach [123]. Although the Gaussian model is expected to work nicely for long loops, it may overestimate $W_{m,\mu}$ in the case of short loops. The present model cuts the entropy due to the loop conformations, i.e. the so called entropy of disorientation, and limits the entropy to the mixing of the μ stems of the crystalline nucleus (with m segments each) along the polymer chain. The resulting free energy has one adjustable parameter less than that of [123]. Representative plots of the free-energy landscape (FEL) and the contour plot of the minimum are shown in figures 5.2 and 5.3, respectively. Qualitatively similar plots were also presented

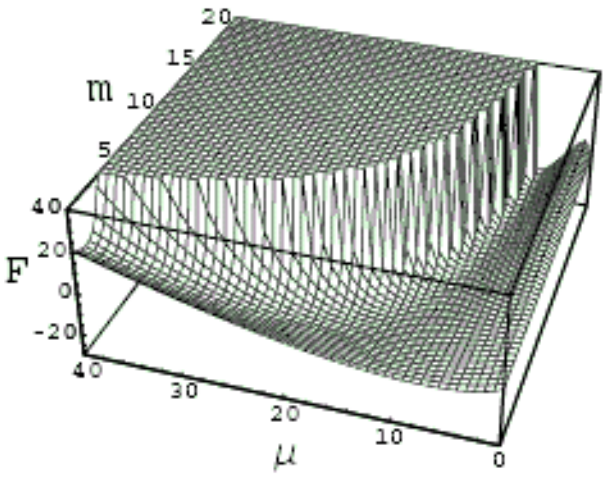

Figure 5.2: The free energy landscape (FEL) of the model. m is the number of Kuhn segments belonging to one of the μ stems. $N_k = 125, \epsilon = 0.6, \sigma = 0.97, p = 0.06$ [129].

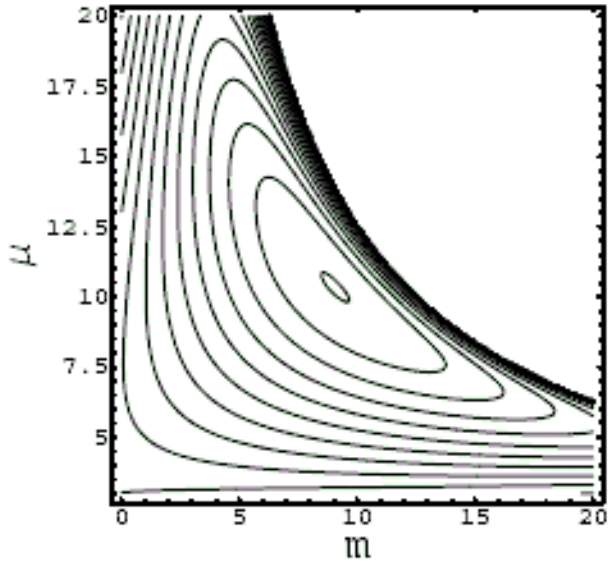

Figure 5.3: Contour plot of the FEL of figure 5.2. The minimum is located at $m^* = 9.68, \mu^* = 9.94$ [129].

in [123]. The FEL is limited to the region $\mu m < N_k$ where segments are available to form both the loops and the two cilia. At $\mu m \lesssim N_k$ a steep ridge is found, due to the small entropy of conformations with very short loops/cilia. Figure 5.3 shows the contour plots of the FEL of figure 5.2. The minimum is located at $m^* = 9.68, \mu^* = 9.94$. This must be compared with $\mu = 10$ from the MD results. If L_{stem} is the stem length, the average number of Kuhn segments per stem is $m = L_{stem}/\ell_k$. From figure 3.14 one estimates $L_{stem} = 2z^*$, where z^* is the positive non-trivial solution of the equation $N_{\|}(z) = 10$, i.e. the intercept with $z \neq 0$ between the distribution $N_{\|}(z) = 10$ from the simulation and that from the ideal case of ten fully stretched stems. One finds $m = 10$ with $L_{stem} = 12$ to be compared with $m^* = 9.68$ of the model. Finally, one notes that the coordinates of the FEL minimum correspond to an average number of segments located in each loop equal to $(N_k - \mu^* m^+ *)/(\mu^* - 1) = 3.22$. The value is consistent with the basic assumption of the model, i.e. short loops, and compares well with the value from the MD simulations, about 3-4 4.2.3.

Figure 5.4 is a parametric plot of the number of stems $\mu^*(\epsilon, \sigma)$ and the segments per stem $m^*(\epsilon, \sigma)$ of the FEL minimum with p=0.06 for different ϵ and *sigma* values. On increasing the surface tension σ, the minimum moves from very prolate crystals (few and very long stems) to more spherical crystals (more and shorter stems) to minimize the exposed surface by keeping the total volume constant (N_k constant). The presence of a maximum number of stems for a given ϵ must be considered with caution, in that it corresponds to a very small number of segments per stem and a very large number of segments located in the loops, therefore pushing the model to its limits.

The existence of a minimum of $F_{m,\mu}$ relies on the limitations of having conformations with a large number of loops. This is understood by noting the relation $F_{m,\mu} = F_{m_\mu}(p = 0) - (\mu - 1) \ln p(p < 1)$ which makes explicit the entropic penalty for conformations with a large number of stems μ. In fact, if the entropy is removed by setting $p = 1$, $F_{m,\mu}$ with the same parameters as figure 5.2 has no minimum

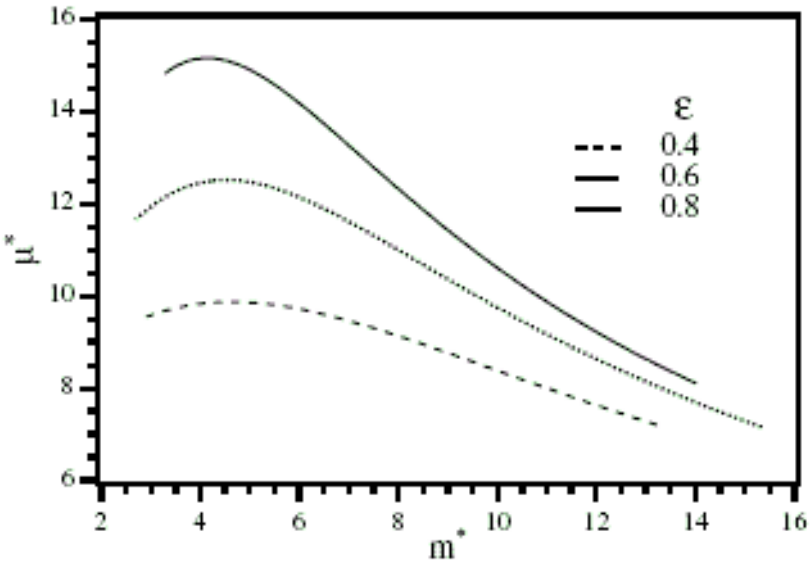

Figure 5.4: Plot of the coordinates μ^*, m^* of the FEL minimum with $N_k = 125, p = 0.06$ for different ϵ and σ values. For $\epsilon = 0.4, 0.6$ and 0.8, σ is in the interval $0.5 \leqslant \sigma \leqslant 0.95$,$0.6 \leqslant \sigma \leqslant 1.655$ and $0.8 \leqslant \sigma \leqslant 2.4$, respectively. m^* always decrease on increasing σ [129].

(data not shown). At constant p, the minimum disappeared at high temperatures (small ϵ and σ). As an example, for $N_k = 125, p = 0.06$ and $\sigma/\epsilon = 0.22, 2.2$ and 3 the minimum disappears for $\epsilon < 0.062, 0.2953$, and 0.8275, respectively. This shows that increasing σ enforces higher energy gain ϵ to make the crystal nucleus stable. Note the approximate scaling ϵ/σ^2.

Chapter 6

Conclusions and further studies

6.1 Conclusions

Part I of this work presented numerical results from extensive MD simulations of the crystallization process of a single PE chain with $N = 500$ monomers. The chain, after suitable equilibration at high temperature is cooled at the final temperature T_f by quenches involving or not intermediate annealing steps at T_{ann}. In addition, it is also isothermally annealed at T_f after initial preparation in the fully-stretched "all-trans" configuration. At $T_f = 11$ the chain remains amorphous for most time with occasional attempts to crystallize. For $T_f < 11$ the development of the ordered structure proceeds along different routes involving either the global reorganization of the chain or, alternatively, well-separated connected nuclei. The latter process was previously observed only for much longer chains. Differently from the early crystallization stages, no dependence on the thermal history was observed at late stages. At $T_f = 10$ the chain does not reach a single stationary state but continuously converts between different ordered configurations. At $T_f = 9$ the folding process of the chain involves several intermediate ordered metastable states in strong analogy with the experiments on n-alkanes [180] which finally yields a well-defined long-lived lamella with ten stems of ap-

proximately equal length, arranged into a regular, hexagonal pattern. We take the evidence of metastable intermediate states as a *microscopic* manifestation of the Ostwald step rule stating that in the course of transformation of an unstable (or metastable) state into a stable one the system does not go directly to the most stable conformation but prefers to reach intermediate stages having the closest free-energy to the initial state [273]. Both the metastable states and the long-lived one are well evidenced as local and global minima of the free-energy landscape (FEL), respectively.

The characterization of the microscopic organization of the lamella evidenced that the two caps are rather flat, i.e. the loops connecting the stems are short, a conclusions which may be also drawn from other experimental [188] and numerical studies [203]. Interestingly, annealing the chain through the different metastable states leaves the average number of Kuhn segments per loop λ nearly unchanged. It is also seen that the chain ends, the so-called cilia, are localized on the surface of the lamella, in agreement with the experiments [188], and that structural fluctuations take place on the lamella surface, as noted by recent MonteCarlo simulations [204]. This shows that the global minimum of FEL corresponds to a set of microscopic states with the same crystalline core and different surface configurations of the cilia and the two caps. The findings will be of help to improve a recent analytic model of the global minimum of the FEL [129].

Finally, the study of the melting process evidenced that the degree of hysteresis is small, in agreement with other MonteCarlo studies. Furthermore, at temperatures a little bit higher than the freezing one, independent attempts to crystallize the chain have been observed.

A major issue in polymer crystallization is the dispute between kinetic and equilibrium theories. The prevailing kinetic was viewed as successful because of its ability to fit experimental data. Nowadays, new techniques, both experimental and simulative, start questioning this prevalence. Concerning the simulation presented in this thesis, the simulations seem to support the equilibrium hypoth-

esis, but we have to appreciate a fundamental difference: the simulations span a range of time scales which is much shorter than the ones experimentally accessible. This means that statements that are valid when a crystal has already started growing, do not necessarily apply for nucleation, where a crystal does not yet exist. The LH theory, indeed, explains what happens during the growth process, when the crystal has a surface which is large enough to be considered infinite in comparison with the dimension of a single molecule. This situation (crystal much more extended than a single molecule) never realises in our simulations. Thus, our work must be considered as part of tentative initial efforts to study polymer crystallization and we must admit that results of significance for understanding polymer melt crystallization by MD do not exist. Our results might have some significance for crystallization from solution where a few chains are involved and where the crystallization process is relatively fast.

6.2 Further studies

From the work until here done, some questions arise which ask for an answer. Follows a quick list of the main issues:

- all the data presented deal with one single polymer chain of molecular weight corresponding to 500 monomers. This situation shows up that the chain is able to achieve an equilibrium conformation of ten stems. Increasing in the number of monomers, may generate a more complex crystallization behaviour, and the equilibrium conformation can probably be replaced by a kinetic one. In our knowledge, the longest chain employed until now for a model like us, correspond to a macromolecules of 2000 monomers [122], where an equilibrium conformation was found.

- Also an increasing of the number of chains can be intriguing [121, 274, 275]. In this case we can study the importance of entanglements among chains,

the growing front and the organization of the multichain crystal.

- Another limit in our tractation concerning the use of one molecule: this case is very interesting, but it is provided to the molecule all the time it needs to find a comfortable disposition which corresponds to the minimum of the free energy landscape. If molecules are very long and they start colliding with each other after a short time, probably the situation can be more complex, and the possibility to reach the minimum of the free energy potential could decrease to zero.

- The melting temperature is exceedingly high and calls for refinements of the force field (section 2.2). From ref. [123], pag 555 (answer to A.H. Windle), can be inferred that using an all atom model is possible to compare directly the results with the experimental findings.

- The theory developed in chapter 5 was devoted only to the determination of the minimum of the FEL, i.e. the equilibrium final structure. The model can be made more interesting including a finer description of the chain, hopefully considering the contribution of more than one chain [268, 269].

- In sections 1.2 and 3.2 was introduced how the molecular structure affects the stability of the crystal, which leads to changes in the melting temperature. With the use of molecular simulation would be possible shaping the potentials, chain lengths, and other properties of the model in order to test the effect of all these parameters on the melting point. This has to be considered as a major issue for following studies. An interesting experimental study on this problem can be found in refs. [276, 277], and in references in the sections cited above.

Part II

New Algorithms for the Integration of the Equations of Motion

Chapter 7

Algorithms for stochastic simulations

This chapter deals with the problem of the integration of the equations of motion. The chapter begins with a quick survey on the problem related with the simulations of polymeric (and biological) materials, where the different strategies employed to reproduce the correct dynamics of the system on a computer are reported. From this beginning, we move in the specific field of molecular dynamics simulation. The first aspect is related to the integration of the equation of motion in a deterministic way, which is a necessary introduction in order to develop quasi-symplectic stochastic algorithms. The last part is devoted to the description of the particular problem of integrating the Langevin equation. The results here presented, appeared in ref. [278].

7.1 Computer simulations of polymers

The physics of macromolecules is a major research field with extremely important applications to both the material science and the biology, In recent years, computer simulations have developed into a powerful tool for studying the dynamic, structural, and topological features of macromolecular systems. A major

challenge in these studies is the large spectrum of length and time scales characterizing both the molecular structure and the motion.

From this respect, one is interested in algorithms which may make use of long time steps in the integration of the equations of motion, in order to investigate the slow dynamics, with limited or no loss of accuracy to sample the short time dynamics in an accurate way. That issue will be discussed in what follow by referring us to the case of polymers where a large number of monomers are linked together by covalent bonds.

The polymer physics is dominated by interactions over several space/time scales, particularly when the molecular weight (MW) of the constituent chains exceeds the characteristic value for the formation of entanglements [7–9, 11]. Heretofore, molecular dynamics simulation studies of polymer systems have been limited to relatively short chains, and short time spans, rarely exceeding a few decades of nanoseconds. However, a robust sampling of the configuration space of truly polymeric substances is a prerequisite for the reliable prediction of their physical properties and the development of computer-aided materials design strategies.

The Monte Carlo (MC) method offers an excellent alternative to molecular dynamics (MD) for the simulation of dense polymer systems. Through the design of clever moves, configurational sampling can be dramatically enhanced. MC moves such as concerted rotation [279], configurational bias [280, 281], and internal configurational bias [282] have thus successfully addressed the problem of equilibrating polymer systems of moderate chain lengths. However, even these moves prove incapable of providing equilibration when applied to polymer melts of molecular length exceeding about one hundred monomers.

A solution to this problem was given by the development and efficient implementation of a chain-connectivity altering MC move, end-bridging (EB) [283–285]. Using EB, atomistic systems consisting of a large number of long chains, up to one thousand monomers, have been simulated in full atomistic detail [284, 285]. Similar efforts, employing chain-connectivity altering segmental rearrangements,

include the cooperative motion algorithm (CMA) [286] used in lattice-based simulations of complex polymer systems and an off-lattice MC study of the interphase between crystals with freely rotating chains [287].

Despite its remarkable efficiency in equilibrating long chain polymer melts, EB suffers from three shortcomings: (a) It cannot equilibrate monodisperse polymer melts; a finite degree of polydispersity is necessary for the move to function. While this is not a drawback in modeling industrial polymers, which are typically polydisperse, the ability to equilibrate strictly monodisperse polymers is highly desirable for comparing against theory or experiments on anionically synthesized model systems. (b) It relies on the presence of chain ends. Thus, it does not offer itself for dense phases of chains with nonlinear architectures containing long strands between branch points such as H-shaped polymers, for cyclic molecules, or for model polymer systems of infinite chain length. (c) Its performance drops considerably as the stiffness of chains increases or in the presence of chain orientation. In order to overcome these problems, new connectivity-altering moves, involving two bridging trimers among four properly chosen monomers along one or two chains in the system were developed [288, 289].

Many problems in complex soft matter systems are inherently multiscale in nature, i.e., microscopic interactions are coupled strongly to meso- and macroscopic properties. Despite the increasing computational power and ongoing efforts to enhance the efficiency of MD integration algorithms [290–294], all-atom MD simulations are often incapable to cover the time and length scales needed in order to reach relaxation in a typical molecular system, such as a polymer solution or melt. In many cases it is also questionable whether a huge amount of detailed information is needed (e.g. the chemical details affect the prefactors of the universal power laws only), and might not even obscure the relevant information.

One first way to tackle this is to reduce the number of degrees of freedom by systematic coarse graining, which retains only those degrees of freedom that are relevant for the particular property of interest. Since some specific chemical

details are usually lost in the coarse-graining procedure, much effort has been devoted recently to the development of multiscale modeling approaches, where different parts of the system are modeled at different levels of detail to account for the local resolution requirement [295–300]. The dynamics of a polymeric liquids are typically described in terms of the Rouse and reptation models [7–9, 11].

For short chains the topological constraints do not play a dominant role. For a given chain, the presence of the other chains is accounted for by a stochastic background. The dynamics of the chain is described by a Langevin equation augmented by the constraints due to the chain connectivity (Rouse model) [301, 302]. That model describes the long-time behaviour very well and belong to the class of models where the stochastic behaviour pictures the coupling with a thermal bath (alternatively, one may modify the equations of motion by coupling the system to an additional degree of freedom [303–306]). In the Langevin dynamics formalism, the degrees of freedom of the bath are eliminated by using the Mori-Zwanzig projection technique [307, 308]. The result is a set of stochastic differential equations describing the dynamic state of the target system [309]. Langevin dynamics has been also used to accelerate the exploration of the high-dimensional configuration space of macromolecules [310].

Within an approach based on stochastic differential equations, symplectic algorithms are noteworthy. Symplectic integrators are numerical integration schemes for Hamiltonian systems, which conserve the symplectic two-form $dp \wedge dq$ exactly, so that $(q(0), p(0)) \rightarrow (q(\tau), p(\tau))$ is a canonical transformation. For both explicit and implicit integrators it was shown that the discrete mapping obtained describes the exact time evolution of a slightly perturbed Hamiltonian system and thus possesses the perturbed Hamiltonian as a conserved quantity. That feature is of interest in common integration schemes which conserve not the complete Hamiltonian, but some other quantity which slightly differs from it [311–315]. Symplectic algorithms guarantee that, in spite of the local truncation error, the total energy (which should be conserved exactly in the original flow) exhibits

limited errors growing in time, the so called secular errors. If the integrator is not symplectic, secular errors of the total energy are usually observed. Dedicated symplectic algorithms were derived for studying the monodimensional motion of a single brownian particle [311, 316]. In that case the equation of motion is:

$$\dot{v} = F(x) - \gamma v + \xi(t)\,, \tag{7.1}$$

where the mass of the particle is unitary, x is the position, $v = \dot{x}$ the velocity, $F(x)$ the force, γ is the damping factor and $\xi(t)$ is a random Gaussian noise, with zero average and standard deviation

$$\langle \xi(t)\xi(s) \rangle = 2\gamma T \delta(t-s) \tag{7.2}$$

where T is the temperature of the system. It will be proved in chapter 8 that the above dedicated algorithms are also well-suited for studies of multi-particle systems in the usual 3D space. To this aim, the dynamics of a single polymer chain in dilute solution will be considered [7, 11, 28]. Trajectories were generated by the above symplectic algorithms and compared with some popular alternatives .

7.2 Symplectic integrators

First of all we start describing the physical problem we want to solve: having defined the initial positions and velocities of the system, we want to compute the time evolutions of the system. This problem is very common in physics and various analytical formulations are available.

For example we can consider the Liouville operator L for a system with f degrees of freedom:

$$iL = \{\Gamma, ...\} = \sum_{j=1}^{f} \left[\dot{x}_j \frac{\partial}{\partial x_j} + F_j \frac{\partial}{p_j} \right] \tag{7.3}$$

where $\Gamma = \{x_j, p_j\}$ are the positions and conjugate momenta of the system, F_j is the force on the j degree of freedom and $\{..., ...\}$ is the Poisson bracket of

the system. L is a linear Hermitian operator on the space of square integrable functions of Γ. The state of the system at time t is given by

$$\Gamma(t) = U(t)\Gamma(0) \tag{7.4}$$

where the classical exact propagator is defined as:

$$U(t) = \exp(iLt) \tag{7.5}$$

Everything said until now in this section is well known by every physician, so is not necessary to enter into deep details, but underline some aspects which will be interesting in what follows:

1. $U(t)$ is time reversible
2. in the microcanonical NVE ensemble the energy $< H >$ is conserved
3. $U(t)$ is symplectic (see below).

7.2.1 Symplecticity

A transformation in phase space from positions x and momenta p

$$\bar{x} = \alpha(x, p), \quad \bar{p} = \beta(x, p) \tag{7.6}$$

is said to be *symplectic* [317–320] if its Jacobian matrix (of partial derivatives) satisfies

$$\begin{bmatrix} \frac{\partial\alpha}{\partial x} & \frac{\partial\alpha}{\partial p} \\ \frac{\partial\beta}{\partial x} & \frac{\partial\beta}{\partial p} \end{bmatrix}^T \begin{bmatrix} 0 & I \\ -I & 0 \end{bmatrix} \begin{bmatrix} \frac{\partial\alpha}{\partial x} & \frac{\partial\alpha}{\partial p} \\ \frac{\partial\beta}{\partial x} & \frac{\partial\beta}{\partial p} \end{bmatrix} = \begin{bmatrix} 0 & I \\ -I & 0 \end{bmatrix} \tag{7.7}$$

where I is the identity matrix. If this is true, then the trasformation $(x, p) \mapsto (\alpha, \beta)$ preserves symplectic structure as follow [313, 320–322]:

$$d\alpha \wedge d\beta = dx \wedge dp \tag{7.8}$$

It is straightforward to show that the composition of symplectic transformation is symplectic.

Now it is appropriate to consider first the question of what kind of accuracy is expected from a simulation. Trajectories of molecular dynamics (MD) simulations are chaotic. That is, very small perturbations to initial conditions grow exponentially in time until they completely overwhelm the trajectory itself [126]. Hence, it is inappropriate to expect that accurate trajectories be computed for more than a short time interval. Rather, it is expected only that the trajectories have the correct statistical properties, which is sensible if, for example, the initial velocities are randomly generated from a Maxwell distribution.

The use of a numerical integrator to approximate the exact propagator of a system of ordinary differential equations (ODEs) yields a numerical solution which can be interpreted as the exact solution of a slightly different system of ODEs (backward error interpretation) [324–326]. If the given system is a Hamiltonian system (as it is for the constant-energy NVE ensemble in MD), then the slightly different system is Hamiltonian if and only if the integrator is symplectic [320]. In particular, this implies that any given energy surface in phase space is changed only slightly by the use of symplectic numerical integration, and it suggests that statistical properties of long time dynamics are retained. On the other hand violations of this property such as that produced by velocity rescaling lead to skewed energy distributions [323].

The exact propagator for a Hamiltonian system for any given time increment is symplectic. As a consequence it possesses the Liouville property of preserving volume in phase space. The most tangible benefit of symplecticity is stability, which follows from the near conservation of energy [318].

As said in ref. [327] “ an algorithm which transforms properly with respect to a class of transformations is more basic than one that does not. In a sense the invariant algorithm attacks the problem and not the particular representation used.”

7.2.2 Time reversibility

Reversibility is another important property that the numerical integrator should preserve. Any method which is based on the splitting of the Hamiltonian, is symplectic. This does not yet, however, guarantee that the method is also time reversible, which may also be considered as a strong requirement for the integrator. This property is guaranteed by symmetric methods, which also provide a better numerical stability [328].

It has been stated [328] that any lack of perfection of such reversal should be due to rounding-off errors only, not the program. Many symplectic integrators are reversible. Additional evidence favoring the use of symplectic integrators is an observation [329] concerning hybrid Monte Carlo methods: to get the property of detailed balance needed for valid sampling, it is enough to use a numerical integrator which is volume preserving and reversible. As was just mentioned, symplectic integrators preserve volume in phase space and many are reversible.

7.2.3 Operator splitting methods

Knowing eq. 7.5 we can try to develop a symplectic integration scheme.

First, let us consider the following problem [313, 330]. Let A and B be non-commutative operators and τ be a small real number. For a given n integer (later to be identified with the order of the integrator), find a set of real numbers $(c_1, c_2, ..., c_k)$ and $(d_1, d_2, ..., d_k)$ such as

$$\exp[\tau(A+B)] = \prod_{i=1}^{k} \exp(c_i \tau A) \exp(d_i \tau B) + o(\tau^{n+1}) \tag{7.9}$$

As an example, for $n = 2$ and $k = 2$, one finds:

$$\exp[\tau(A+B)] = \exp(\frac{1}{2}\tau A) \exp(\tau B) \exp(\frac{1}{2}\tau A) + o(\tau^3) \tag{7.10}$$

The above general problem is directly related to the symplectic integrator of a Hamiltonian $H(p,q) = T(p) + V(q)$ [313].

In a symplectic algorithm one key step is the separation of the Liouvillian in two terms L_1 and L_2 such as $L = L_1 + L_2$. For second-order integrators ($n = 2$, $k = 2$) the total propagator allows to be decomposed as [313, 330–333]:

$$\exp\left[i(L_1 + L_2)t\right] = \left\{\exp\left[iL_1(h/2)\right]\exp\left[iL_2(h)\right]\exp\left[iL_1(h/2)\right]\right\}^P \tag{7.11}$$

where $h = t/P$. From this one defines the discrete time propagator as:

$$G(h) = U_1\left(\frac{h}{2}\right)U_2\left(h\right)U_1\left(\frac{h}{2}\right) = \exp\left[iL_1(h/2)\right]\exp\left[iL_2(h)\right]\exp\left[iL_1(h/2)\right] \tag{7.12}$$

Notice that the propagator $G(h)$ is time reversible and symplectic. As an example, the Liouvillian, Eq.7.3, may be separated as [335]:

$$iL_1 = \sum_{j=1}^{f} \dot{x}_j \frac{\partial}{\partial x_j}; \quad iL_2 = \sum_{j=1}^{f} F_j \frac{\partial}{\partial p_j} \tag{7.13}$$

The above choice leads to the Velocity Verlet algorithm (VV) which in one dimension takes the form [336] (see also section 2.4):

$$\begin{aligned} x(t+h) &= x(t) + hv(t) + \frac{1}{2}h^2\dot{v}(t) \\ v(t+h) &= v(t) + \frac{1}{2}h\left[\dot{v}(t) + \dot{v}(t+h)\right] \end{aligned} \tag{7.14}$$

where h is the integration time step and $\dot{v}$ is given by the deterministic equation of motion. If iL_1 and iL_2 are exchanged, the position Verlet algorithm is obtained [334]. Both algorithms are correct to second order.

7.2.4 Accuracy

Now we move to analyse another, more subtle problem: the accuracy. In order to grasp the main ideas we have to understand the process followed in order to write down an integration scheme. For our purpose we consider the generic form of a time-reversible symplectic algorithm with $n = 2$ and $k = 3$ [335]:

$$e^{i(L_1+L_2)h} = e^{iL_1\chi h}e^{iL_2h/2}e^{iL_1(1-2\chi)h}e^{iL_2h/2}e^{iL_1\chi h} + Ch^3 + O(h^4) \tag{7.15}$$

following from eq. 7.9 at $c_1 = c_3 = \chi$, $c_2 = 1 - 2\chi$, $d_1 = d_2 = 1/2$ ad $b_3 = 0$. Again iL_1 and iL_2 can be exchanged. Formula 7.15 represents a whole family of symplectic time-reversible integrators of the second order in which a particular member can be extracted by choosing a value for the free parameter χ. The case $\chi = 0$ reduces to the VV algorithm. In the case $\chi \neq 0$, the main difference from VV is the requirements of two force evaluations instead of one. For this reason, we can come to an incorrect conclusion that such a propagation has no advantage over the Verlet algorithms.

In order to prove that the above conclusion is indeed incorrect, let us analyze in more detail the influence of truncation errors Ch^3 on the result. Expanding both the sides of Eq. 7.15 into Taylor's series with respect to h, one finds

$$C = \alpha(\chi)[A,[B,A]] + \beta(\chi)[B,[B,A]] \tag{7.16}$$

where

$$\alpha(\chi) = \frac{1 - 6\chi + 6\chi^2}{12}, \quad \beta(\chi) = \frac{1 - 6\chi}{24} \tag{7.17}$$

The norm of C with respect to the third-order commutators $[A,[B,A]]$ and $[B,[B,A]]$ is

$$\gamma(\chi) = \sqrt{\alpha^2(\chi) + \beta^2(\chi)} \tag{7.18}$$

Then the norm of local uncertainties $C\rho h^3$ appearing in phase trajectory ρ during a single-step propagation given by Eq. 7.15 can be expressed in terms of γ and h as $g = \gamma h$. During a whole integration over a fixed time interval t, the total number P of such single steps is proportional to h^{-1}. As a result, the local third-order uncertainties will accumulate step by step leading at $t \gg h$ to the second order global errors $\varepsilon = gh^{-1}$, i.e.,

$$\varepsilon(\chi, h) = \gamma(\chi)h^2 \tag{7.19}$$

Now, we are able to make comparisons.

First of all we can suppose that minimizing the global error is the main purpose of this tractation. The minimum of ε can be found [335] and this algorithm is 11

times more accurate than VV (case $\varepsilon(\chi = 0, h)$). Remembering that the extended propagation requires two force evaluation per time step h, it should be performed with double step size $2h$ with respect to that of the Verlet algorithms, in order to provide the same number of total force recalculations during the integration over the same time interval. In this case the accuracy is 3 times better that VV. This means that algorithms with more than one force evaluation (and so slower) could be preferred because they can obtain longer time step and also an increasing in accuracy.

A second point is that position and velocities can be computed with a different accuracy [335].

For instance, some MD applications are aimed exclusively at the investigation of structural properties of the system. Then the accuracy of determining particle positions will play a more important role than that of velocities. In such a situation, it is quite natural to increase the precision in evaluation of the positions. In this way we lose accuracy on velocities (in fact, it is not possible to have simultaneously $\alpha(\chi) = \beta(\chi) = 0$).

7.2.5 Summarizing

Before leaving the presentation of symplectic integrators, we summarize the main points, which will be important in what follows:

- Algorithms which are developed in order to preserve some symmetries of the system are preferable because of less "deformation" of the exact phase space. See section 7.2.1.

- Time reversibility is not usually guarantee: it has to be explicitly requested during the algorithm developed. See section 7.2.2.

- Algorithm with less force evaluation are faster, but algorithm with more force evaluation can achieve longer time steps, with even best accuracy. See

section 7.2.4.

- The algorithms can be fine tuned imposing additional requests in order to achieve a better computation of the important variables of the problem to be solved. See section 7.2.4.

With this considerations we can leave the field of deterministic algorithms and move to the field of stochastic integration schemes. We will concentrate our attention on Langevin-type equations.

7.3 Stochastic methods

When we talk about stochastic processes, in general we describe the process by means of its statistical properties. This lead straightly to the heart of the problem: stochastic algorithm has to reproduce statistical properties (i.e. distribution) correctly. Instead, in deterministic algorithms, the attention is usually pointed at their ability to conserve some constant of the motion, such as energy or moments.

In particular, we remember that the Langevin equation (eq.7.1) is equivalent to a Fokker-Plank equation for the phase space density function [337, 338], which has the canonical ensemble distribution as a stationary solution:

$$P(x, v) = \mathcal{N} \exp(-(v^2/2 + V(x))/T) \tag{7.20}$$

where $\mathcal{N}$ is the normalization constant, v is the velocity, x the position, T the temperature, and V the potential.

Follows a brief introduction on the ability of the algorithms to reproduce the correct distribution.

7.3.1 Reproducing equilibrium distribution

Obviously an algorithm reproduce the correct distribution eq 7.20 only with a partial accuracy.

Considering a general integration pattern [311, 312]:

$$y_i(t+h) = y_i(t) + G_i(y_i, \xi, h) \tag{7.21}$$

where y_i is the i-th degree of freedom and G_i is generally different for every degrees of freedom. Then the probability distribution of y_i satisfies the Kramers-Moyal expansion [339]

$$P(y_i, t+h) - P(y_i, t) = \sum_{n=1}^{\infty} \sum_{y_i} \frac{\partial}{\partial y_i} \dots \frac{\partial}{\partial y_n} K_{1\dots n} P(y_i, t) \tag{7.22}$$

with

$$K_{1\dots n} = (-1)^n \frac{1}{n!} \langle G_1 \dots G_n \rangle_\xi \tag{7.23}$$

where $< \cdots >_\xi$ means averaging over the noise realizations.

When the system reaches the equilibrium state, clearly

$$P(y_i, t+h) - P(y_i, t) = 0 \tag{7.24}$$

and the system achieves an equilibrium distribution, that differ from eq. 7.20 [311, 312]:

$$P(x, v)_{sim} = P(x, v) \times \exp\left(\sum_{n=1}^{\infty} h^n \frac{S_n(x, v)}{T} \right) \tag{7.25}$$

where $P(x, v)$ is the canonical ensemble distribution. The first nonzero S_n yields the corrections to the true equilibrium distribution generated by the numerical scheme.

Putting eqs. 7.24 and 7.25 in 7.22 the result is:

$$\sum_{n=1}^{\infty} \sum_{y_i} \frac{\partial}{\partial y_i} \dots \frac{\partial}{\partial y_n} K_{1\dots n} P(x, v)_{sim} = 0 \tag{7.26}$$

This equation is, substantially, a differential equation for the S_n. We come back to it after a rapid review of commonly used algorithms.

7.3.2 Requests for integration schemes

A lot of different routes can be followed to write down numerical integration schemes. In particular one has to bear in mind the particular problem he wants to solve. A simple observation is that eq. 7.1, when $\gamma \to 0$, becomes symplectic. This means that for small values of γ it will be reasonable working with algorithm which in the case $\gamma = 0$ works fine, for example symplectic algorithms [311, 340](see section 7.2). An example of such a problem follows.

A straightforward method of conducting stochastic simulations has been developed by Ermak [341, 342]:

$$\begin{aligned} x(t+h) &= x(t) + c_1 h v(t) + c_2 h^2 F(x(t)) + \xi_1 \\ v(t+h) &= c_0 v(t) + c_1 h F(x(t)) + \xi_2 \end{aligned} \tag{7.27}$$

where

$$c_0 = e^{\gamma h} \quad c_1 = \frac{1-c_0}{\gamma h} \quad c_2 = \frac{1-c_1}{\gamma h} \tag{7.28}$$

and the two stochastic variables ξ_1 and ξ_2 are two random gaussian variables with zero average and moments

$$\begin{aligned} \langle \xi_1^2 \rangle &= \frac{Th}{\gamma}\left(2 - \frac{3 - 4e^{-\gamma h} + e^{-2\gamma h}}{\gamma h}\right) \\ \langle \xi_2^2 \rangle &= T\left(1 - e^{-2\gamma h}\right) \\ \langle \xi_1 \xi_2 \rangle &= \frac{T}{\gamma}\left(1 - e^{-\gamma h}\right)^2 \end{aligned} \tag{7.29}$$

Ermak's algorithm is an attempt to treat properly both the systematic dynamic and stochastic elements of the Langevin equation. The problems arise when $\gamma \to 0$: in this limit the eqs. 7.27 become a simple Taylor series predictor algorithm, which is not a particularly accurate method of conducting simulations [126]. In fact, for the case when $V(x) = \omega^2 x^2/2$, the numerical equilibrium distribution at lowest order in h is [311]

$$P(x,v) = \mathcal{N} \exp[-(v^2/2 + \omega^2 x^2/2)/\widehat{T}] \tag{7.30}$$

where

$$\widehat{T} = \frac{T}{1 + \frac{\omega^2 h}{2\gamma}}$$

This example shows that the numerical equilibrium distribution is similar to the correct one, but with a renormalization of the temperature. If $\gamma \to 0$, then $\widehat{T} \to 0$; thus, for small values of γ the algorithm stops working properly.

In order to overcame these problems, what is needed is a stochastic generalization of the velocity Verlet algorithm [126](from now called *Li*):

$$\begin{aligned} x(t+h) &= x(t) + c_1 h v(t) + c_2 h^2 F(x(t)) + \xi_1 \\ v(t+h) &= c_0 v(t) + (c_1 - c_2) h F(x(t)) + c_2 h F(x(t+h)) + \xi_2 \end{aligned} \tag{7.31}$$

where the coefficients and the random variables are the same as in eqs. 7.27. This algorithm reproduces the correct equilibrium distribution at $O(h)$, but there are still corrections $O(h^2)$ in the exponent [311].

7.3.3 Quasi symplectic stochastic integration

In this section we want to test a series of new algorithms, which can be helpful in the integration of the Langevin equation. First of all we start with a symplectic, deterministic algorithm:

$$\begin{aligned} \bar{x} &= x(t) + \frac{h}{2} v(t) \\ v(t+h) &= v(t) + h F(\bar{x}) \\ x(t+h) &= \bar{x} + \frac{h}{2} v(t+h) \end{aligned} \tag{7.32}$$

This algorithm is known as leap-frog or position Verlet (see section 7.2.3 for its derivation). In order to reintroduce both the dissipation and the noise, it is possible to write the previous scheme in the generic form [311]:

$$\begin{aligned} \tilde{x} &= x(t) + \frac{h}{2} v(t) \\ v(t+h) &= c_2 \left[c_1 v(t) + h F(\tilde{x}) + d_1 \xi \right] \\ x(t+h) &= \tilde{x} + \frac{h}{2} v(t+h) \end{aligned} \tag{7.33}$$

where ξ is a random Gaussian variable with unitary standard deviation and zero average. Putting this scheme into eq.7.26 and imposing that the term S_1 vanishes, we can determine the unknown coefficient c_1 and c_2 [311]:

$$c_1 = 1 - \frac{\gamma h}{2} \qquad c_2 = \frac{1}{1+\gamma h/2} \qquad d_1 = \sqrt{2T\gamma h}$$

This algorithm is able to reproduce the probability distribution of position up to an order $O(h)$ (which has not to be confused with the order of the integrator), and we will refer to it as *SLO*, from Symplectic Low Order.

Looking at the structure of the previous algorithm, it is possible to derive an algorithm of higher order. The idea is that if one could increase the number of unknown quantities, one might be able to make the terms $O(h^2)$ vanish. To obtain this, two steps of the forms eq. 7.33 with time step $h/2$ are combined [311]:

$$\begin{aligned}
x_1 &= x(t) + \frac{h}{4}v(t) \\
v_1 &= c_2\left[c_1 v(t) + \frac{h}{2}F(x_1) + \sqrt{\gamma T h}\,(a_1\xi_1 + a_2\xi_2)\right] \\
x_2 &= x_1 + \frac{h}{2}v_1 \\
v(t+h) &= c_2\left[c_1 v_1 + \frac{h}{2}F(x_2) + \sqrt{\gamma T h}\,(b_1\xi_1 + b_2\xi_2)\right] \\
x(t+h) &= x_2 + \frac{h}{4}v(t+h)
\end{aligned} \tag{7.34}$$

with:

$$\begin{aligned}
c_1 &= 1 - \frac{\gamma h}{4} \\
c_2 &= \frac{1}{1+\gamma h/4} \\
a_1 &= -1.0691860043307065... \\
a_2 &= -0.1533230407019893... \\
b_1 &= 0.3044913128854065... \\
b_2 &= -1.0363164126095790...
\end{aligned}$$

here ξ_1 and ξ_2 are two random Gaussian variables with unit standard deviation and zero average. This algorithm will be referred as *SHO*, Symplectic High Order.

Equation 7.33 can be used to obtain quasi-symplectic algorithms of arbitrarily high order in the frictionless deterministic limit which reproduce the correct equilibrium distribution of to $O(h)$ order in the exponent (i.e. the same order of SLO scheme above). Given a generic deterministic symplectic scheme of order N

$$\begin{aligned} p(i) &= p(i-1) + hb_i F(q(i-1)) \\ q(i) &= q(i-1) + ha_i p(i) \end{aligned} \tag{7.35}$$

there is a corresponding quasi-symplectic algorithm which reads(one dimensional case) [312]

$$\begin{aligned} p(i) &= c_{2,i}\left[c_{1,i}p(i-1) + b_i(hF(q(i-1)) + \xi)\right] \\ q(i) &= q(i-1) + ha_i p(i) \end{aligned} \tag{7.36}$$

where $i = 1, N$ and

$$c_{1,i} = 1 - \frac{h}{2}\gamma b_i \qquad c_{2,i} = \frac{1}{1 + \gamma h b_i/2} \tag{7.37}$$

and where ξ is a random gaussian variable with average zero and standard deviation $2T\gamma h$. It is important to stress that the variable ξ is the same for each of the i steps within the integration step h.

7.3.4 Summarizing

In this section we underline the main issues treated in the above analysis of stochastic algorithms:

- Stochastic algorithm can reproduce the exact equilibrium distribution only partially (see section 7.3.1); with a suitable choice of the parameters is possible, in some cases, to obtain more accurate schemes, which are usually more complex than low order schemes (see section 7.3.3).

- Working with low values of γ, algorithms which are symplectic in the limit $\gamma \to 0$ are preferable (see section 7.3.2).

- In section 7.3.3, eq. 7.36 make possible obtain quasi-symplectic algorithm from the research on symplectic, deterministic schemes.

Chapter 8

Benchmark of the new algorithms

In the previous chapter were presented the main ideas behind the integration schemes for both deterministic and stochastic dynamics; for some of these algorithms a detailed derivation has been proposed, and comments on their properties has also been done. Now we are interested to know their performance in the integration of the Langevin equation for the system presented in chapter 3, in order to check if any improvement is possible over the VV scheme.

8.1 New algorithms

The algorithm we want to test are the SLO (eq. 7.33) and SHO (eq. 7.34) schemes. In addition, by means of eq. 7.36 presented in chapter 7, it is possible to write the stochastic scheme for a fourth-order Hamiltonian Runge-Kutta (from now, HRK4) [312, 343]:

$$\begin{aligned} v_i &= c_i^{(2)} \left[c_i^{(1)} v_{i-1} + b_i(F(x_{i-1})) + d_1 \xi \right] \\ x_i &= x_{i-1} + h a_i v_i \end{aligned}$$

where $1 \leq i \leq 4$ and:

$$\begin{aligned} x_0 = x(t) \quad &, \quad v_0 = v(t) \\ x_4 = x(t+h) \quad &, \quad v_4 = v(t+h) \end{aligned}$$

$$\begin{aligned} a_1 = 0.515352837431123 \quad &, \quad b_1 = 0.134496199277431 \\ a_2 = -0.085782019412974 \quad &, \quad b_2 = -0.224819803079421 \\ a_3 = 0.441583023616467 \quad &, \quad b_3 = 0.756320000515668 \\ a_4 = 0.128846158365384 \quad &, \quad b_4 = 0.334003603286321 \end{aligned}$$

$$\begin{aligned} c_i^{(1)} &= 1 - \frac{\gamma h}{2} b_i \\ c_i^{(2)} &= \frac{1}{1 + \frac{\gamma h}{2} b_i} \end{aligned}$$

8.2 Benchmark algorithms

The performance of the above presented algorithms are compared with other widely used algorithm. These are the VV (eq. 2.4 and eq. 7.14) and the Li (eq. 7.31) algorithms. Another very common algorithm is the BBK scheme developed by Brünger, Brooks, Karplus [344]:

$$\begin{aligned} \tilde{v} &= v(t) + \frac{h}{2} F(x(t)) \\ x(t+h) &= x(t) + \frac{[1 - \exp(-\gamma h)]}{\gamma} \tilde{v} + \sqrt{2T/\gamma}\zeta_2 \\ v(t+h) &= \exp(-\gamma h)\tilde{v} + \frac{h}{2} F(x(t+h)) + \sqrt{2T\gamma}\zeta_1 \end{aligned} \tag{8.1}$$

The stochastic variables ζ_1, ζ_2 are defined as:

$$\begin{aligned} \zeta_1 &= \sqrt{\tau_2}\xi_1 \\ \zeta_2 &= \frac{\tau_1 - \tau_2}{\sqrt{\tau_2}}\xi_1 + \sqrt{h - \frac{\tau_1^2}{\tau_2}}\xi_2 \end{aligned}$$

where ξ_1 and ξ_2 are two uncorrelated gaussian variables with zero average and unit standard deviation and

$$\tau_1 = \frac{1}{\gamma}\left[1 - e^{-\gamma h}\right] \qquad \tau_2 = \frac{1}{2\gamma}\left[1 - e^{-2\gamma h}\right]$$

8.3 Model and details of simulations

The system to be used to test the different algorithms presented is the model already presented in chapter 2. It describe a single polymer chain with $M = 20$ monomers in solution. It was studied in detail by the present [129, 130, 265] and other authors [121, 122, 345]. The difference from the model presented in chapter 2 is that now the Lennard-Jones cutoff is located at $r_{\text{cut}} = 2^{1/6}\sigma$ (that is the Lennard-Jones minimum), in order to have an increase in computational speed. What is worth noticing now is that the motion is described by the Langevin equation

$$\ddot{\mathbf{r}}_i = -\nabla_i U - \gamma \dot{\mathbf{r}}_i - \boldsymbol{\xi}_i \tag{8.2}$$

where $\mathbf{r}_i$ denotes the position vector of the i-th bead, $\nabla_i U$ is the sum the internal forces acting on it, $-\gamma\dot{\mathbf{r}}_i$ is the frictional force and $\boldsymbol{\xi}_i$ is a gaussian noise with zero average and delta-like correlation:

$$\langle \boldsymbol{\xi}_i(t) \cdot \boldsymbol{\xi}_j(t') \rangle = 6\gamma k_B T \delta_{ij} \delta(t - t') \tag{8.3}$$

It is understood that the different cartesian component are mutually independent for $i = j$. All the simulations have been performed according to the following protocol. The system was initially equilibrated at the temperature $T = 9$. Then, a single configuration was singled out and used as seed for all the production runs with the different algorithms.

About the choice of the model, a point warrant emphasis. This model permits to check the performance of the algorithm on a system composed of different potentials mutually interacting. With respect to an harmonic solvable model it

presents the advantage that anharmonic features can also be addressed. Another aspect, more technical, is related to the equipartition of the energy, which is reached very slowly in the harmonic approximation. In this situation a well equilibrated configuration can alleviate that drawback [309].

8.4 Results and discussion

Below, we discuss our results splitting them into two parts pointing out the global and detailed aspects of the algorithms.

8.4.1 Global aspects

Stability and numerical efficiency

To compare the different algorithms, the integration time step, h, was changed to identify the largest value h_{max} above which each algorithm is unstable. The algorithm is defined as unstable if it crashes before 10^4 iterations . Usually this happens when the algorithm is unable to integrate in a correct way the faster degrees of motion (i.e. the bond potential in the present case); in that case a fast increase in global energy (driven by the increase in the bond energy) is observed which leads the simulations to crash. From this respect, different behaviors were observed. SVV, SLO, BBK, Li become unstable for $h_{max} \cong 3.4 \cdot 10^{-3}$ whereas SHO ($h_{max}^{SHO} \cong 6.6 \cdot 10^{-3}$) and HRK4 ($h_{max}^{HRK4} \cong 4.4 \cdot 10^{-3}$) are stable for longer time steps. The main instability source stems from the fast oscillations triggered by the potential setting the bond length, Eq. 2.1. However, differently from the other algorithms where only one force evaluation per integration step is needed, SHO and HRK4 require two and four force evaluations per integration step, respectively, i.e. they are computationally slower. It must be also noted that different algorithms involve the evaluation of different numbers of random variables. Even if the force evaluation is one crucial part of each integration step,

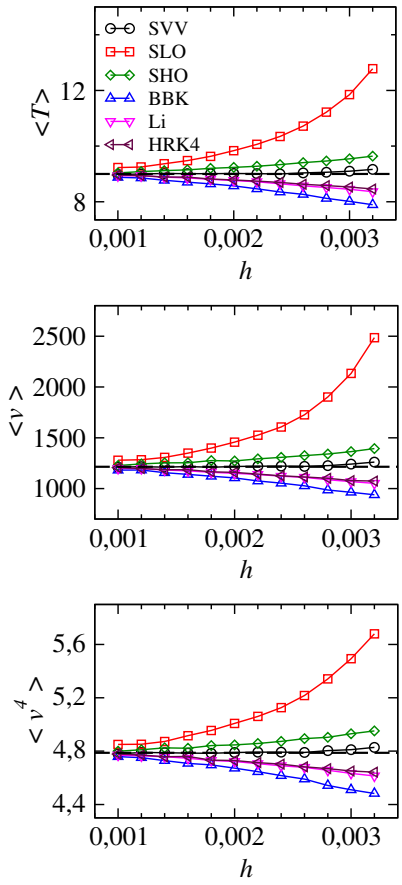

Figure 8.1: The average temperature $< T >$ and the first and fourth moments of the probability distribution of the modulus of the velocity $< v >$ and $< v^4 >$, respectively. The superimposed dashed lines are the expected theoretical values. The absence of error bars from the present figure and the next ones implies that they are smaller than the symbol size.

the evaluation of random variables by using reliable routines [343, 347] may affect the performance of the integration routines for small systems [311].

As outlined in Sec. 7, the number of stochastic variables is different for each algorithm: SHO, BBK and Li require two random variables, whereas SVV, SLO, HRK4 involve only one random variable. As it will be evident in section 8.4.2, no systematic differences are evidenced at short h values. Increasing the h value leads to instabilities, which are related with the integration scheme of the different algorithms.

Stabilization of the deterministic part

In the low friction regime, of interest here, the effective integration carried out by both the stochastic and the deterministic parts of the algorithm is crucial. Augmenting symplectic algorithms by adding stochastic and dissipative terms

seem to be a viable way to achieve this purpose [311, 312]. Here, we want to clarify the improvement in the stabilization of the algorithms due to their stochastic part.

It is possible to classify the algorithms in two groups: Li, BBK, stochastic VV, come from the VV splitting eq. 7.13; whereas SLO, SHO are a stochastic derivation of the PV splitting which exchanges the definitions of the liouvillians L_1 and L_2 with respect to the VV one; HRK4, instead, is a symplectic derivation of the standard Runge-Kutta schemes [348, 349]. It is known that the *d*eterministic VV splitting is better at small time steps, but, on increasing the time step, it becomes unstable more quickly than the *d*eterministic PV splitting [334]. For this reason it is usually thought that PV factorization is better than VV one for developing algorithms in order to reach longer time steps [350, 351].

Another approach to stabilize integration schemes with long time steps was pointed out by several authors who suggested the use of a Langevin coupling as a device to dump numerical resonances associated with symplectic algorithms [350–355]. In order to illustrate the Langevin stabilization let us compare the SVV and SLO algorithms both employing one single stochastic variable. The comparison is made, as usual, by evaluating the different kinetic and potential energy terms, see figs. 8.1 and 8.2 to be discussed in greater detail in Sec. 8.4.2. It is seen that the SVV algorithm is less stable as far as the potential energy is concerned, but the kinetic energy is more stable. On the other hand, SLO, derived by a PV splitting, performs as SVV to evaluate the potential energy, but it is worse as far as the kinetic energy is concerned. The total energy, as evaluated by SVV, is more stable. These findings suggest that the conclusions drawn for the deterministic algorithms (see above) cannot be extended to the stochastic counterparts in a straightforward way.

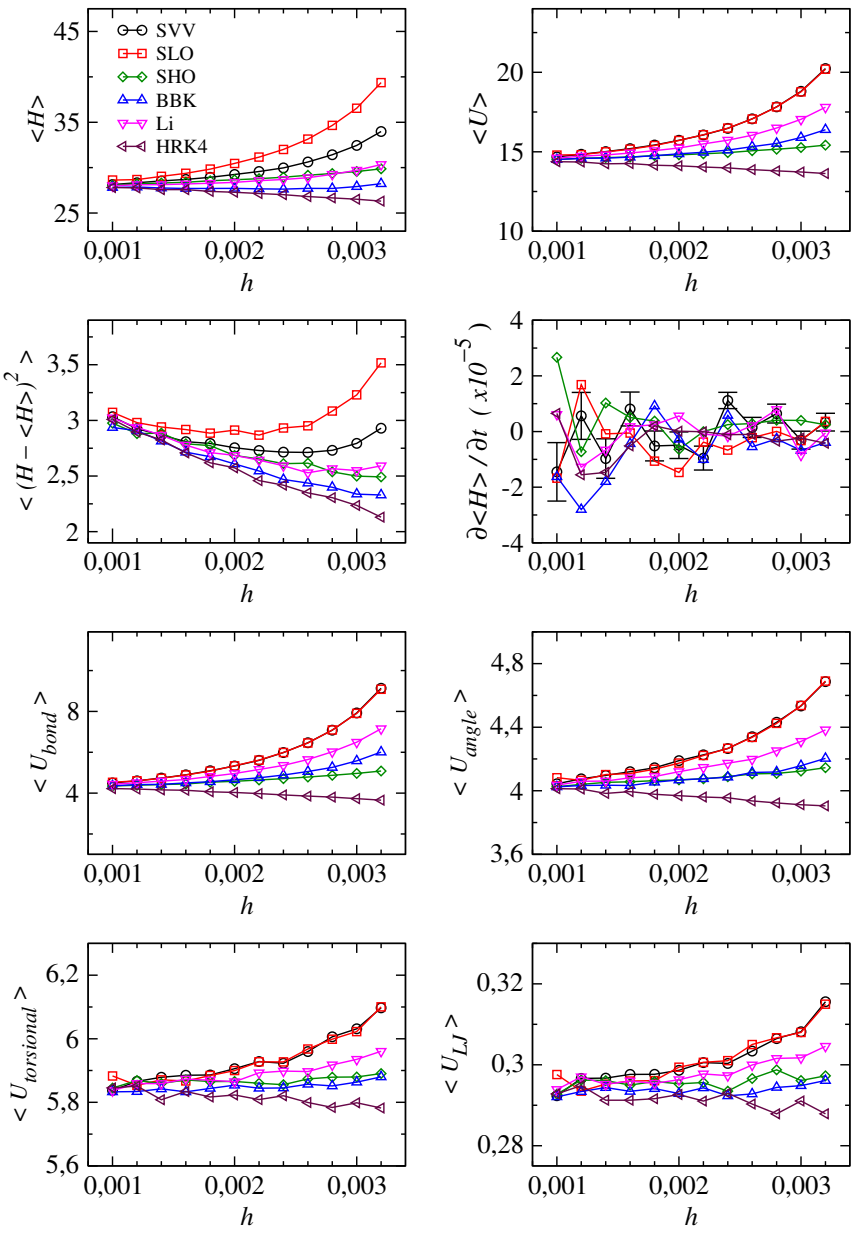

Figure 8.2: Dependence of the different energy terms on the integration step h. The quantities which are plotted are the average values per monomer of : the overall energy $< H >$, the overall potential energy $< U >$ and its different contributions, $< U_{\rm bond} >$ (Eq. 2.1) , $< U_{\rm angle} >$ (Eq. 2.2) and $< U_{\rm torsion} >$ (Eq. 2.3), as well the Lennard-Jones average energy $< U_{\rm LJ} >$ (Eq. 2.4). The total energy fluctuations and the energy drift $\partial < H > /\partial t$ were also plotted.

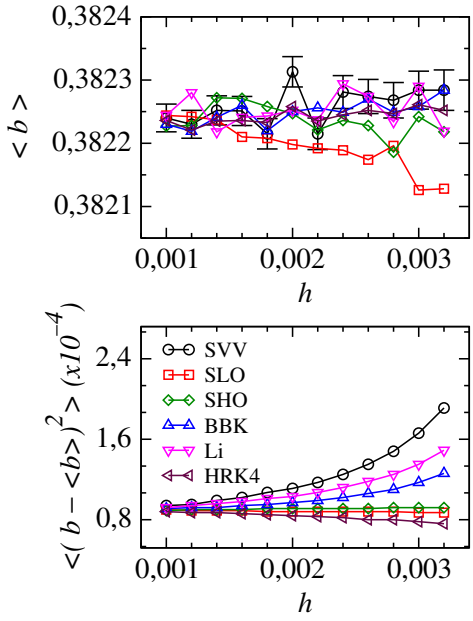

Figure 8.3: The first two moments of the bond length distribution.

8.4.2 Detailed aspects

Energy conservation

The energy conservation is an important goal in MD simulations and the symplectic algorithms are designed to achieve this target. Fig. 8.2 plots the average values of the overall energy $< H >$, the overall potential energy $< U >$ and its different contributions, $< U_{\text{bond}} >$ (Eq. 2.1), $< U_{\text{angle}} >$ (Eq. 2.2) and $< U_{\text{torsion}} >$ (Eq. 2.2), as well the Lennard-Jones average energy $< U_{\text{LJ}} >$ (Eq. 2.4). The total energy fluctuations and the energy drift $\partial < H > /\partial t$ were also plotted. Monitoring the different components of the total energy is useful in order to search the sources of instabilities since each potential term has a characteristic time scale. From this respect, Fig. 8.2 shows that the energy contributions involving faster degrees of freedom, i.e. the bond potential, are more critical.

Fig. 8.2 shows that BBK is the most accurate in its stability region ($h < 3.4 \cdot 10^{-3}$). SHO and Li have comparable performances. As we noted above, SHO is the most stable algorithm together with HRK4. However, the latter, a fourth-

order algorithm, does not perform better than the lower-order algorithms, such as BBK or SHO. It is also seen that, even if SLO and Li gets the probability distribution of the position with the same accuracy, the latter performs better. The limited accuracy of SVV is expected since it was developed for accurate evaluation of the velocity, see Sec. 8.4.2. Table 9.1 summarizes the above remarks.

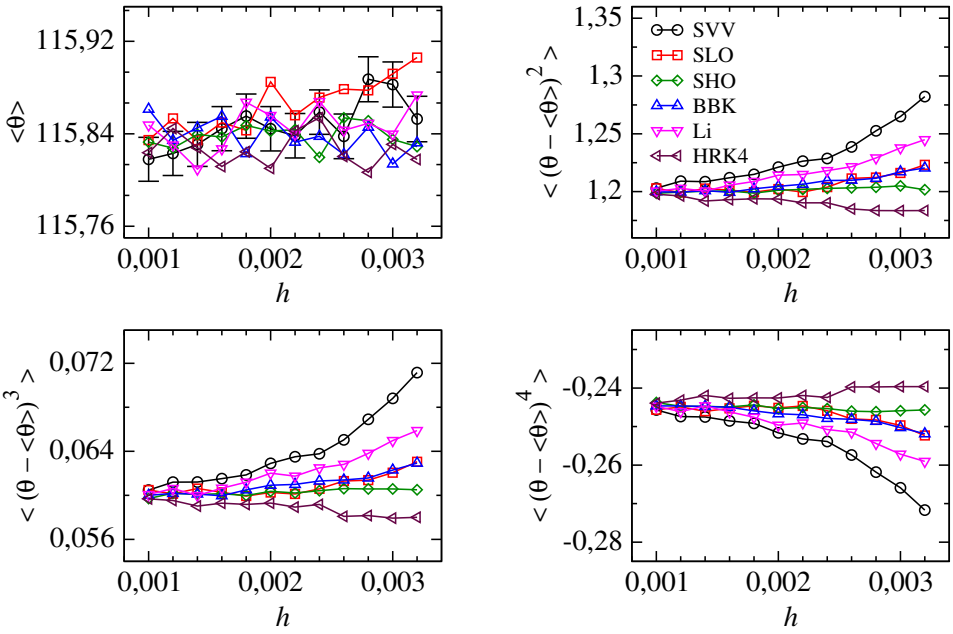

Figure 8.4: The first four moments of the bond angle distribution.

Structural properties

All the algorithms under study, apart from SVV, were designed to give accurate evaluations of the position distributions. To test the related performances, we computed the first two moments of the distribution of the bond length (Fig. 8.3), and the first four moments of the distributions of both the bond angle (Fig. 8.4) and the torsional angle (Fig. 8.5). Higher moments of the bond length distribution were found to be negligibly small. The evaluation of these structural properties evidences the better accuracy of SHO with respect to the other ones. HRK4

performs better than BBK. It must be noted that SVV and SLO, which have comparable low accuracy to evaluate both the potential energies (see fig. 8.2) and the even moments of the distribution of the torsional angle (see fig.8.5), are rather different when both the bond length (Fig. 8.3) and the bond angle (Fig. 8.4) are considered . In fact, SLO underperforms the evaluation of the average values of both quantities but it has better accuracy for their higher moments, whereas SVV behaves in the opposite way. Table 9.1 summarizes the above remarks.

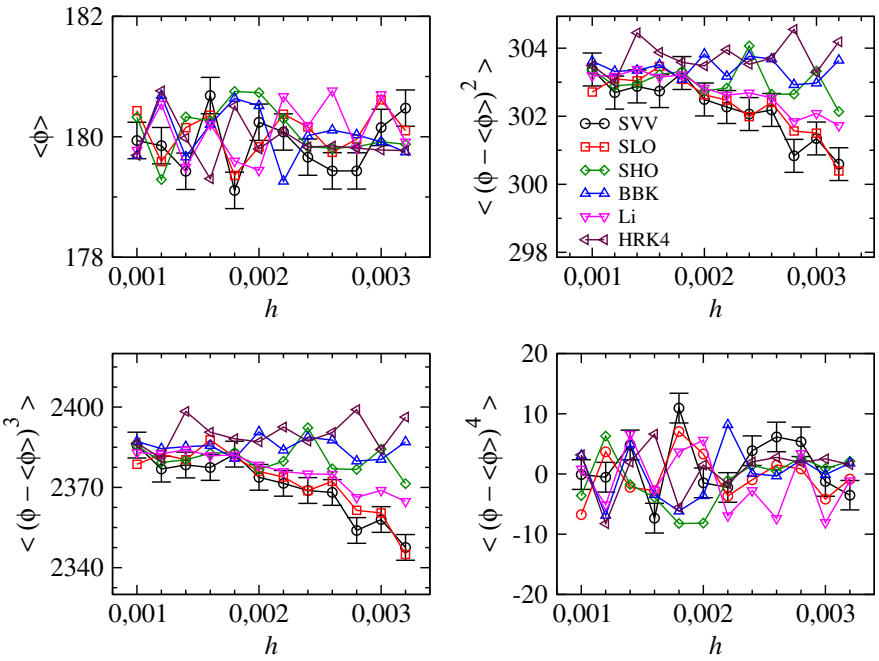

Figure 8.5: The first four moments of the torsional angle distribution.

Temperature and moments of the velocity distribution

Finally, we compared the performances of the different algorithms when they have to evaluate the molecular velocity or related quantities like the temperature. The results are presented in Fig. 8.1. The distribution of the modulus of the velocity is found to be maxwellian in shape with first and fourth moments given by [356]:

$$< v >= 2\sqrt{2T/\pi}$$

$$< v^4 >= 15T^2$$

As expected, SVV algorithm is quite accurate to evaluate both the temperature and the moments of the velocity distribution. SHO, Li and HRK4 exhibit similar accuracy. From this respect, they are better than BBK.

Table 9.1 summarizes the above remarks.

Chapter 9

Conclusions and further studies

9.1 Conclusions

Part II of this work deals with the effectiveness of employing stochastic algorithms in order to stabilise longer molecular dynamics simulations. This issue is of great importance, as can be guessed from section 7.1, where several alternative methods are presented which cope with the problem.

With this respect, we compare different algorithms to test both the accuracy, the numerical efficiency and the stability of the MD simulations of a polymer solution with long integration time steps. HRK4 and the quasi-symplectic SHO algorithm are the most stable. This feature is ensured by their greater accuracy to evaluate the position and, consequently, to follow the fast dynamics. However, the numerical efficiency is affected, especially for HRK4, by the increased number of evaluations of the forces per integration step. Differently, the popular BBK algorithm is found to be faster with limited accuracy loss but with poorer stability. The dependence of the accuracy on the quantity to be evaluated was noted. As shown by Table 9.1, the SHO algorithm exhibits better overall accuracy and stability than the other ones. As far as the computing efficiency is concerned, it also compares well with the faster (but less stable) BBK algorithm.

Table 9.1: Summary of the performances of the algorithms under study. Apart from the last three rows, the entries denote the ranks of the algorithms. The superscript denotes the sign of the positive/negative deviation from the best value. τ_X is the time needed by the X algorithm to complete one integration step. h_{max} is the integration time step above which the algorithm is unstable.

Quantity	**Algorithm**					
	SHO	BBK	HRK4	Li	SVV	SLO
$< H >$	2^+	1^+	2^-	2^+	3^+	4^+
$< U >$	1^+	2^+	2^-	3^+	4^+	4^+
$< U_{LJ} >$	1^+	1^+	2^-	2^+	3^+	3^+
bond distance	1^+	2^+	1^-	3^+	4^+	4^+
bond angle	1^+	2^+	1^-	3^+	4^+	4^+
torsional angle	1^+	1^+	2^-	2^+	3^+	3^+
velocity	2^+	3^-	2^-	2^-	1^+	4^+
τ_X/τ_{SVV}	2	1	4	1	1	1
$h_{max} \times 10^3$	6.6	3.4	4.4	3.4	3.4	3.4

9.2 Further studies

The algorithms we have just presented, have been chosen from a selection of single step methods, which come in use to perform simulation in a canonical ensemble. Considering these remarks, several proposals for further studies are brought to mind:

- Stochastic methods can be useful also when an isobaric-isothermal ensemble is required. This can be an interesting field where future tests can be performed.

- The methodology of employing symplectic schemes, can also be transferred in the field of deterministic molecular dynamics simulations in order to

speed up the simulations in NTV/NTP ensembles.

- Obviously, an extension of the above methods in case of multiple time step integrators will be valuable.

Part III

Glass transition

Chapter 10

The glass transition

Although glass is the oldest artificial material utilized by man, new discoveries and applications continue to appear. Thus the glassy state of pharmaceuticals [357]is being recognized as more effective than the crystalline form because it dissolves more quickly; the glass transition is important in providing stability to otherwise labile materials and the glass transition plays a central role in the preservation of food [358–360]. Traditional applications of glasses and glass science include, e.g., optical fibers or glass ceramics, and glass is still extensively used for windows and containers.

This chapter starts describing what we intend for glass transition; then are presented quickly the more common theories dealing with glass transition; finally we present the elastic models for glass transition, the aim of our studies.

10.1 The glass transition

A glass is formed by cooling a liquid fast enough to avoid crystallization. At continued supercooling the liquid viscosity increases dramatically, and at some point the liquid freezes continuously into a noncrystalline solid. This is termed the glass transition, although it is not a phase transition with a well-defined transition temperature T_g [361–363].

Many liquids require fast cooling to avoid crystallization, e.g., most alloys, but there are also many liquids that are easily supercooled and, in fact, difficult to crystallize, e.g., silicates and numerous organic liquids. Any liquid is able to form a glass if cooled rapidly enough. In view of this universality, the glassy state may be regarded as the fourth state of conventional matter: glass is solid as is the crystalline state, but isotropic and without long-range order as is the liquid state. This unique combination of properties explains the immense importance of glasses for a variety of applications. Indeed, it is glass' lack of long-range order, rather than the traditional properties of transparency, brittleness, and low electrical conductivity, that is the defining characteristic of this type of material [364].

10.2 Glass features

Figure 10.1(a) shows the specific volume of selenium as a function of temperature during cooling. The gradual shrinking of the liquid continues unaffected by the freezing temperature T_m. At some point the expansion coefficient, i.e. the slope of the curve, decreases to a value close to that of the crystalline state at T_g. This is the glass transition, which takes place at a slightly lower temperature if the cooling is slower. A similar observation is made for the enthalpy. Figure 10.1 (b) shows a schematic drawing of the enthalpy during cooling and subsequent reheating. The glass transition is continuous and cooling-rate dependent, and there is hysteresis upon reheating. The glass transition is similar to a second-order phase transition in the Ehrenfest sense with continuity of volume and entropy, but discontinuous changes of their derivatives [365]. But the transition is continuous and cooling-rate dependent, so it cannot be a genuine phase transition.

A system falls out of equilibrium when its relaxation time is so long that it cannot equilibrate within a given time. The relaxation time τ of a liquid was first

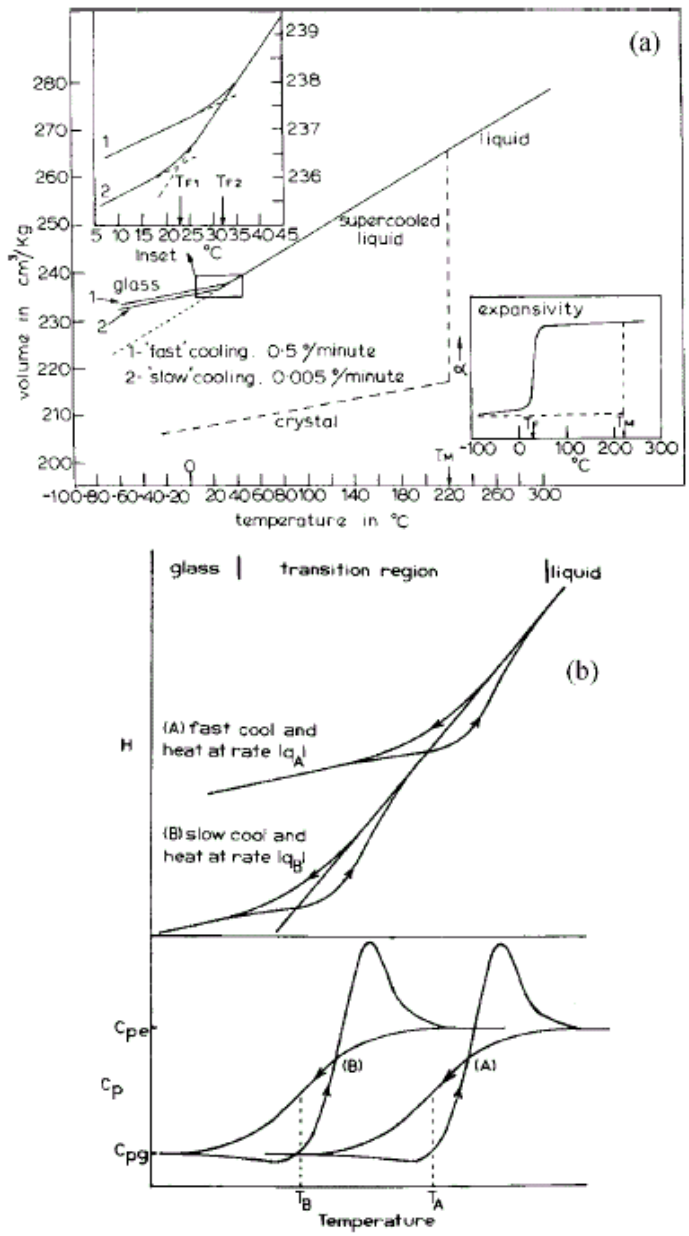

Figure 10.1: Thermodynamic characteristics of the glass transition. (a) Volume of selenium measured during cooling from liquid phase. (b) Schematic drawing of the enthalpy H and specific heat C_p by cooling from the liquid phase and subsequently reheating (selenium). [364]

identified by Maxwell in 1867 [366], and defined as

$$\tau = \frac{\eta}{G_\infty} \tag{10.1}$$

where η is the viscosity of the sample and G_∞ the instantaneous or infinite-frequency shear modulus; it has to be noted that τ and η are roughly proportional since G_∞ is much less temperature dependent than η or τ. It is a general property of Eq. 10.1 that the liquid is solid-like on time scales much shorter than τ; generic liquid behavior is only predicted on time scales much longer than τ. The Maxwell relaxation time τ provides the key to understanding the glass transition. Typical values of G_∞ are in the $10^9 - 10^{10}$ Pa s range, so since $\eta \sim 10^{12}$ Pa s at the glass transition, τ is here of order 100-1000 s. Thus the glass transition takes place when the Maxwell relaxation time becomes comparable to the cooling time.

The Maxwell relaxation time not only determines how fast a macroscopic stress relaxes. Numerous experiments show that τ also determines the typical time between molecular displacements or reorientations. This confirms that the glass transition takes place when the liquid is unable to equilibrate on the experimental time scale, i.e., when some process in the amorphous material occurs too slowly at low temperatures to permit thermodynamic equilibrium to be established in all degrees of freedom [364, 367].

What happens at the glass transition is that molecular motion virtually ceases (and so any structural relaxation), except for thermal vibrations[364]; however, some vacancy-driven diffusion can still be found, in the same manner as it occurs, at finite temperature, in a crystalline solid phase [368, 369]. This explains several observations:

- The ability to form glasses is universal and not a specific atomic or molecular property; once the extremely viscous liquid state has been arrived at, glass formation is unavoidable upon continued cooling.

- Volume, enthalpy, and entropy are continuous across the glass transition, and no changes of the molecular structure are observed at T_g. It must be

pointed out that as the equilibrium cannot be reached within the experimental time-scale, these quantities are not well defined in the thermodynamic sense, and depends on the sample's history. The non-ergodic thermodynamics can still be defined on a restricted ensemble [370, 371].

- The glass expansion coefficient and specific heat are lower than those of the liquid: this is because below T_g molecular reorientations and effective motions cease to contribute to these quantities.

- T_g is lower when the cooling rate is reduced in fact T_g has no exact definition, even for a given cooling rate.

- Hysteresis effects are inherently associated with the glass transition; these derive from the fact that upon reheating the structure relaxes slightly before T_g is reached.

Glasses may form from all liquids, however, with liquid helium as the outstanding exception. A good *glass former* is a liquid which is readily supercooled, i.e., characterized by very low rates of crystal nucleation and growth at all temperatures [372, 373].

The glassy state has several challenging questions which need an answer; however, here we address our attention only toward that aspects relevant for our studies. In literature good reviews can be found, such as refs. [374–377].

10.3 Non-Arrhenius behaviour

A fingerprint of the glassy state is the non-Arrhenius temperature dependence of the Maxwell *alpha* relaxation time τ or viscosity η (eq. 10.1).

Figure 10.2 is the original *Angell plot* [378] showing the logarithm of the viscosity for a number of viscous liquids as a function of inverse temperature normalized to unity at T_g, where T_g is defined as the temperature at which the

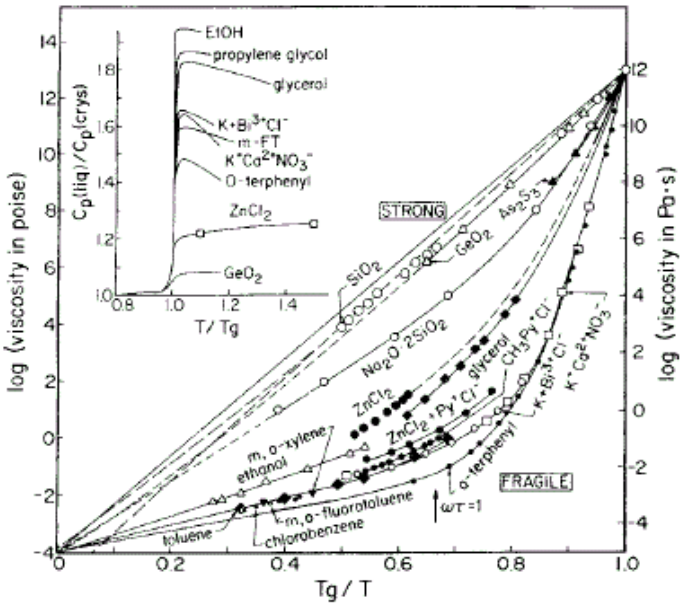

Figure 10.2: The Angell fragility plot showing the viscosity as a function of inverse temperature normalized to 1 at T_g. The lower left corner marks the approximate high-temperature limit of the viscosity that is common to all liquids. An Arrhenius viscosity gives a straight line in this plot. Inset: Specific-heat jumps at the glass transition. [378]

equilibrium liquid viscosity is 10^{12} Pa s. If, as is generally assumed, dynamics are dominated by barriers to be overcome by thermal fluctuations, one would expect $\eta \sim \exp(\Delta E/k_B T)$ [379], corresponding to the diagonal line. This is referred to as an Arrhenius temperature dependence, after Arrhenius [380] who discovered that chemical reaction times usually follow this law. The Arrhenius law, however, only works for a few liquids, e.g., pure silica SiO_2 or phosphor pentoxide P_2O_5 [381]. In the vast majority of cases viscous liquids show a stronger than Arrhenius increase of the viscosity upon cooling toward the glass transition. If one nevertheless accepts the Arrhenius expression, the activation energy must be temperature dependent: $\Delta E(T)$ is defined by(where $\tau_0 \sim 10^{13}$ s is a typical microscopic time)

$$\tau = \tau_0 \exp\left(\frac{\Delta E(T)}{k_B T}\right) \tag{10.2}$$

More correctly ΔE defines the free energy of activation, but for simplicity we

use the traditional term activation energy. The message of Fig. 10.2 is that the activation energy increases when temperature decreases. There seem to be no examples of viscous liquids with an activation energy that decreases upon cooling.

For some viscous liquids τ increases by more than one order of magnitude when the temperature is lowered by just 1%. Such strongly non-Arrhenius liquids are called *fragile* (no connection to glass fragility), while those closer to Arrhenius behavior are termed *strong* [378]. Non-Arrhenius data are often fitted by the so-called Vogel-Fulcher-Tammann expression [382–384]

$$\tau = \tau_0 \exp\left(\frac{A}{T - T_0}\right) \tag{10.3}$$

Equation 10.3 implies that the liquid's equilibrium relaxation time becomes infinite at T_0, a prediction that cannot be verified because, if correct, the system is bound to fall out of equilibrium as T_0 is approached. Equation 10.3 has inspired leading theorists to speculate on its origin[385]. Stillinger [386] argued that a liquid cannot have an infinite relaxation time at a finite temperature. When compared to experiment, eq. 10.3 generally breaks down in the highly viscous regime by predicting too large relaxation times [361, 372, 387–389]. An alternative fit to data with the same number of parameters is provided by [390–393]:

$$\tau = \tau_0 \exp\left(\frac{C}{T^n}\right) \tag{10.4}$$

The traditional measure of non-Arrhenius behavior is the *fragility* m defined [394–396] by

$$m = \left.\frac{d \log_{10} \tau}{d(T_g/T)}\right|_{T_g} \tag{10.5}$$

10.4 Models of the glass transition

All molecules of a viscous liquid have the thermal velocities prescribed by the canonical ensemble, but virtually all motion goes into vibrations. Thus it has been suggested that a viscous liquid is to be regarded more as "a solid that

flows" than as a conventional liquid [397–399]. This is consistent with the long-standing assumption that viscous-liquid thermodynamics may be separated into a vibrational and a configurational part. The dynamics also separates into vibrations on the short time scale and *inherent dynamics*, i.e., jumps between potential energy minima on the long time scale [208, 248, 400, 401].

Up to date several theories have been put forward in order to tackle the problem of glass transition. The most important are the **Adams-Gibbs theory** [402–404], which states that the long relaxation times at low temperatures are brought about by a dearth of configurations and the **free volume models** [405, 406], which assert that molecules need "free" volume in order to be able to rearrange; as the liquid contracts upon cooling, less free volume becomes available.

In the literature other interesting models have been proposed, such as the **mode coupling theory** [407–409]; a quick review can be found in [364] and reference therein.

In this work we are not interested in exploring the features of the different theories. We concentrate our attention on what is commonly called *harmonic approximation*; but this is the subject of the chapter 12.

Chapter 11

Simulation details

In this chapter we describe the model employed in order to perform a molecular dynamic simulation of a melt of polymer chains. Again we employed a bead spring model: in this model we lose the atomistic details of the molecules, preserving only the connectivity and the excluded volume effect; each monomer of the chain is mimicked by a bead, see chapter 2 for further details.

11.1 Force field

A coarse-grained model of a linear polymer chain is used. Torsional potentials are neglected. Each monomer is pictured as a soft sphere interacting via a suitable pair potential with the other non-bonded monomers. Bonded monomers interact with a potential which is the sum of the FENE (Finitely Extendible Nonlinear Elastic) potential and the Lennard-Jones potential [12, 302]:

$$U_{\mathrm{LJ}}(r) = \epsilon \left[\left(\frac{\sigma^*}{r} \right)^{12} - 2 \left(\frac{\sigma^*}{r} \right)^{6} \right] \tag{11.1}$$

$$U_{\mathrm{FENE}}(r) = -\frac{1}{2} k R_0^2 \ln \left[1 - \left(\frac{r}{R_0} \right)^2 \right], \quad R_0 = 1.5\sigma, \quad k = \frac{30\epsilon}{\sigma^2} \tag{11.2}$$

where r is the monomer-monomer distance and $\sigma^* = 2^{1/6}\sigma$. With the above parameters the bond length is $b = 0.97\sigma$ within few percent.

Non-bonded monomers interact via a truncated parametric Lennard-Jones potential [422]:

$$U_{p,q}(r) = \begin{cases} \frac{\epsilon}{q-p}\left[p\left(\frac{\sigma^*}{r}\right)^q - q\left(\frac{\sigma^*}{r}\right)^p\right] + U_{cut} & r \leqslant r_c \\ \\ 0 & \text{Otherwise} \end{cases} \tag{11.3}$$

where the value of the constant U_{cut} is chosen to ensure $U_{p,q}(r_c) = 0$ at $r = r_c = 2.5\sigma$. The minimum of the potential $U_{p,q}(r)$ is at $r = \sigma^*$, with a constant depth $U(r = \sigma^*) = \epsilon$. We set $\sigma = 1, \epsilon = 1$. The time unit is $\tau_{MD} = (m\sigma^2/\epsilon)^{1/2}$, with m being the mass of the monomer. Temperature is in units of ϵ/k_B, where k_B is the Boltzmann constant. We set $m = k_B = 1$.

11.2 Statistical ensembles

The simulations were performed using three distinct ensembles: isothermal-isobaric ensemble (NPT), canonical ensemble (NTV) and microcanonical ensemble (NVE) [126]. NPT and NTV ensembles have been used for equilibration runs while NVE ensemble has been used for production runs.

11.2.1 NVE ensemble

In this ensemble the system evolves under its internal forces, without any interaction with the surrounding environment (as it happens in NTV and NPT ensembles revised later). The Hamiltonian of the system reads:

$$H = \sum_{i=1}^{N} \frac{P_i^2}{2m_i} + U(Q) \tag{11.4}$$

where N is the number (constant) of interacting particles in the system, m_i the mass of the i-th monomer; P and Q being conjugate momenta. From the

Hamiltonian H follows the equations of motion:

$$\dot{Q}_i = \frac{\dot{P}_i}{m_i} \tag{11.5}$$

$$\dot{P}_i = -\nabla_Q U(Q) \tag{11.6}$$

where $\dot{Q}$ and $\dot{P}$ signify the time derivative of positions and momenta.

11.2.2 NTV ensemble

In order to simulate a constant temperature system, the Hamiltonian H which describes the dynamics of the particles, is augmented by adding and extra term which accounts for a thermal piston. For this reason the system gain an extra degree of freedom. The extended Hamiltonian is:

$$H_{NTV} = \sum_{i=1}^{N} \frac{P_i^2}{2m_i} + U(Q) + \frac{\pi_s^2}{Q_s} + g k_B T \ln s \tag{11.7}$$

where π_s is the extra degree of freedom which account for the thermal piston, Q_s is its thermal inertia (which works as a mass), and g is the total number of degrees of freedom of the system. Again we can derive the equation of motion [426]:

$$\dot{Q}_i = \frac{\dot{P}_i}{m_i} \tag{11.8}$$

$$\dot{P}_i = -\nabla_Q U(Q) - P_i \xi \tag{11.9}$$

$$\dot{\eta} = \xi \tag{11.10}$$

$$\dot{\xi} = \frac{1}{Q_s}\left(\sum_{i=1}^{N} \frac{P_i^2}{m_i} - (g-1)k_B T\right) \tag{11.11}$$

where $\xi = \pi_s / Q_s$ and $\eta = \ln s$

11.2.3 NPT ensemble

For isobaric-isothermal system is used the technique of the extended Hamiltonian, which now reads:

$$H_{NPT} = \sum_{i=1}^{N} \frac{P_i^2}{2m_i} + U(Q) + \frac{\pi_s^2}{2Q_s} + g k_B T \zeta + \frac{\pi_V^2}{2Q_V} + P_{ext} V \tag{11.12}$$

The new variables π_V and Q_V account for the dynamics of the pressure piston, in the same way as the thermal piston met in the NTV ensemble. P_{ext} is the external pressure applied on the system, and V the varying volume of the system. Now the equation of motion can be written down as[128, 427]:

$$\dot{Q}_i = \frac{\dot{P}_i}{m_i} + \frac{\pi_V}{Q_V} Q \tag{11.13}$$

$$\dot{P}_i = -\nabla_Q U(Q) - P_i \frac{\pi_s}{Q_s} - \left(1 + \frac{3}{g-1}\right) \frac{\pi_V}{Q_V} P_i \tag{11.14}$$

$$\dot{V} = 3V \frac{\pi_V}{Q_V} \tag{11.15}$$

$$\dot{\pi}_V = 3V(P_{int} - P_{ext}) + \frac{3}{g-1} \sum_{i=1}^{N} \frac{P_i^2}{m_i} - \pi_V \frac{\pi_s}{Q_s} \tag{11.16}$$

$$\dot{\zeta} = \frac{\pi_s}{Q_s} \tag{11.17}$$

$$\dot{\pi}_s = \sum_{i=1}^{N} \frac{P_i^2}{m_i} + \frac{\pi_V^2}{Q_V} - g k_B T \tag{11.18}$$

and

$$P_{int} = \frac{1}{3V} \left[\sum_{i=1}^{N} \left(\frac{P_i^2}{m_i} - Q_i \cdot \nabla_Q U(Q) \right) \right]$$

11.3 Algorithm

NPT and NTV ensembles have been simulated with the extended system method introduced by Andersen [428] and Nosé [429]. Within this approach, additional degrees of freedom are added to the Hamiltonian of the system, to be interpreted as the degrees of freedom associated to the thermal piston and the mechanical one. The numerical integration of the augmented Hamiltonian has been performed through the reversible multiple time steps algorithm (i.e. the r-RESPA algorithm) developed by Tuckerman *et al.*[334]. In particular, the NPT and NTV Liouville operators corresponding to the aforementioned extended Hamiltonian have been factorized using the Trotter theorem [331] separating the short range and long range contributions of the potential $U_{p,q}(r)$, Eq. 11.3, according to the WCA

decomposition [430]. The simulations have a drift of the total energy less than $\sim 5 \cdot 10^{-8}\epsilon/\tau_{MD}$ and a standard deviation of the total energy less than $2 \cdot 10^{-4}$ with an integration time step $3 \cdot 10^{-3}\tau_{MD}$. The latter was kept constant in all the production runs to limit systematic errors. To speed-up the simulations, we exploited the neighbour lists method and, to reduce the finite-size effects, periodic boundary conditions have been used.

11.4 Simulation protocol

In this section the simulation protocol is described. Each state point (labelled by the multiplets $\{T, \rho, M, p, q\}$) has been obtained through four stages:

1. Placement of the chains in a regular lattice preventing monomer-monomer overlap.

2. NPT-ensemble simulation to get the number density of interest ρ.

3. NTV-ensemble equilibration of the system. The equilibration time is ten times longer than the longest relaxation time, i.e. the time needed by the end-to-end correlation function to decay to less than 0.1 times its initial value.

4. NVE-ensemble production run.

11.5 Data set

We investigated 121 independent states. Both the temperature T, the number density ρ, the monomers per chain M and the parameters p, q in the force field, eq. 11.3, are changed. $\rho = N/V$ where N is the total number of monomers, and V is the volume of the cubic box. $N = 2000$ in all cases but $M = 3$ where $N = 2001$. For each case averages on at least five independent configurations are

performed. For $M = 10$ the least number of independent configurations is ten. Below, the different state points are listed. In addition to the systematic scan of some parameters, other cases were added to ensure the optimum definition of the master curve plotted in Fig. 12.3.

$T = 0.7$:

- $p = 6$. All the combinations with $M = 2, 3, 5, 10$, $\rho = 1.033, 1.056, 1.086$ and $q = 7, 8, 10, 12$. The case $M = 2, \rho = 1.086, q = 12$ equilibrates very slowly and was discarded.

- $p = 6, M = 3$. The pairs (ρ, q): (1.090,12), (1.033,11), (1.039,11), (1.041,11), (1.045,11), (1.051,11), (1.056,11), (1.086,11), (1.033,9), (1.056,9), (1.063,9), (1.071,9), (1.079,9), (1.086,9).

- $p = 5, q = 8$. All the combinations with $M = 2, 3, 5, 10$ and $\rho = 1.133, 1.156, 1.186, 1.2$. Furthermore, $M = 2$, $\rho = 1.033$.

- $p = 11, q = 12, M = 2$ with densities $\rho = 0.980, 0.990, 1.0$.

$T \neq 0.7, p = 6$:

- $T = 0.5$, $\rho = 1.033$, All the combinations with: $M = 2, 3, 5, 10$, $q = 7, 8, 10$.

- $T = 0.6$, $\rho = 1.033$, All the combinations with: $M = 2, 3, 5, 10$, $q = 8, 10$.

- $q = 12$, $\rho = 1.033$, the pairs (M, T): (2,0.5), (3,0.5), (2,0.55), (3,0.55), (2,0.6), (3,0.6), (5,0.6), (3,0.65), (5,0.65), (10,0.65).

- $q = 12$, $\rho = 1.086$, the pairs (M, T): (2,0.75), (3,0.75), (5,0.75), (10,0.75), (2,0.8), (3,0.8), (5,0.8).

- $q = 12, \rho = 1.090, M = 3$, with $T = 0.75, 0.8$.

Finally, $p = 5, q = 8, M = 2, \rho = 1.033, T = 0.5$.

11.5.1 Data sets of Fig. 12.2

What follows is a list of the data represented in Fig. 12.2 (multiplets (M, ρ, T, q, p)):

- Set A (blue): (2,1.086,0.7,7,6), (3,1.086,0.7,7,6), (10,1.086,0.7,7,6), (10,1.033,0.7,8,6)
- Set B (black): (2,1.033,0.7,10,6), (3,1.039,0.7,11,6), (3,1.041,0.7,11,6)
- Set C (red): (2,1.033,0.5,10,6), (3,1.056,0.7,12,6), (5,1.033,0.6,12,6), (10,1.056,0.7,12,6)
- Set D (green): (3,1.086,0.7,12,6), (5,1.086,0.7,12,6), (10,1.086,0.7,12,6)
- Set E:(2,1.0,0.7,12,11)

These data are presented here, instead that in chapter 12, in order not to interrupt the discussion there reported.

Chapter 12

The glimpse of an universal scaling

This chapter is devoted to the presentation of the original results achieved during this work concerning the glass transition. At the beginning an overview of the harmonic approximation is given; this section is then followed by the data obtained by molecular dynamic simulation in order to assess the validity of the harmonic approximation. A final comparison with experimental data closes this chapter.

12.1 Harmonic approximation

The first paper suggesting that the activation energy is determined by short-time elastic properties appears to be the work by Tobolsky, Powell and Eyring [410] basically arguing as follows. The viscosity is determined by the rate of molecules moving from one equilibrium position (energy minimum) to another. In the schematic situations of fig. 12.1 the energy barrier to be overcome is clearly overestimated by the intersection of the parabolic extrapolations from the minima. Comparing the situations of figs. 12.1a and 12.1b, however, the barrier is overestimated by the same numerical factor. Thus the estimated barrier is pro-

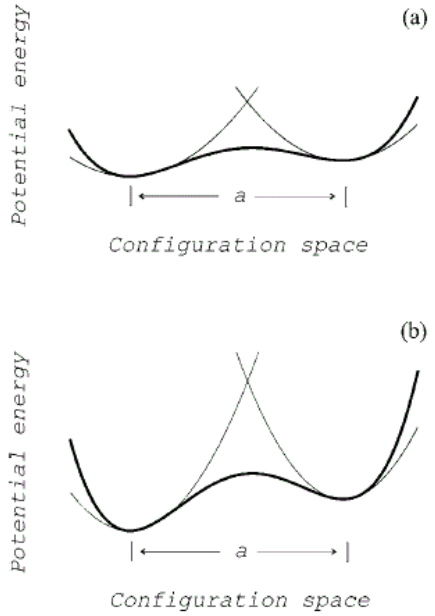

Figure 12.1: Comparing two cases of potential energy minima with different curvatures at the minima. The full curve is the potential energy; the thin curve gives the potential estimated by second-order Taylor expansions around the minima. The barriers estimated from the intersection of thin curves are considerably larger than the actual barriers; however, going from (a) to (b) the estimated and actual barriers are proportional [364]

portional to the actual barrier (a only changes insignificantly). According to rate theory [411] the average time between jumps τ is a microscopic time τ_0 divided by the statistical mechanical probability to find the system around the energy maximum. In the harmonic approximation the energy is quadratic in the reaction coordinate; this leads to a Gaussian statistical-mechanical probability distribution $\propto \exp(-x^2/2 < x^2 >)$, where x is the reaction coordinate deviation from its value at the minimum and $< x^2 >$ is the vibrational mean-square thermal average around one minimum. Thus for some numerical factor of order one λ_1, if a is the average intermolecular distance, the harmonic approximation leads to

$$\tau = \tau_0 \exp\left(\lambda_1 \frac{a^2}{< x^2 >}\right) \tag{12.1}$$

Using eq. 10.2 the activation energy is given by

$$\Delta E = \lambda_1 k_B T \frac{a^2}{< x^2 >} \tag{12.2}$$

The vibrational mean-square displacement $< x^2 >$ depends on temperature. For a harmonic, temperature independent system the intermolecular potential

is parabolic and classical equipartition implies that $x^2 \propto T$, so ΔE is temperature independent. For most glass-forming liquids $< x^2 >$ decreases faster than T upon cooling, resulting in an activation energy that increases upon cooling. During the last 20 years eq. 12.1 or related expressions were derived and discussed by a number of authors in different contexts of viscous liquid dynamics [412, 413, 417–423]. Eq. 12.1 has also been used for diffusion in crystals [424, 425].

12.2 Universal scaling between structural relaxation and vibrational dynamics

When liquids, polymers, bio-materials, metals and molten salts are cooled, if the crystallization is avoided, they freeze to a microscopically disordered solid-like state, a glass [221, 372]. As the glass transition temperature T_g is approached from above, the kinetic unit spends an increasing fraction of time rattling on picosecond time scales into the cage of the first neighbours. To escape, the unit must await an average lapse of time τ_α, the so called "structural relaxation time", which, on approaching T_g, increases from a few picoseconds up to thousands of seconds. In spite of that huge time scale separation old [410, 431, 432] and recent theoretical [372, 412, 423, 433–435], experimental [413, 436–438] and numerical [421, 422, 439] studies suspected correlations between the rattling process and the relaxation.

The solid state of matter is characterized by well-defined elastic properties settled by the interatomic potentials driving at a microscopic level the oscillatory motion of the atoms with mean square amplitude $< u^2 >$ around their equilibrium positions (henceforth to be referred to as the Debye-Waller (DW) factor). On increasing the temperature, depending on the structural degree of order, solids meet different fates. In crystalline solids the ordered structure melts at T_m, whereas in amorphous solids the disordered structure softens at the glass transition tem-

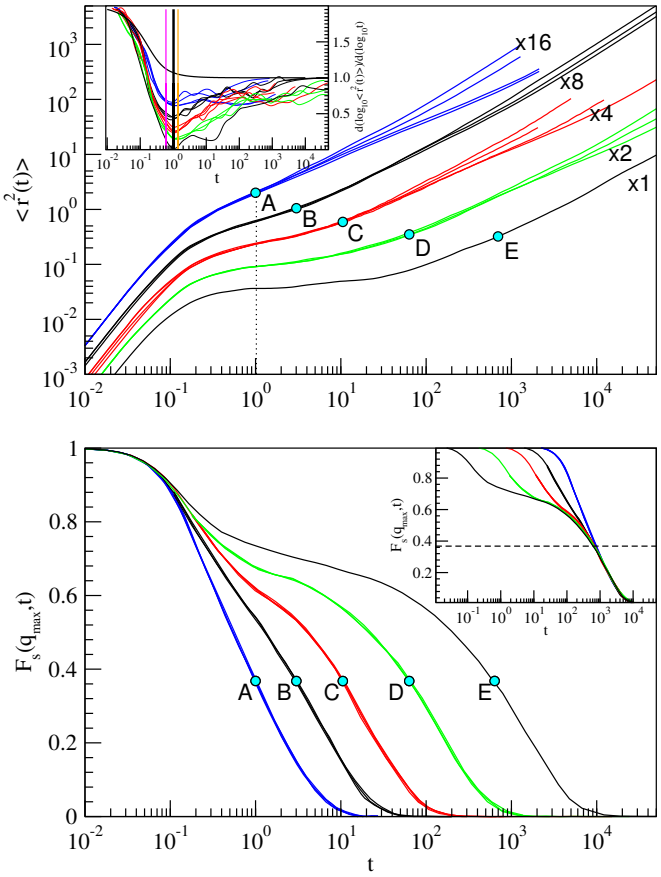

Figure 12.2: MD simulations of a polymer melt by the bead-spring FENE model [15]. The structural relaxation time τ_α is marked with a large dot on each curve. Top: time-dependence of the monomer mean squared displacement $< r^2(t) >$ in selected cases. To improve the readability curves are multiplied by constant factors. Inset: the time when the system leaves the balistic regime and meets the cage, is defined as the appeareance of a discontinuity in the slope; three values of the time have been chosen. Bottom: corresponding ISF $F_s(q_{max}, t)$. Non-trivial sets of potential parameters, density, temperature and chain length lead to clusters of sumperimposable MSD and ISF curves. As an example four different clusters are shown. The superimposability breaks down for $t > \tau_\alpha$ and at short times in the ballistic regime, i.e. $t \lesssim 0.1$. If the cluster groups cases has the same temperature, the superimposability extends at shorter times. Inset: superimposability of the shifted ISF; the horizontal line is drawn at e^{-1}.

perature T_g above which viscous flow occurs. Elasticity seems to be involved in both phenomena. This motivated extensions to glasses of the Lindemann criterion for crystalline solids [440]. In addition, approaches linking the elastic properties of amorphous solids with the viscous flow observed above T_g [410, 431–434] are paralleled by results reporting [422, 435–439], or denying [441], correlations between the fragility (an index of how fast the viscosity η or τ_α increase *close* to T_g [372]) and the elastic/vibrational properties. On the other hand, the old models [410, 432] correlated η or τ_α to the instantaneous shear modulus G_∞, at *any* temperature above T_g. More recently, this viewpoint has been considered by picturing the glass transition as a freezing in an aperiodic crystal structure (ACS) [412]. There, the viscous flow is originated by activated jumps over free-energy barriers $\Delta E \propto k_B T a^2 / < u^2 >$ where a is the displacement to reach the transition state ($a^2 \propto N_m (\delta\Delta)^2$, with N_m and $(\delta\Delta)^2$ being the number of particles that move and their mean squared displacement, respectively) and k_B the Boltzmann constant. The usual rate theory leads to [412, 434]:

$$\tau_\alpha, \eta \propto \exp\left(\frac{a^2}{2 < u^2 >}\right) \tag{12.3}$$

Tests of Eq. 12.3 were carried out in several systems [413–416]. However, either the crystal or the glass contributions after extrapolation in the liquid regime are usually subtracted from $< u^2 >$. In selenium, if $< u^2 >$ is used, *log* η vs. $1/ < u^2 >$ is concave, whereas if the glass or the crystal contribution are removed, a convex curve or a straight line, the latter agreeing with Eq.12.3, are seen, respectively [413]. The fact that many glass-formers have no underlying crystalline phases, as well as the fact that in many studies removing the glass contribution, differently from Se, leads to Eq. 12.3, raises some ambiguities about the above subtractions. The ACS model is expected to fail when τ_α becomes comparable to the typical rattling times of each atom in the cage of the surrounding atoms. That condition is quite mild, e.g. in Se it occurs at $T_m + 104K$ corresponding to picosecond timescales [413]. It seems natural to generalize Eq.12.3 by adopting

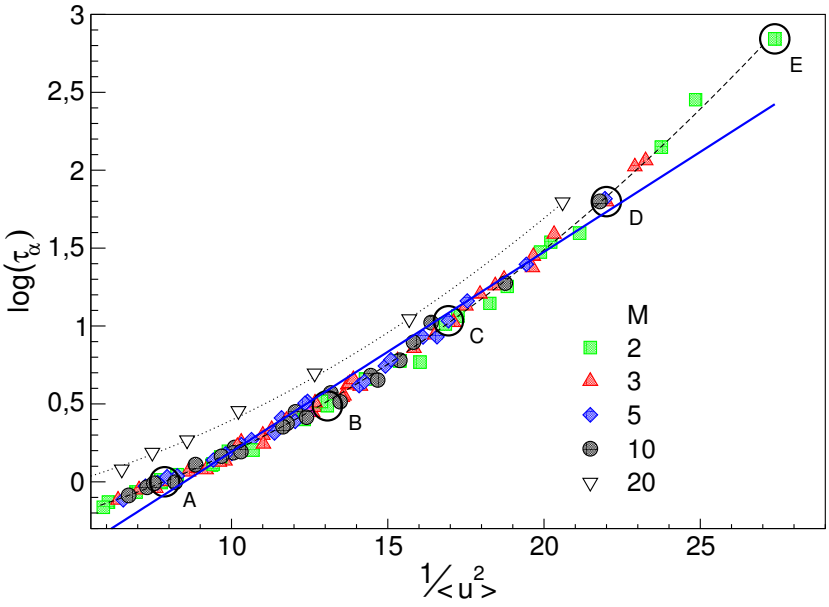

Figure 12.3: The structural relaxation time τ_α vs the DW factor $< u^2 > \equiv < r^2(t = 1.022) >$. Circles identify the cases plotted in Fig.12.2. The superimposed curve is Eq. 12.4 $log_{10}\tau_\alpha = \alpha + \beta < u^2 >^{-1} + \gamma < u^2 >^{-2}$ with $\alpha = -0.424(1), \beta = \overline{a^2}/2\ln 10 = 2.7(1) \cdot 10^{-2}, \gamma = \sigma^2_{a^2}/8\ln 10 = 3.41(3) \cdot 10^{-3}$. MD results on the collective relaxation time τ of a polymer melt with $M = 20$ from [421]. The dotted curve is obtained by shifting vertically the best-fit curve of τ_α with $\alpha' = \alpha + 0.205(5), \beta' = \beta, \gamma' = \gamma$. The straight line represents the best fit using eq. 12.3

a suitable distribution $p(a^2)$ of the squared displacement to reach the transition state. In particular, averaging Eq.12.3 over $p(a^2) \propto exp[-(a^2 - \overline{a^2})^2/2\sigma^2_{a^2}]$ leads to:

$$\tau_\alpha, \eta \propto \exp\left(\frac{\overline{a^2}}{2 < u^2 >} + \frac{\sigma^2_{a^2}}{8 < u^2 >^2}\right) \tag{12.4}$$

Eq.12.4 yields the leading dependence on $< u^2 >$ even if the gaussian is truncated below $a_c \geq 0$ to account for e.g. a minimum number of particles that move and/or a minimum mean squared displacement. Beyond the Central Limit Theorem, other motivations support the gaussian form of $p(a^2)$. If the kinetic unit is undergoing a harmonic motion due to an effective spring with constant k, $< u^2 > \propto k_B T/k$ and Eq.12.4 reduces to a form already reported for both supercooled liquids [392] and polymers [442], and predicted by a coarse-grained model

of glass formers [443]. Furthermore, along the same line of reasoning, one may reinterpret the gaussian form of $p(a^2)$ as a gaussian form of the energy barriers $\Delta E \propto ka^2$ which has been assumed by the trap model [444] and others [445]. Evidence will be given that the dependence of the structural relaxation time on the DW factor collapses on a universal master curve provided by Eq.12.4. We devised a two-step strategy. First, a master curve is built by resorting to extensive Molecular-Dynamics (MD) numerical simulations of a polymer melt by changing the temperature T, the density ρ, the interatomic potential and the connectivity of the system (all these parameters but T affect the fragility of the system [422, 437, 439, 446]). Then, motivated by the Lindemann criterion [440, 447, 448], a suitable scaling of both the numerical and experimental data is introduced to convert the MD master curve into the universal one, including both strong and fragile glasses [372] and polymers, the latter considered less by other studies[436–438, 441].

12.2.1 Simulations

Let us discuss the MD simulations. To characterize the short-time dynamics and the structural relaxation we use the monomer mean squared displacement $< r^2(t) >$ (MSD, $< r^2(t) >= N^{-1} < \sum_{j=1}^{N_m} [\boldsymbol{r}_j(t) - \boldsymbol{r}_j(0)]^2 >$ where the sum runs over the total number of N monomers and the brackets denote a suitable ensemble average) and the incoherent intermediate scattering function $F_s(q_{max}, t)$ (ISF, $F_s(q,t) = N_m^{-1} < \sum_{j=1}^{N_m} exp\{-i\boldsymbol{q} \cdot [\boldsymbol{r}_j(t) - \boldsymbol{r}_j(0)]\} >$), q_{max} being the q-vector of the maximum of the static structure factor. Fig. 12.2 shows typical MSD and ISF curves. At short times MSD increases according to $< r^2(t) > \cong 3\upsilon^2 t^2 - \upsilon^2 \Omega_0^2 t^4/4$ where $\upsilon = \sqrt{k_B T/m}$ is the thermal velocity. Correspondingly, ISF initially decays as $F_s(q,t) \cong 1 - \Omega_q^2 t^2/2 + (3\Omega_q^4 + \Omega_q^2 \Omega_0^2) t^4/24$ with $\Omega_q = q\upsilon$ [449]. Ω_0 is an effective frequency of collisions , i.e. the frequency at which the tagged monomer would vibrate if it were undergoing small oscillations in the potential

well produced by the the other surrounding monomers when kept at their mean equilibrium positions [449]. In Fig.12.2 $2\pi/\Omega_0$ is located close to the time $t \sim 0.1$ when MSD starts to deviate from the ballistic regime $< r^2(t) > \cong 3v^2t^2$. At longer times, after a knee, MSD exhibits a quasi-plateau region, also apparent in ISF, which is more apparent when the temperature is lowered and/or the density increases evidencing the increasing caging of the monomer. On average, the latter escapes after a time τ_α (defined by the relation $F_s(q_{max}, \tau_\alpha) = e^{-1}$). For $t > \tau_\alpha$ MSD increases more steeply. The monomers of short chains ($M \lesssim 3$) undergo diffusive motion $< r^2(t) > \propto t^\delta$ with $\delta = 1$. For longer chains, owing to the increased connectivity, the onset of the diffusion is preceded by a subdiffusive region ($\delta < 1$, Rouse regime) [51]. The dynamics of the model polymer depends in a non trivial way upon the temperature T, the densityρ, the chain length M and the interaction potential $U_{p,q}(r)$. Nonetheless, Fig.12.2 (top) shows that cases (labelled by multiplets $\{T, \rho, M, p, q\}$) exist which exhibit nearly perfect superimposability of MSD curves from times being a little bit longer than $2\pi/\Omega \simeq 0.1$ up to times longer than τ_α (if the cluster groups cases with equal temperature, the superimposability extends at shorter times). Notably, in the same time window the corresponding ISF curves superimpose as well (Fig.12.2, bottom). The finding suggests that, after few collisions with frequency Ω_0, a correlation between the structural relaxation and the fast dynamics sets in. To better evidence the correlation, a proper definition of the DW factor $< u^2 >$ is needed. Notice that Eq.12.3 was derived under the ansatz that the motion of the atoms crossing the energy barriers is virtually unidirectional [412]. That picture relies on the fact that the atomic MSD during the structural relaxation is less than one atomic radius. Indeed, Fig.12.2 shows that $< r^2(t = \tau_\alpha) >^{1/2} \lesssim \sigma/2$. The ansatz suggests to identify $< u^2 >$ with $< r^2(\tau_v) >$, τ_v being the time needed by the velocity correlations to vanish. Due to the limited changes of $\tau_v \sim 1$ and the extension of the superimposability region of the MSD and ISF curves around $t \sim 1$, the practical definition $< u^2 > \equiv < r^2(t = 1.022) >$ is adopted [421]. In view

of the comparison with the experiment this choice is also motivated by noting that the experimental DW factor $< u^2 >_{exp}$ is collected during few picoseconds (e.g. see [413]), i.e. in a lapse of time consistent with our definition, since one MD time unit $\sigma\sqrt{m/\epsilon}$ corresponds to about $1 - 10ps$, depending on the polymer of interest [15].

Fig.12.3 plots the dependence of the structural relaxation time τ_α on the mean square amplitude $< u^2 >$. The data collapse on a well-defined master curve nicely fitted by Eq.12.4. Additional data about the collective relaxation time τ from [421] are also shown and fitted by the same master curve after a suitable vertical shift. The best fit values of Eq.12.4 ($\overline{a^2}^{1/2} \sim 0.35$ and $\sigma^2_{a^2} \sim 0.25$) are consistent with the previous discussion, i.e. the MSD involved in the structural relaxation is, with some spread, a fraction of the molecular radius.

12.2.2 Comparison with experiments

Now we prove that the scaling evidenced by simulations may be extended to the experimental results. For each system the temperature dependencies of the mean square displacement $< u^2 >$ and τ_α or η are used. The pairs $(< u^2 >, \tau_\alpha)$ or $(< u^2 >, \eta)$ are preferably taken from the same source, if possible. In the absence of a single paper, the pairs are taken from different sources provided that the temperature ranges of the two studies overlap meaningfully and include the glass transition region. For some systems both viscosity and structural relaxation data were considered. The mean square displacements $< u^2 >$ are drawn from incoherent neutron scattering (INS) and Mössbauer spectroscopy (MS). The former takes $< u^2 >$ from the Debye-Waller Factor, the latter from the Lamb-Mössbauer factor $f \propto \exp(-q^2 < u^2 >)$ with $q = 7.3\text{Å}^{-1}$. The fragilities were drawn from refs. [395, 450]. The structural relaxation (in seconds) and the viscosity (in Pa·s) were scaled to the MD master curve by logarithmic vertical shifts in Fig. 3. Table 12.1 lists in order of increasing fragility the systems, the data

Table 12.1: Relevant information about the investigated systems (in order of increasing fragility) and the MD simulations. The structural relaxation time (ps)is taken via either dielectric spectroscopy or, for a part of the data set of B_2O_3, data aggregated from different techniques. The mean square displacement (in Å) is taken from Incoherent Neutron Scattering (INS) or Mössbauer Spectroscopy (MS). The logarithmic vertical shifts to scale the experimental curves to the MD master curve in Fig. 3 and the mean square displacement at T_g, $< u_g^2 >$ (or $-\ln f_g$ for MS), are also given.

system	τ_α, η			$< u^2 >$		
	quantity	shift	ref.	technique	$< u_g^2 >$ $-\ln f_g$	ref.
MD	MD	0		MD	0.01667	
B_2O_3	η	-2.2	[451]	INS	0.065	[452]
B_2O_3	$\tau_\alpha^\dagger$	+8.4	[453]	INS	0.065	[452]
$Zr_{46.8}Ti_{8.2}Cu_{7.5}Ni_{10}Be_{27.5}$	η	+1	[454]	MS	0.885	[455]
Glycerol	η	+1	[456]	INS	0.022	[457]
PI	τ_α	+12	[458]	INS	0.427	[459]
TNB	η	+2	[460]	INS	0.315	[461]
Fe+DBP	τ_α	+11	[462]	MS	3.15	[462]
Fe+DBP	η	+2	[463]	MS	3.05	[462]
OTP	τ_α	+11	[461]	INS	0.215	[464]
OTP	η	+1	[464]	INS	0.232	[464]
Selenium	η	+1.66	[413]	INS	0.155	[413]
1,4 PBD	τ_α	+11	[465]	INS	0.102	[466, 467]
a-PP	τ_α	+11.5	[468]	INS	0.13	[469]
PMMA	τ_α	+11.5	[470]	INS	1.1	[471]
PVC	τ_α	+11	[472]	INS	0.51	[471]

† data aggregated from different techniques.

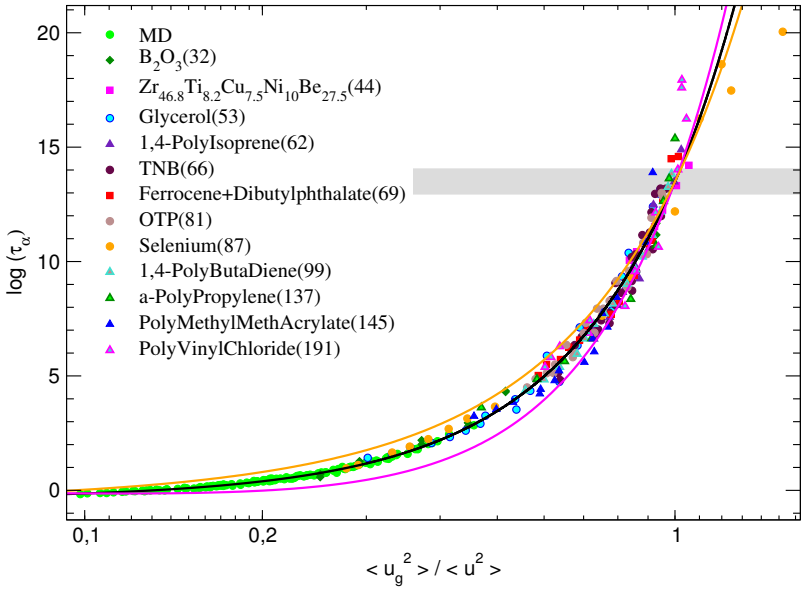

Figure 12.4: Scaling of the structural relaxation time τ_α (in MD units) vs. $\tilde{x} =< u_g^2 > / < u^2 >$. The grey area marks the glass transition. The continuous (central) line is $log_{10}\tau_\alpha = \alpha + \tilde{\beta}\tilde{x} + \tilde{\gamma}\tilde{x}^2$ with $\tilde{\beta} = \beta/0.129$ and $\tilde{\gamma} = \gamma/0.129^2$; α, β, γ from Fig.12.3. The numbers in parenthesis denote the fragility m covering the range from very strong to very fragile systems. Data about the structural relaxation (in seconds) and the the viscosity (in Pa·s) were scaled to the MD master curve by logarithmic vertical shifts $+11.5 \pm 0.5$ and $+1.5 \pm 0.5$, respectively, apart from B_2O_3 (+8.4(5) and -2.2(5)). Data of polymers refer to τ_α. Data related to B_2O_3, OTP, Ferrocene/Dibutylphthalate include two independent sets, one for τ_α, the other for η, which for simplicity are presented with the same symbol. Magenta(bottom) and orange(top) lines represent the extrapolation of simulation data in case a different value of the time for the evaluation of $< u^2 >$ is chosen: t=0.6 (magenta) and t=1.4 (orange); see also fig. 12.2, inset in top figure.

sources for τ_α or η, the vertical shifts, the experimental technique used to measure $< u^2 >$ and its value at T_g, $< u_g^2 >$ (or $-\ln f_g$ for Mössbauer experiments). Notice that for B_2O_3 two independent sets concerning τ_α and η were considered. The shifts of τ_α and η of B_2O_3 differ about three orders of magnitude with respect to the ones of the other systems. However, the difference between the shifts of the two sets (+10.6) is close to the difference of the shifts of the other systems ($\simeq$ +10.0(7)).

As a preliminary step, let us locate $< u^2 >$ at T_g of the model polymer system

assuming that eq. 12.4 with the best-fit parameters from Fig.12.3. For the MD simulation the time unit corresponds to $1 - 10\ ps$, as noted above. Then, the customary definition of T_g according to the equation $\tau_\alpha(T_g) = 10^2 s$ in laboratory units [372] corresponds to $\tau_\alpha(T_g) = 10^{13} - 10^{14}$ in dimensionless MD units. Eq.12.4 with the best-fit parameters from Fig.12.3 yields $\sqrt{< u_g^2 >} = 0.129(1)$ at T_g ($< u_g^2 >$ being the DW factor at the glass transition). This amplitude corresponds to the ratio $v_0 \cong (2\sqrt{< u_g^2 >})^3 = 0.017$ between the volume which is accessible to the monomer center-of-mass and the monomer volume. Flory and coworkers proposed that the glass transition takes place under iso-free volume conditions with the universal value $v_0 \cong 0.025$ [51, 474, 475]. Furthermore, an extension of the ACS model (leading to Eq.12.3) predicts that, just as for a crystalline solid [447, 448], there is a Lindemann criterion for the stability of glasses stating that at T_g the ratio f between $\sqrt{< u_g^2 >}$ and the average next neighbor distance of the atoms in the lattice is a quasi-universal number ($f \cong 0.1$)[440]. From this respect, the ratio $f \simeq 0.12 - 0.13$ at T_g for our data supports this expectation and is close to $f = 0.129$ for the melting of a hard sphere fcc solid [448]. After this preliminary analysis, we are now in a position to test the scaling of the available experimental data. Both experiments [447] and simulations [448] show that the Lindemann ratio (weakly) depends on both the given type of interaction potential and the given crystal structure. With the purpose of removing both this (small) effect and the evaluation of the average next neighbor distance of the atoms (not trivial for molecular systems) we plot the structural relaxation time τ_α versus the reduced variable $\tilde{x} =< u_g^2 > / < u^2 >$. For MD data we set $< u_g^2 >= 0.129$. The underlying hypothesis is that the curve $log_{10}\tau_\alpha = \alpha + \tilde{\beta}\tilde{x} + \tilde{\gamma}\tilde{x}^2$ with $\tilde{\beta} = \beta/0.129$ and $\tilde{\gamma} = \gamma/0.129^2$ (α, β, γ from Fig.12.3) is a universal master curve. Fig.12.4 puts under test that scaling hypothesis for several glassformers and polymers in a wide range of fragility ($32 \leq m \leq 191$) which compares well with the range covered by ref. [436] ($20 \leq m \leq 87$) and [437] ($20 \leq m \leq 100$). We were unable to find other data in the available literature. The result proves that the reduced

variable $\tilde{x}$ yields good scaling and that information about it is found in the liquid state. Connections between the dynamics far from and close to the glass transition were previously noted [437] and motivated the search of correlations between the fragility and the Poisson's ratio [437] which was disputed [441]. The fact that the metallic glass $Zr_{46.8}Ti_{8.2}Cu_{7.5}Ni_{10}Be_{27.5}$ which does not support that correlations (see [441]; it corresponds to the point with coordinates m=44, ν_l/ν_t=2.08 in their Fig.1), fits our scaling plot seems to offer a way for reconciliation.

Chapter 13

Conclusions and further studies

13.1 Conclusions

Here we have shown, by computer simulations and comparison with the experiment, a scaling between τ_α (the structural relaxation time and hence a global property of the sample) and the rattling amplitude $< u^2 >$ (which refers to localized fast dynamics) over almost fifteen decades of relaxation times which unravels a universal curve with simple analytical form obeyed by both fragile and strong systems [372]. The results clarify recent correlations between liquids and glasses[437], offer a reconciliation with contrasting evidence [441], and prove that known correlations between the relaxation very close to T_g, setting the fragility, and the vibrational glassy-like dynamics [422, 435–439] extend very much above T_g. Furthermore, they readdress the old idea that the glass transition takes place under iso-free volume conditions [51], also inherent in the "glassy" Lindemann criterion [440].

13.2 Further studies

Several possibility for future studies can be explored:

- Concerning the simulative point of view, it is of great importance testing the presumed universality of the scaling between global and local motion just presented against other samples; possible choices for suitable system could be water, which requires a long range electrostatic potential, and the widely used binary mixture. More complex systems, like network forming materials, such as silica, would be of great interested to be investigated.

- An aspect not touched in the present work is the relation between crystallization and glassy state; in the present case, this can be achieved, for example, with a deep analysis of the effects of changing the torsional potential used in the Part I of this work. A glimpse of that can be caught from ref. [473].

- Improving the temperatures sampled, would be also possible to test the variations in fragility and glass transition temperature due to chain legth. A possible way to evaluate these two thing can be borrowed from [422].

Appendix A

Gibbs-Thomson equation

The notation employed in the following text is mutuated by chapter 5.

As known from basic thermodynamic, the free energy at a given temperature T can be written as:

$$F = H - TS \tag{A.1}$$

Where H is the enthalpy and S the entropy at some temperature T. When the system melts:

$$F(T_m^0) = H(T_m^0) - T_m^0 S(T_m^0) = 0 \tag{A.2}$$

Where T_m^0 is the melting temperature of a perfect crystal. From this equation follows:

$$S(T_m^0) = \frac{H(T_m^0)}{T_m^0} \tag{A.3}$$

If the system is at a temperature T not far from the melting temperature T_m^0, it is fair to suppose that H and S are substantially unchanged. Substituting eq. A.3 in eq. A.1 :

$$F(T) = \frac{H(T_m^0)\,(T_m^0 - T)}{T_m^0} \tag{A.4}$$

Coming back to the problem of polymer crystallization, we focalize our atten-

tion on eqs. 5.5. If we represent the bulk free energy using A.4, we can write:

$$\begin{aligned} T_m &= T_m^0 \left(1 - \frac{6\sigma_e^{1/3}\sigma_s^{2/3}}{H(T_m^0)V^{1/3}}\right) \\ &= T_m^0 \left(1 - \frac{6\sigma_e}{H(T_m^0)L^*}\right) \\ &= T_m^0 \left(1 - \frac{6\sigma_s}{H(T_m^0)W^*}\right) \end{aligned} \tag{A.5}$$

This equations are correct only around the melting temperature and make possible to link the expected melting temperature T_m with the geometrical properties of the crystal. In particular, T_m^0 can be inferred as the temperature of a crystal of infinite size. Equations A.5 are known as the Gibbs-Thomson equation. For its applications see section 3.2.

Bibliography

[1] H.F. Mark, K.H. Meyer; *Der Aufbau der hochpolymeren organischen Naturstoffe* (Akademische Verlagsgesellschaft, Leipzig, 1930).

[2] D.I. Bower; *An Introduction to Polymer Physics* (Cambridge University Press, Cambridge, 2002).

[3] P.J. Flory; *Principles of Polymer Chemistry* (Cornell University Press, Ithaca, New York, 1953).

[4] P.J. Flory; *Statistical Mechanics of Chain Molecules* (Interscience, New York, 1969).

[5] P.J. Flory; *Nobel Lecture 1974*. Available on `http://nobelprize.org/nobel_prizes/chemistry/laureates/1974/flory-lecture.pdf`

[6] I.M. Lifshitz, A.Y. Grosberg, A.R. Khokhlov; Rev. Mod. Phys. 50, 683 (1978).

[7] A. Yu. Grosberg, A. R. Khokhlov; *Statistical Physics of Macromolecules* (AIP Press, New York, 1994).

[8] M. Doi, S.F. Edwards; *The Theory of Polymer Dynamics* (Academic Press, New York, 1986).

[9] P.G. de Gennes; *Scaling Concept in Polymer Physics* (Cornell University Press, Ithaca, New York, 1979).

[10] `http://www.mpcfaculty.net/mark_bishop/addition_polymers.htm`

[11] G. Strobl; *The Physics of Polymers* (Springer, New York, 1997).

[12] J. Baschnagel, F. Varnik; J. Phys.: Condens. Matter 17, R851 (2005).

[13] H. Meyer, F. Müller-Plathe; J. Chem. Phys. 115, 7807 (2001).

[14] H. Meyer, F. Müller-Plathe; Macromolecules 35, 1241 (2002).

[15] M. Kröger; Phys. Rep. 390, 453 (2004).

[16] F. Müller-Plathe; Chem. Phys. Chem. 3 754 (2002).

[17] F. Müller-Plathe; Soft Matter 1 1 (2003).

[18] S.C. Glotzer, W. Paul; Annu. Rev. Mater. Res. 32, 401 (2002).

[19] K. Binder; *Monte Carlo and Molecular Dynamics Simulations in Polymer Science* (Oxford University Press, new York, 1995).

[20] W. Kob in *Annual Reviews of Computational Physics*, D. Stauffer ed. (World Scientific, Singapore, 1995).

[21] W. Kob; J. Phys.: Condens. Matter 11 R85 (1999).

[22] K. Binder, J. Horbach, W. Kob, W. Paul, F. Varnik; J. Phys.: Condens. Matter 16 S429 (2004).

[23] J. GrotenDorst, D. Marx, A. Maramatsu editors; *Modern Methods and Algorithms of Quantum Chemistry* (NIC series, Jülich, 2000);

[24] W. Paul, G.D. Smith; Prog. Phys. 67,1117 (2004).

[25] J. Baschnagel, K. Binder, P. Doruker, A.A. Gusev, O. Hahn, K. Kremer, W.L. Mattice, F. M̈ller-Plathe, M. Murat, W. Paul, S. Santos, U.W. Suter, V. Tries; *Advanced Polym. Sci.* 152, 41 (2000).

[26] N. Attig, K. Binder, H. Grubmüller, K. Kremer editors; *Computational Soft Matter: From Synthetic Polymers to Proteins* (NIC series, Jülich, 2004);

[27] K. Kremer, K. Binder; Comput. Phys. Rep. 7, 259 (1988).

[28] K. Armitstead, G. Golbeck-Wood; *Adv. Polym. Sci.* 100, 219 (1992).

[29] G. Strobl; Prog. Polym. Science 31, 398 (2006).

[30] K.H. Stroks; J. Am. Chem. Soc. 60, 1753 (1938).

[31] A. Keller, Philos. Mag. 2, 1171 (1957).

[32] J. I. Lauritzen Jr, J. D. Hoffman; J. Res. Nat. Bur. Stand. A 64, 73 (1960).

[33] J. D. Hoffman, J. I. Lauritzen Jr; J. Res. Nat. Bur. Stand. A 65, 297 (1961).

[34] A. Peterlin, E.W. Fischer, C. Reinhold; J. Chem. Phys. 37, 1403 (1962).

[35] J.M. Peterson, P.H. Lindenmeyer; Makromol. Chem. 118, 343 (1968).

[36] Faraday Discuss. Chem. Soc. 68 (1979).

[37] D. M. Sadler; Polymer 24, 1401 (1983).

[38] D. M. Sadler; Phys. Rev. Lett. 56, 2708 (1986).

[39] D. M. Sadler; Nature 326, 174 (1987).

[40] D. M. Sadler, G. H. Gilmer; Polymer Commun. 28, 232 (1987).

[41] G. Strobl; Eur. Phys. J. E 3, 165 (2000).

[42] J. M. G. Cowie; *Polymers: Chemistry and Physics of Modern Materials* (Chapman & Hall, New York, 1991).

[43] C.R. Ashcraft, R.H. Boyd; J. Polym. Sci. Phys. Ed. 14, 2153 (1976).

[44] M.L. Mansfield, R.H. Boyd; J. Polym. Sci. Phys. Ed. 16, 1227 (1978).

[45] R.H. Boyd; Macromolecules 17, 903 (1984).

[46] B. Wunderlich, M. Moller, J. Grebowicz, H. Baur; Adv. Polym. Sci. 87 (1988).

[47] C.W. Bunn, E.V. Garner; Proc. Royal Soc. A. 189, 39 (1947).

[48] A. Keller; Rep. Prog. Phys. 31, 623 (1968).

[49] G. Natta, P. Corradini, M. Cesari; Atti Accad. Naz. Lincei. Rc. 21, 365 (1956).

[50] M. Guaita, F. Ciardelli, F. LA Mantia, E. Pedemonte; *Fondamenti di Scienza dei Polimeri* (Pacini Editore, 1998).

[51] U. W.Gedde, *Polymer Physics* (Chapman and Hall, London, 1995).

[52] P. J. Philips; Rep. Prog. Phys. 53, 549 (1990).

[53] P.H. Geil; Polymer 41, 8983 (2000).

[54] P.H. Till; J. Polym. Sci. 24, 30 (1957).

[55] E.W. Fischer; Z. Naturf. 12a, 753 (1957).

[56] C.W. Bunn; Trans. Faraday Soc. 35, 428 (1939).

[57] Faraday Discuss. Chem. Soc. 25 (1958).

[58] J.D. Hoffman; Polymer 24, 3 (1983).

[59] D.Y. Yoon, P.J. Flory; Polymer 18, 509 (1977).

[60] M.L. Mansfield; Macromolecules 16, 914 (1983).

[61] D.M. Sadler, R. Harris; J. Polym. Sci. Polym. Phys. Ed. 20, 561 (1982).

[62] S.J. Spells, D.M. Sadler; Polymer 25, 739 (1984).

[63] S.J. Spells, A. Keller, D.M. Sadler; Polymer 25, 749 (1984).

[64] A. Peterlin J. Appl. Phys. 31, 1934 (1960).

[65] A. Peterlin, E.W. Fischer, C. Reinhold; Z. Physik 159, 272 (1960).

[66] A. Peterlin, C. Reinhold; J. Polymer Sci. A3, 2801 (1965).

[67] M.L. Huggins; J. Polymer Sci. 50, 65 (1961).

[68] M.L. Huggins; Makromol. Chem. 92, 260 (1966).

[69] H.G. Zachmann; Kolloid Z. Z. Polym. 321, 504 (1967).

[70] J.D. Hoffman, R.L. Miller; Polymer 38, 3151 (1997).

[71] D.M. Sadler; J. Chem. Phys. 97, 1771 (1987).

[72] D.M. Sadler; Polymer 28, 1440 (1987).

[73] J.I. Lauritzen Jr; J. Appl. Phys. 44, 4353 (1973).

[74] I.C. Sanchez, E.A. Di Marzio; J. Chem. Phys 55, 893 (1971).

[75] F.C. Frank; J. Cryst. Growth 22, 233 (1974).

[76] C.H. Bennett, M. Buttiker, R. Landauer, H. Thomas; J. Stat. Phys. 24, 419 (1981).

[77] N. Goldenfeld; J. Phys. A 17, 2807 (1984).

[78] A. Toda, Y. Tanzawa; J. Cryst. Growth 76, 462 (1986).

[79] D.J. Gates, M. Westcott; Proc. Royal Soc. London A 416, 443 (1988).

[80] C.M. Guttmann, E.A. Di Marzio; J. Appl. Phys. 54, 5541 (1983).

[81] D.J. Blundell, A. Keller; J. Macr. Sci. Phys. B 2, 337 (1968).

[82] A. Keller, E. Pedemonte; J. Cryst. Growth 18, 111 (1973).

[83] M. Cooper, R.St.J. Manley; Macromolecules 8, 219 (1975).

[84] S.J. Organ, A. Keller; J. Polym. Sci. C 25, 67 (1987)

[85] A. Toda, H. Kiho; J. Phys. Soc. Jpn. 56, 1631 (1987).

[86] A. Toda, H. Kiho; J. Polym. Sci. Polymer. Phys. Ed. 27, 53 (1989).

[87] A. Toda, H. Kiho, H. Miyaji, K. Asai; J. Phys. Soc. Jpn. 54, 1411 (1985).

[88] A. Toda, H. Miyaji, H. Kiho; Polymer 27, 1505 (1986).

[89] D.M. Sadler; J. Polymer. Sci. A 2, 779 (1971).

[90] B. Wunderlich, A. Metha; J. Polym. Sci. Polym. Phys. Ed. 11, 1259 (1973).

[91] J.J. Point, M.C. Colet, M. Dosière; J. Polym. Sci. Polymer. Phys. Ed. 24, 357 (1986).

[92] M. Dosière, M.C. Colet, J.J. Point; J. Polym. Sci. Polymer. Phys. Ed. 24, 345 (1986).

[93] M.C. Colet, J.J. Point, M. Dosière; J. Polym. Sci. Polymer. Phys. Ed. 24, 1183 (1986).

[94] J.D. Hoffman, R.L. Miller; Macromolecules 22, 3038 (1989).

[95] F.C. Frank, M. Tosi; Proc. Royal Soc. A 263, 323 (1961).

[96] J.J. Point; Macromolecules 12 ,770 (1979).

[97] E.A. Di Marzio, C.M. Guttman; J. Appl. Phys. 53, 6581 (1982).

[98] J.I. Lauritzen Jr, E.A. Di Marzio, E. Passaglia; J. Chem. Phys. 45, 4444 (1966).

[99] E. Helfand, J.I. Lauritzen Jr; Macromolecules 6, 631 (1973).

[100] E.A. Di Marzio; J. Chem. Phys. 47, 3451 (1967).

[101] I.C. Sanchez, E.A. Di Marzio; J. Res. Nat. Bur. St. 76A, 213 (1972).

[102] E.A. Di Marzio, E. Passaglia; J. Chem. Phys. 87, 4901 (1987).

[103] E. Passaglia, E.A. Di Marzio; J. Chem. Phys. 87, 4908 (1987).

[104] J.D. Hoffman, R.L. Miller; Macromolecules 21, 3028 (1988).

[105] M.L. Mansfield; Polymer 29, 1755 (1988).

[106] M.L. Mansfield; Polym, Commun, 31, 283 (1990).

[107] M. Hikosaka; Polymer 28, 1257 (1987).

[108] M. Hikosaka; Polymer 31, 458 (1990).

[109] A. Keller, M. Machin; J. Macrom. Sci. Phys. B1, 41 (1967).

[110] A. Keller, F.M. Willmouth; J. Macrom. Sci. Phys. B6, 493 (1972).

[111] I. Dukovski, M. Muthukumar; J. Chem. Phys. 118, 6648 (2003).

[112] S. Liu, B. Ashok, M. Muthukumar; Polymer 45, 1383 (2004).

[113] C. Baig, B.J. Edwards, D.J. Keffer, H. Cochran, V.A. Harmandaris; J. Chem. Phys. 124, 084902 (2006).

[114] C. De Rosa, F. Auriemma, O. Ruiz de Ballesteros; Phys. Rev. L. 96, 167801 (2005).

[115] M.H.E. Van der Beek, G.W.M. Peters, H.E.M. Meijer; Macromolecules 39, 1805 (2006).

[116] H. Sata, T. Kimura, S. Ogawa, M. Yamamoto, E. Ito; Polymer 37, 1879 (1996).

[117] H. Sata, T. Kimura, S. Ogawa, M. Yamamoto, E. Ito; Polymer 39, 6325 (1998).

[118] T. Kimura, T. Kawai, Y. Sakamoto; Polymer 41, 809 (2000).

[119] F. Ebert, T. Thurn-Albrecht; Macromolecules 36, 8685 (2003).

[120] `http://www.tennoji-h.oku.ed.jp/tennoji/oka/2003/n-pentane-b.gif`

[121] C. Liu, M. Muthukumar; J. Chem. Phys. 109, 2536 (1998).

[122] M. Muthukumar, P. Welch; Polymer 41, 8833 (2000).

[123] M. Muthukumar; Phil. Trans. R. Soc. Lond. A 361, 539 (2003).

[124] P. Welch, M. Muthukumar; Phys. Rev. Lett. 87, 218302 (2001).

[125] S. Fujiwara, T. Sato; J. Chem. Phys. 114, 6455 (2001).

[126] M. P. Allen, D. J. Tildesley; *Computer Simulation of liquids* (Clarendon, Oxford, 1987).

[127] D. C. Rapaport; *The Art of Molecular Dynamics Simulation* (Cambridge University Press, Cambridge, 1995).

[128] D. Frenkel, B. Smit; *Understanding molecular simulation*, 2nd Ed. (Academic Press, New York, 2002).

[129] L. Larini, A. Barbieri, D. Prevosto, P.A. Rolla, D. Leporini; J. Phys.: Condens. Matter 17, L199 (2005).

[130] L. Larini, D. Leporini; J. Chem. Phys. 123, 144907 (2005).

[131] Y. Lei, C. Chan, J. Li, K. Ng, Y. Wang, Y. Jiang, L. Li; Macromolecules

35, 6751 (2002).

[132] Y. Lei, C. Chan, Y. Wang, K. Ng, Y. Jiang, L. Li; Polymer 44, 4673 (2003).

[133] A.S. Vaughan, D.C. Basset; In: C. Booth and C. Price editors; *Comprehensive polymer science* (Pergamon Press, Oxford, 1989), Vol. 2, p. 415 .

[134] J. Hobbs; Chin. J. Polym. Sci. 21, 135 (2003).

[135] J. Hobbs; In: J.D. Batteas editor; *Applications of scanned probe microscopy to polymers* (Oxford Univeristy Press, Oxford, 2005), p. 194.

[136] R. Kolb, C. Wutz, N. Stribeck, G. von Krosigk, C. Riekel; Polymer 42, 5257 (2001).

[137] A. Häfele, B. Heck, T. Kawai, P. Kohn, G. Strobl; Eur. Phys. J. E 16, 207 (2005).

[138] B. Heck, T. Kawai, G. Strobl; Polymer 47, 5538 (2006).

[139] J. Fritsch, W. Stille, G. Strobl; Colloid. Polym. Sci. 284, 620 (2006).

[140] B. Heck, G. Strobl, M. Grasruck; Eur. Phys. J. E 11,117 (2003).

[141] D. Patel, D.C. Basset; Proc. R. Soc. Lond. A 445, 577 (1994).

[142] D.A. Ivanov, Z. Amalou, S. Magonov; Macromolecules 34, 8944 (2001).

[143] W. Hu, K. Schmidt-Rohr; Acta Polym. 50, 271 (1999).

[144] T. Cho, B. Heck, G. Strobl; Colloid. Polym. Sci. 282, 825 (2004).

[145] T. Hugel, G. Strobl, R. Thomann; Acta polym. 50, 214 (1999).

[146] S. Magonov, Y. Godovsky; Am. Lab. 31,52 (1999).

[147] W. Hu, D. Frenkel; Adv. Polym. Sci. 191, 1 (2005).

[148] M.L. Huggins; J. Chem. Phys. 9, 440 (1941).

[149] P.J. Flory; J. Chem. Phys. 9, 660 (1941).

[150] P.J. Flory; J. Chem. Phys. 10, 51 (1942).

[151] J.W. Cahn, J.E. Hilliard; J. Chem. Phys. 28, 258 (1958).

[152] P.D. Olmsted, W.C.K. Poon, T.C.B. McLeish, N.J. Terrill, A.J. Ryan; Phys. Rev. Lett. 81, 373 (1998)

[153] J. Loos, P.C. Thüne, P.J. Lemstra, W.J. Niemantsverdriet; Macromolecules

32,8910 (1999).

[154] B. Goderis, H. Reynaers, R. Scharrenberg, V. Mathot, M.H.J. Koch; Macromolecules 34, 1779 (2001).

[155] G. Hauser, J. Schmidtke, G. Strobl; Macromolecules 31,6250 (2002).

[156] D.C. Basset, D. Patel; Polymer 35, 1855 (1994).

[157] A. Wurm, C. Schick; e-Polymers 024 (2002).

[158] Y. Jiang, Q. Gu, L. Li, D. Shen, X. Jin, C. Chan; Polymer 44, 3509 (2003).

[159] A. Padermsoke, H. Sato, Y. Katsumoto, S. Ekgasit, I. Noda, Y. Ozaki; Polymer 45, 7159 (2004).

[160] J. Zhang, Y. Duan, D. Shen, S. Yan, I. Noda, Y. Ozaki; Macromolecules 37, 3292 (2004).

[161] P. Kohn, G. Strobl; Macromolecules 37, 6823 (2004).

[162] D.A. Ivanov, S. Hocquet, M. Dosière, M.H.J. Koch; Eur. Phys. J. E 13, 363 (2004).

[163] T. Liu, J. Petermann, C. He, Z. Liu, T. Chung; Macromolecules 34, 4305 (2001).

[164] Y. Jiang, X. Jin, C. Han, L. Li, Y. Wang, C. Chan; Langmuir 19, 8010 (2003).

[165] T. Hippler, S. Jiang, G. Strobl; Macromolecules 38, 9396 (2005).

[166] B.Lee, T.J. Shin, S.W. Lee, J. Yoon, J. Kim, H.S. Youn, M. Ree; Polymer 44, 2509 (2003).

[167] G. Dreezen, M.H.J. Koch, H. Reynaers, G. Groeninckx; Polymer 40, 6451 (1999).

[168] C. ougnies, M. Dosière, M.H.J. Koch, J. Roovers; Macromolecules 31, 6266 (1999).

[169] B. Heck, T. Hugel, M. Iijima, E. Sadiku, G. Strobl; New J. Phys. 1, 17.1 (1999).

[170] M. Al-Hussein, G. Strobl; Eur. Phys. J. E 6, 305 (2001).

[171] M. Grasruck, G. Strobl; Macromolecules 36, 86 (2003).

[172] G. Strobl; Eur. Phy. J. E 18, 295 (2005).

[173] M. Al-Hussein, G. Strobl; Macromolecules 35, 1672 (2002).

[174] A. Minakov, D. Mordvintsev, C. Schick; Polymer 45, 3755 (2004).

[175] S. Rastogi, M. Hikosaka, H. Kawabata, A. Keller; Macromolecules 24, 6384 (1991).

[176] A. Keller, M. Hikosaka, S. Rastogi, A. Toda, P. Barham, G. Goldbeck-Wood; J. Mater. Sci. 29, 2579 (1994).

[177] A. Tracz, J. Jeszka, I. Kucinska, J. Chapel, G. Boiteux; J. Appl. Polym. Sci. 86,1329 (2002).

[178] S. Rastogi, L. Kurelec; J. Mater. Sci. 35,5121 (2000).

[179] S. Tsubakihara, A. Nakamura, M. Yasuniwa; Polym. J. 28, 489 (1996).

[180] E.B.Sirota, A.B.Herhold; Science 283, 529 (1999).

[181] G. Ungar; Macromolecules 19, 1317 (1986).

[182] T. Nakaoki, Y. Ohira, H. Hayashi, F. Horii; Macromolecules 31, 2705 (1998).

[183] Y. Ohira, F. Horii, T. Nakaoki; Macromolecules 33, 5566 (2000).

[184] T. Nakaoki, T. Yamanaka, Y. Ohira, F. Horii; Macromolecules 33, 2718 (2000).

[185] V. Vittoria, L. Guadagno, A. Comotti, R. Simonutti, F. Auriemma, C. De Rosa; Macromolecules 33, 6200 (2000).

[186] C. De Rosa, F. Auriemma, O. Ruiz de Ballesteros; Polymer 42, 9729 (2001).

[187] C. De Rosa, O. Ruiz de Ballesteros, M. Santoro, F. Auriemma; Polymer 44, 6267 (2003).

[188] G. Ungar, J. Stejny, A. Keller, I. Bidd, M.C. Whiting; Science 229, 386 (1985).

[189] G. Alamo, L. Mandelkern, G.M. Stack, C. Krohnke, G. Wegner; Macromolecules 26, 2743 (1993).

[190] S.J. Organ, A. Keller, M. Hikosaka, G. Ungar; Polymer 37, 2517 (1996).

[191] G. Ungar, A. Keller; Polymer 27, 1835 (1986).

[192] G. Alamo, L. Mandelkern, G.M. Stack, C. Krohnke, G. Wegner; Macro-

molecules 27, 147 (1994).

[193] S.K. Ghosh, M. Hikosaka, A. Toda, S. Yamazaki, K. Yamada; Macromolecules 35, 6985 (2002).

[194] R.H. Gee , L.E. Fried; J. Chem. Phys. 118, 3827 (2003).

[195] H. Bu, Y. Pang, D. Song, T. Yu, T. M. Voll, G. Czornyj, B. Wunderlich; J.Polymer Sci., Part B: Polym. Phys. 29, 139 (1991).

[196] L.Z.Liu , F.Y.Su , H.S.Zhu , H.Li , E.L.Zhou , R.F.Yan , R.Y.Qian; J.Macromol.Sci.,Phys.B, 36, 195 (1997).

[197] T.A. Kavassalis, P.R. Sundararajan; Macromolecules 26, 4144 (1993).

[198] P.R. Sundararajan, T.A. Kavassalis; J. Chem. Soc. Faraday Trans. 91,2541 (1995).

[199] S. Fujiwara, T. Sato; J. Chem. Phys. 110, 9757 (1999).

[200] S. Fujiwara, T. Sato; J. Chem. Phys. 107, 613 (1997).

[201] S. Fujiwara, T. Sato; Comput. Phys. Comm. 142, 123 (2001).

[202] S. Fujiwara, T. Sato; Comput. Phys. Comm. 147, 342 (2002).

[203] H.Meyer, F. Muller-Plathe; J. Chem. Phys. 115, 7807 (2001).

[204] W.Hu , D.Frenkel; V.B.F.Mathot, J. Chem. Phys. 118, 3455 (2003).

[205] W.Hu , D.Frenkel; V.B.F.Mathot, Macromolecules 36, 8178 (2003).

[206] J.P.K.Doye , D.Frenkel; J. Chem. Phys. 110, 7073 (1999).

[207] W.Hu ; J. Chem. Phys. 113, 3901 (2000).

[208] F. Sciortino; J. Stat. Mech. P05015 (2005).

[209] D.J. Wales; Phil. Trans. R. Soc. A 363, 357 (2005).

[210] D.J. Wales; *Energy Landscapes* (Cambridge University Press, Cambridge, 2003).

[211] J.D. Bryngelson, P.G. Wolynes; Proc. Natl. Acad. Sci. USA 84, 7524 (1987).

[212] J.D. Bryngelson, P.G. Wolynes; J. Phys. Chem. 93, 6902 (1989).

[213] J.D. Bryngelson, P.G. Wolynes; Biopolymers 30, 177 (1990).

[214] J.D. Bryngelson, J.N. Onuchic, N.D. Socci, P.G. Wolynes; Proteins: Struct., Func. Gen. 21, 167 (1995).

[215] P.E. Leopold, M. Montal, J.N. Onuchic; Proc. Natl. Acad. Sci. USA 89, 8721 (1992).

[216] J.N. Onuchic, P.G. Wolynes, Z. Luthey-Schulten, N.D. Socci; Proc. Natl. Acad. Sci. USA 92, 3626 (1995).

[217] J.N. Onuchic, Z. Luthey-Schulten, P.G. Wolynes; Annu. Rev. Phys. Chem. 48, 545 (1997).

[218] H. Nymeyer, A.E. García, J.N. Onuchic; Proc. Natl. Acad. Sci. USA 95, 5921 (1998).

[219] C.M. Dobson, A. Šali, M. Karplus; Angew. Chem. Int. Ed. 37, 868 (1998).

[220] K.A. Dill, H.S. Chan; Nature Struct. Biol. 4, 10 (1997).

[221] P. G. Debenedetti, F. H. Stillinger; Nature 410, 259 (2001).

[222] C.L. Brooks, J.N. Onuchic, D.J. Wales; Science 293, 612 (2001).

[223] F.H. Stillinger, T.A. Weber; Phys. Rev. A 25, 978 (1982).

[224] F.H. Stillinger, T.A. Weber; Science 225, 983 (1984).

[225] F.H. Stillinger; Science 267, 1935 (1995).

[226] C. Levinthal in *Mössbauer Spectroscopy in Biological Systems*, P. Debrunner, J.C.M Tsibris, E. Münck edts. (University of Illinois Press, Urbana, 1969).

[227] J.P.K Doye, D.J. Wales; J. Chem. Phys. 105, 8428 (1996).

[228] R. Zwanzig, A. Szabo, B. Bagchi; Proc. Natl. Acad. Sci. USA 89, 20 (1992).

[229] R. Zwanzig; Proc. Natl. Acad. Sci. USA 92, 9801 (1995).

[230] C.D. Sfatos, A.M. Gutin, E.I. Shakhnovich; Phys. Rev. E 48, 465 (1993).

[231] V.S. Pande, A.Y. Grosberg, T. Tanaka; Phys. Rev. E 51, 3381 (1993).

[232] A.M. Gutin, V.I. Abkevich, E.I. Shakhnovich; Phys. Rev. Lett. 77, 5433 (1996).

[233] J. Wang, J.N. Onuchic, P.G. Wolynes; Phys. Rev. Lett. 76, 4861 (1996).

[234] J. Wang, S.S. Plotkin, P.G. Wolynes; J. Phys. I 7, 395 (1997).

[235] M. Karplus, A. Šali; Curr. Opin. Struct. Biol. 5, 58 (1995).

[236] J. Wang, K. Zhang, H. Lu, E. Wang; Phys. Rev. Lett. 96, 168101 (2006).

[237] O. Miyashita, P.G. Wolynes, J.N. Onuchic; Phys. Chem. B 109, 1959 (2005).

[238] O. Miyashita, J.N. Onuchic, P.G. Wolynes; Proc. Natl. Acad. Sci. USA 100, 12570 (2003).

[239] H. Frauenfelder, S.G. Sligar, P.G. Wolynes; Science 254, 1598 (1991).

[240] N.D. Socci, J.N. Onuchic, P.G. Wolynes; Proteins: Struct., Func. Gen. 32, 136 (1998).

[241] P.G. Wolynes, J.N. Onuchic, D. Thirumalai; Science 267, 1619 (1995).

[242] N.D. Socci, J.N. Onuchic, P.G. Wolynes; J. Chem. Phys. 104, 5860 (1996).

[243] S.S. Plotkin, J. Wang, P.G. Wolynes; Phys. Rev. E 53, 6271 (1996).

[244] S.S. Plotkin, J. Wang, P.G. Wolynes; J. Chem. Phys. 106, 2932 (1997).

[245] B.A. Shoemaker, J. Wang, P.G. Wolynes; Proc. Natl. Acad. Sci. USA 94, 777 (1997).

[246] J.N. Onuchic, H. Nymeyer, A.E. García, J. Chahine, N.D. Socci; Adv. Prot. Chem. 53, 87 (2000).

[247] T. Komatsuzaki, K. Hoshino, Y. Matsunaga, G.J. Rylance, L.J. Johnston, D.J. Wales; J. Chem. Phys. 122, 084714 (2006).

[248] M. Goldstein; J. Chem. Phys. 51, 3728 (1969).

[249] D. Chakrabarti, B. Bagchi; Phys. Rev. Lett. 96, 187801 (2006).

[250] S.N. ChakraBorty, C. Chakravarty; J. Chem. Phys. 124, 014507 (2006).

[251] P. Lucas; J. Phys.: Condens. Matter 18, 5629 (2006).

[252] R.M.J. Cotteril, J.U. Madsen; J. Phys.: Condens. Matter 18, 6507 (2006).

[253] A.J. Moreno, I. Saika-Voivod, E. Zaccarelli, E. La Nave, S.V. Buldyrev, P. Tartaglia, F. Sciortino; J. Chem. Phys. 124, 204509 (2006).

[254] A. Saksaengwijit, A. Heuer; Phys. Rev. E 73, 061503 (2006).

[255] A.J. Moreno, S.V. Buldyrev, E. La Nave, I. Saika-Voivod, F. Sciortino, P. Tartaglia, E. Zaccarelli; Phys. Rev. Lett. 95, 157802 (2005).

[256] C.A. Angell, J. Res. NIST 102, 171 (1997).

[257] L. Angelani, G. Parisi, G. Ruocco, and G. Viliani, Phys. Rev. Lett. 81, 4648 (1998).

[258] K.D. Ball, R.S. Berry, R.E. Kunz, F. Li, A. Proykova, D.J. Wales; Science 271, 963 (1996).

[259] G. Diezemann, R. Bömer; J. Chem. Phys. 124, 214597 (2006).

[260] S. Sen,T. Mukerji; J. Non-Cryst. Solids 351, 3361 (2005).

[261] L. Hu, X. Bian, W. Wang, G. Liu, Y. Jia; J. Phys. Chem. B 109, 13737 (2005).

[262] C. Li,Y. Matsunaga, M. Toda, T. Komatsuzaki; J. Chem. Phys. 123, 184301 (2005).

[263] J.P.K. Doye; Polymer 41, 8857 (2000).

[264] J. Lee, J.M. Kosterlitz; Phys. Rev. Lett. 65, 137 (1990).

[265] L. Larini, A. Barbieri, D. Leporini; Physica A 364, 183 (2006).

[266] L. Larini, D. Leporini; J. Non-Cryst. Solids 352, 5021 (2006).

[267] L. Larini, D. Leporini; Philos. Mag. 87, 411 (2007).

[268] B. Crist; Macromolecules 39, 1971 (2006).

[269] J. Sommer; Eur. Phys. J. E 19, 413 (2006).

[270] M. Muthukumar; Eur. Phys. J. E 3, 195 (2000).

[271] G. Wulff; Z. Kristallogr. 34, 449 (1901).

[272] B. Wunderlich; *Macromolecular physics* (Academic Press, New York, 1973).

[273] W. Ostwald; Z. Phys. Chem. Stoechiom. Verwandtschaftsl. 22, 289 (1897).

[274] S. Fujiwara, T. Sato; Comput. Phys. Comm. 142, 127 (2001).

[275] S. Fujiwara, T. Sato; Comput. Phys. Comm. 147, 346 (2002).

[276] W.C. Bunn; J. Polym. Sci. 16, 323 (1955).

[277] A. Keller; J. Polym. Sci. B 34, 797 (1996).

[278] L. Larini, R. Mannella, D. Leporini; J. Chem. Phys. 126, 104101 (2007).

[279] L.R. Dodd,T.D. Boone, D.N. Theodorou, Mol. Phys. 78, 961 (1993).

[280] J.I Siepmann, D. Frenkel, Mol. Phys. 75, 59 (1992).

[281] J.J. de Pablo, M. Laso, U.W. Suter, J. Chem. Phys. 96, 2395 (1992).

[282] A. Uhlherr, Macromolecules 33, 1351 (2000).

[283] P.V.K. Pant, D.N. Theodorou, Macromolecules 28, 7224 (1995).

[284] V.G. Mavrantzas, T.D. Boone, E. Zervopoulou, D.N. Theodorou, Macromolecules 32, 5072 (1999).

[285] V.G. Mavrantzas, D.N. Theodorou, Comput. Theor. Polym. Sci. 10, 1 (2000).

[286] S. Geyler, T. Pakula, J. Reiter, J. Chem. Phys. 92, 2676 (1990).

[287] S. Balijepalli, G.C. Rutledge, J. Chem. Phys. 109, 6523 (1998).

[288] N.C. Karayiannis, V.G. Mavrantzas, D.N. Theodorou, Phys. Rev. Lett. 88, 105503 (2002).

[289] V.A. Harmandaris, V.G. Mavrantzas, D.N. Theodorou, M. Kröger, J. Ramirez, H.C. Öttinger, D. Vlassopoulos, Macromolecules, 36, 1376 (2003).

[290] P. Minary, M.E. Tuckerman, G.J. Martyna, Phys. Rev. Lett. 93, 150201 (2004).

[291] D. Janežič, M. Praprotnik, F. Merzel, J. Chem. Phys. 122, 174101 (2005).

[292] M. Praprotnik, D. Janežič, J. Chem. Phys. 122, 174102 (2005).

[293] M. Praprotnik, D. Janežič, J. Chem. Phys. 122, 174103 (2005).

[294] M. Praprotnik, D. Janežič, J. Mavri, J. Phys. Chem. A 108, 11056 (2004).

[295] H.M. Chun, C.E. Padilla, D.N. Chin et al., J. Comput. Chem. 21, 159 (2000).

[296] A. Malevanets, R. Kapral, J. Chem. Phys. 112, 7260 (2000).

[297] E. Villa, A. Balaeff, K. Schulten, Proc. Natl. Acad. Sci. U.S.A. 102, 6783 (2005).

[298] L. Delle Site, C. F. Abrams, A. Alavi, K. Kremer, Phys. Rev. Lett. 89, 156103 (2002).

[299] M. Praprotnik, L. Delle Site, K. Kremer, J. Chem. Phys. 123, 224106 (2005).

[300] A. Laio, J.V. Vondele, U. Roethlisberger, J. Chem. Phys. 116, 6941 (2002).

[301] G.S. Grest, K. Kremer, Phys. Rev. A 33, 3628 (1986).

[302] K. Kremer, G.S. Grest, J. Chem. Phys. 92, 5057 (1990).

[303] S. Nose, Prog. Theor. Phys. Supp. 103, 1 (1991).

[304] W. Hoover, Phys. Rev. A 31, 1695 (1985).

[305] T. Schneider, E. Stoll, Phys. Rev. B 17, 1302 (1978).

[306] J.N. Bright, D.J. Evans, D. Searles, J. Chem. Phys. 122, 194106 (2005).

[307] H. Mori, Prog. Theor. Phys. 34, 399 (1965).

[308] R. Zwanzig, J. Stat. Phys. 9, 215 (1973).

[309] B. Mishra, T. Schlick, J. Chem. Phys. 105, 299 (1996).

[310] R.I. Cukier, M. Morillo, J. Chem. Phys. 123, 234908 (2005).

[311] R. Mannella, Phys. Rev. E 69, 041107 (2004).

[312] R. Mannella, SIAM J. Scient. Comp. 27, 2121 (2006).

[313] H. Yoshida, Phys. Lett. A 150, 262 (1990).

[314] R.D. Engle, R.D. Skeel, M. Drees, J. Comput. Phys. 206, 432 (2005).

[315] R.D. Skeel, D.J. Hardy; SIAM J. Scient. Comp. 23, 1172 (2001).

[316] R. Mannella, Int J. Mod. Phys. C 13, 1177 (2002).

[317] R.D. Skeel, G. Zhang, T. Schlick; SIAM J. Scient. Comp. 18, 203 (1997).

[318] J.A. Izaguirre, Ph.D. thesis, University of Illinois Urbana-Champaign, 1999. Available on-line via http://www.cs.uiuc.edu/research/tech-reports.html

[319] J. GrotenDorst, D. Marx, A. Maramatsu editors; *Quantum Simulation of Complex Many-Body Systems: From Theory to Algorithms* (NIC series, Jülich, 2002), p. 224.

[320] J. Sanz-Serna, M. Calvo; *Numerical Hamiltonian problems*(Chapman and Hall, London, 1994).

[321] G.N. Milstein, Y.M. Repin, M.V. Tretyakov; SIAM J. Numer. Anal. 40, 1583 (2002).

[322] G.N. Milstein, Y.M. Repin, M.V. Tretyakov; SIAM J. Numer. Anal. 39, 2066 (2002).

[323] S.C. Harvey, R.K.Z. Tan, T.E. Cheatman; J. Comput. Chem. 19, 726 (1998).

[324] E. Hairer; Ann. Numer. Math. 1, 107 (1994).

[325] E. Hairer, C. Lubich; Numer. Math. 76, 441 (1997).

[326] S. Reich; SIAM J. Numer. Anal. 36, 1549 (1999).

[327] R.W. Hamming; *Numerical Methods for Scientist and Engineers* (Mc Graw-

Hill, New York, 1962).

[328] O. Buneman; J. Comput. Phys. 1, 517 (1967).

[329] B. Mehlig, D.W. Heermann, B.M. Forrest; Phys. Rev. B 45, 679 (1992).

[330] E. Forest, R.D. Ruth, Physica D 43, 105 (1990).

[331] H.F. Trotter, Proc. Am. Math. Soc. 10, 545 (1959).

[332] G.Strang; SIAM J. Numer. Anal. 5,506 (1968).

[333] T. Shardlow; SIAM J. Sci. Comput. 24, 1267 (2003).

[334] M. Tuckerman, B.J. Berne, G.J. Martyna, J. Chem. Phys. 97, 1990 (1992).

[335] I.P. Omelyan, I.M. Mryglod, R. Folk, Phys. Rev. E 65, 056706 (2002).

[336] W.C. Swope, C.H. Andersen, P.H. Berens, K.R. Wilson, J. Chem. Phys. 76, 637 (1982).

[337] R.L. Stratonovich; *Topics in the Theory of Random Noise I* (Gordon and Breach, New York, 1963).

[338] H. Haken; Rev. Mod. Phys. 47, 67 (1975).

[339] G.G. Batrouni, G.R. Katz, A.S. Kronfeld, G.P. Lepage, B.Svetitsky, K.G. Wilson; Phys. Rev. D 32, 2736 (1985).

[340] G.N. Milstein, M.V. Tretyakov; IMA J. Numer. Anal. 23, 593 (2003).

[341] D.L. Ermak; Rapport d'activité scientifique du CECAM, pp.66-81 (1976)

[342] D.L. Ermak, H. Buckholtz; J. Comput. Phys. 35, 169 (1980).

[343] W.H. Press, A.S. Teukolsky, W.T. Vetterling, B.P. Flannery, *Numerical Recipes: the Art of Scientific Computing* (Cambridge University Press,Cambridge,2002).

[344] A. Brünger, C.B. Brooks, M. Karplus, Chem. Phys. Lett. 105, 495 (1984).

[345] Z. Ou, M. Muthukumar; J. Chem. Phys. 124, 154902 (2006).

[346] W. Paul, D.Y. Yoon, G.D. Smith, J. Chem. Phys. 103, 1702 (1995).

[347] D.E. Knuth, *The Art of Computer Programming. Vol 2: Seminumerical Algorithms* (Addison Wesley, Reading, 1981).

[348] I.P. Omelyan, I.M. Mryglod, R. Folk, Comput. Phys. Comm. 151, 273 (2003).

[349] M. Sofroniou, W. Oevel, SIAM J. Numer. Anal. 34, 2063 (1997).

[350] P.F. Batcho, T. Schlick, J. Chem. Phys. 115, 4003 (2001).

[351] P.F. Batcho, T. Schlick, J. Chem. Phys. 115, 4019 (2001).

[352] E. Barth, T. Schlick, J. Chem. Phys. 109, 1617 (1998).

[353] E. Barth, T. Schlick, J. Chem. Phys. 109, 1633 (1998).

[354] A. Sandu, T. Schlick, J. Comput. Phys. 151, 74 (1999).

[355] J.A. Izaguirre, D.P. Catarello, J.M. Wozniak, R.D. Skeel, J. Chem. Phys. 114, 2090 (2001).

[356] A. Papoulis, *Probability, Random Variables, and Stochastic Processes* (McGraw-Hill, New Yrok, 1984).

[357] G.P. Johari, D. Pyke; Phys. Chem. Chem. Phys. 2, 5479 (2000).

[358] M. Le Meste, D. Champion, G. Roudaut, G. Blond, D. Simatos; J. Food. Sci. 67, 2444 (2002).

[359] H. Levine Ed.; *Amorphous Food and Pharmaceutical Systems* (Royal Society of Chemistry, London,2002).

[360] S. Kasapis; Drying Technol. 23, 731 (2005).

[361] S. Brawer; *Relaxation in Viscous Liquids and Glasses* (American Ceramic Society, Columbus, OH, 1985).

[362] C.A. Angell;J. Non-Cryst. Solids 131, 13 (1991).

[363] P.G. Debenedetti;*Metastable Liquids: Concepts and Principles* (Princeton University Press, Princeton, NJ,1996).

[364] J.C. Dyre; Rev. Mod. Phys. 78, 953 (2006).

[365] N. Goldenfeld; *Lectures on Phase Transitions and the Renormalization Group* (Addison-Wesley, Reading, MA, 1992).

[366] J.C. Maxwell; Philos. Trans. R. Soc. London 157, 49 (1867).

[367] W. Kauzmann; Chem. Rev. 43, 219 (1948).

[368] J.R. Manning; *Diffusion Kinetics for Atoms in Crystals* (Wiley, New York, 1968).

[369] E.B. Watson, E.F. Baxter;Earth Planet Sci. Lett. 253, 307 (2007).

[370] R.G. Palmer; Adv. Phys. 31, 669 (1982).

[371] H.C. Öttinger; Phys. Rev. E 74, 011113 (2006).

[372] C.A. Angell; Science 267, 1924 (1995).

[373] A. Pimpinelli, J. Villain; *Physics of Crystal Growth* (Cambridge University Press, Cambridge, UK, 1998).

[374] C.A. Angell; J. Phys.: Condens. Matter 12, 6463 (2000).

[375] J. Jäckle; Rep. Prog. Phys. 49, 171 (1986).

[376] C.A. Angell, K.L. Ngai, G.B. McKenna, P.F. McMillan, S.W. Martin; J. Appl. Phys. 88, 3113 (2000).

[377] G.B. McKenna in *Comphensive Polymer Science* edited by C. Booth, C. Price (Pergamon, Oxford, 1989), Vol. 2, p. 311.

[378] C.A. Angell in *Relaxation in Complex Systems* edited by K.L. Ngai, G.B. Wright (U.S. GPO, Washington, D.C., 1985), p. 3.

[379] S.G. Brush; Chem. Rev. 62, 513 (1962).

[380] S. Arrhenius; Z. Phys. Chem. 4, 226 (1889).

[381] A.K. Varshneya; *Fundamentals in Inorganic Glasses* (Academic, New York, 1994).

[382] H. Vogel; Phys. Z. 22, 645 (1921).

[383] G.S. Fulcher; J. Am. Ceram. Soc. 8, 339 (1925).

[384] G. Tamman, W. Hesse; Z. Anorg. Allg. Chem. 156, 245 (1926).

[385] S.F. Edward; Polymer 17, 933 (1976).

[386] F.H. Stillinger; J. Chem. Phys. 88, 7818 (1988).

[387] G.W. Scherer, J. Non-Cryst. Solids 123, 75 (1990).

[388] F. Stickel, E.W. Fischer, R. Richert; J. Chem. Phys. 102, 6251 (1995).

[389] D. Kivelson, G. Tarjus, X. Zhao, S.A. Kivelson; Phys. Rev. E 53, 751 (1996).

[390] C. Walther; Erdoel Teer 7, 382 (1931).

[391] G. Harrison; *The Dynamic Properties of Supercooled Liquids* (Academic, New York, 1976).

[392] H. Bässler; Phys. Rev. Lett. 58, 767 (1987).

[393] I. Avramov; J. Non-Cryst. Solids 351, 3163 (2005).

[394] D.J. Plazek, K.L. Ngai; Macromolecules 24, 1222 (1991).

[395] R. Böhmer, K.L. Ngai, C.A. Angell, D.J. Plazek; J. Chem. Phys. 99, 4201 (1993).

[396] G. Ruocco, F. Sciortino, F. Zamponi, C. De Michele, T. Scopigno; J. Chem. Phys. 120, 10666 (2004).

[397] J.C. Dyre; Phys. Rev. E 59, 2458 (1999).

[398] J.C. Dyre; Phys. Rev. E 72, 011501 (2005).

[399] J.C. Dyre; Phys. Rev. E 74, 021502 (2006).

[400] F.G. Stillinger, T.A. Weber; Phys. Rev. A 28, 2408 (1983).

[401] T.B. Schrøder, S. Sastry, J.C. Dyre, S.C. Glotzer; J. Chem. Phys. 112, 9834 (2000).

[402] J.H. Gibbs, E.A. DiMarzio; J. Chem. Phys. 28, 373 (1958).

[403] G. Adam, J.H. Gibbs; J. Chem. Phys. 43, 139 (1965).

[404] P.A. Rolla, D. Prevosto, M. Lucchesi, S. Capaccioli, L. Larini; Current Trends in Polymer Science 9, 69 (2004).

[405] M.H. Cohen, D. Turnbull; J. Chem. Phys. 31, 1164 (1959).

[406] G.S. Grest, M.H. Cohen in *Advances in Chemical Physics* edited by I. Prigogine, S.A. Rice (Wiley, New York, 1981), Vol. 48, p. 455.

[407] W. Götze, L. Sjögren; Rep. Prog. Phys. 55, 241 (1992).

[408] A.P. Sokolov; Endeavour 21, 109 (1997).

[409] S.P. Das; Rev. Mod. Phys. 76, 785 (2004).

[410] A. Tobolsky, R.E. Powell, H. Eyring in *Frontiers in Chemistry* edited by R.E. Burk, O. Grummit (Interscience, New York, 1943), Vol. 1, p. 125.

[411] H.A. Kramer; Physica 7, 284 (1940).

[412] R.W. Hall, P.G. Wolynes; J. Chem. Phys. 86, 2943 (1987).

[413] U. Buchenau, R. Zorn; Europhys. Lett. 18, 523 (1992).

[414] T. Kanaya, T. Tsukushi, K. Kaji, J. Bartos, J. Kristiak; Phys. Rev. E 60, 1906 (1999).

[415] S. Magazù, G. Maisano, F. Migliardo, C. Mondelli; Biophys. J. 86, 3241 (2004).

[416] E. Cornicchi, G. Onori, A. Paciaroni; Phys. Rev. Lett. 95, 158104 (2005).

[417] A.P. Sokolov, A. Kisliuk, D. Quitmann, A. Kudlik, E. Rössler; J. Non-Cryst. Solids 172, 138 (1994).

[418] V.N. Novikov, E. Rössler, V.K. Malinovsky, N.V. Surovtsev; Europhys. Lett. 35, 289 (1996).

[419] C.M. Roland, K.L. Ngai; J. Chem. Phys. 104, 2967 (1996).

[420] M.M. Teeter, A. Yamano, B. Stec, U. Mohanty; Proc. Natl. Acad. Sci. USA 98, 11242 (2001).

[421] F.W. Starr, S. Sastry, J.F. Douglas, S.C. Glotzer; Phys. Rev. Lett. 89, 125501 (2002).

[422] P. Bordat, F. Affouard, M. Descamp, K.L. Ngai; Phys. Rev. Lett. 93, 105502 (2004).

[423] K.L. Ngai; Philos. Mag. 84, 1341 (2004).

[424] C.P. Flynn; Phys. Rev. 171, 682 (1968).

[425] U. Köhler, C. Herzig; Philos. Mag. A 58, 769 (1988).

[426] S.D. Bond, B.J. Leimkuhler, B.B. Laird; J. Comput. Phys. 151, 114 (1999).

[427] G.J. Martyna, M.E. Tuckerman, D.J. Tobias, M.L. Klein; Mol. Phys. 87, 1117 (1996).

[428] H. C. Andersen; J. Chem. Phys. 72, 2384 (1980).

[429] S. Nosé; J. Chem. Phys. 81, 511(1984).

[430] M. E. Tuckerman, B. J. Berne, G.J. Martyna; J. Chem. Phys. 94, 6811 (1991).

[431] C.A. Angell; J. Am. Chem. Soc. 51, 117 (1968).

[432] S.V. Nemilov; Russ. J. Phys. Chem. 42, 726 (1968).

[433] J.C. Dyre, N.B. Olsen, T. Christensen; Phys. Rev. B 53, 2171 (1996).

[434] J.C. Dyre, N.B. Olsen; Phys. Rev. E 69, 042501 (2004).

[435] L.-M. Martinez, C.A. Angell; Nature 410, 663 (2001).

[436] T. Scopigno, G. Ruocco, F. Sette, G. Monaco; Science, 302, 849 (2003).

[437] V.N. Novikov, A.P. Sokolov; Nature 431, 961 (2004).

[438] A.P. Sokolov, E. Rössler, A. Kisliuk, D. Quitmann, Phys. Rev. Lett. 71, 2062 (1993).

[439] S. Sastry; Nature 409, 164 (2001).

[440] X. Xia, P.G. Wolynes; PNAS 97, 2990 (2000).

[441] S.N. Yannopoulos, G.P. Johari; Nature 442, E7 (2006).

[442] J.D. Ferry, L.D. Jr. Grandine, E.R. Fitzgerald, J. Appl. Phys. 24, 911 (1953).

[443] J.P. Garrahan, D. Chandler; PNAS 100, 9710 (2003).

[444] C. Monthus, J.-P. Bouchaud; J. Phys. A: Math. Gen. 29, 3847 (1996).

[445] J.E. Straub, J.-K. Choi; J. Phys. Chem. 98, 10978 (1994).

[446] C.M. Roland, R. Casalini; J. Chem. Phys. 119, 1838 (2003).

[447] J.H. Bilgram; Phys. Rep. 153, 1 (1987).

[448] H. Löwen; Phys. Rep. 237, 249 (1994).

[449] J.P. Boon, S. Yip; *Molecular Hydrodynamics* (Dover Publications, New York, 1980).

[450] Q. Qin, G.B. McKenna; J. Non-Cryst. Solids 352, 2977 (2006).

[451] K.M. Bernatz, I. Echeverría, S.L. Simon, D.J. Plazek; J. Non-Cryst. Solids 289, 9 (2001).

[452] D. Engberg, A. Wischnewski, U. Buchenau, L. Börjesson, A.J. Dianoux, A.P. Sokolov, L.M. Torell; Phys. Rev. B 58, 9087 (1998).

[453] D. Sidebottom, R. Bergman, L. Börjesson, L.M. Torell; Phys. Rev. Lett. 71, 2260 (1993).

[454] R. Busch, E. Bakke, W.L. Johnson; Acta Mater. 46, 4725 (1998).

[455] A. Meyer, H. Franz, B. Sepiol, J. Wuttke, W. Petry; Europhys. Lett. 36, 379 (1996).

[456] H.Z. Cummins, J. Hernandez, W.M. Du, G. Li; Phys. Rev. Lett. 73, 2935 (1994).

[457] J. Wuttke, W. Petry, G. Coddens, F. Fujara; Phys. Rev. E 52, 4026 (1995).

[458] C.M. Roland, M.J. Schroeder, J.J. Fontanella, K.L. Ngai;Macromolecules 37, 2630 (2004).

[459] B. Frick, L.J. Fetters; Macromolecules 27, 974 (1994).

[460] D.J. Plazek, J.H. Magill; J. Chem. Phys. 49, 3678 (1968).

[461] K.L. Ngai; J. Non-Cryst Solids 275, 7 (2000).

[462] H. Franz, W. Petry, A.Q.R. Baron; Hyperfine Interact. 123/124, 865 (1999).

[463] N. Menon, S.R. Nagel, D.C. Venerus; Phys. Rev. Lett. 73, 963 (1994).

[464] A. Tölle; Rep. Prog. Phys. 64, 1473 (2001).

[465] R. Zorn; J. Phys.: Condens. Matter 15, R1025 (2003).

[466] B. Frick, D. Richter; Science 267, 1939 (1995).

[467] B. Frick, D. Richter, W. Petry, U. Buchenau; Z. Phys. B 70, 73 (1988).

[468] C.M. Roland, K.L. Ngai, P.G. Santangelo, X.H. Qiu, M.D. Ediger, D.J. Plazek; Macromolecules 34, 6159 (2001).

[469] T. Kanaya, K. Kaji, J. Bartos, M. Klimova; Macromolecules 30, 1107 (1997).

[470] R.H. Colby; Phys. Rev. E 61, 1783 (2000).

[471] C.L. Soles, J.F. Douglas, W.-I. Wu, R.M. Dimeo; Macromolecules 36, 373 (2003).

[472] N.G. McCrum, B.E. Read, G. Williams; *Anelastic and Dielectric Effects in Polymeric Solids*(Dover Publications, New York, 1991).

[473] G. Smith, D. Bedrov; J. Polym. Sci. B 45, 627 (2007).

[474] J. Dudowicz, K.F. Freed, J.F. Douglas; J. Phys. Chem. B 109, 21285 (2005).

[475] J. Dudowicz, K.F. Freed, J.F. Douglas; Adv. Chem. Phys., in press